INVESTIGATION OF RAIN EROSION ON GERMANIUM BY USING FINITE ELEMENT METHOD

A THESIS SUBMITTED TO
THE GRADUATE SCHOOL OF NATURAL AND APPLIED SCIENCES
OF
MIDDLE EAST TECHNICAL UNIVERSITY

BY

HÜSEYİN ANIL SALMAN

IN PARTIAL FULFILLMENT OF THE REQUIREMENTS
FOR
THE DEGREE OF MASTER OF SCIENCE
IN
MECHANICAL ENGINEERING

AUGUST 2011

Approval of the thesis:

INVESTIGATION OF RAIN EROSION ON GERMANIUM BY USING FINITE ELEMENT METHOD

submitted by **HÜSEYİN ANIL SALMAN** in partial fulfilment of the requirements for the degree of **Master of Science in Mechanical Engineering Department, Middle East Technical University** by,

Prof. Dr. Canan Özgen _____
Dean, Graduate School of **Natural and Applied Sciences**

Prof. Dr. Süha Oral _____
Head of Department, **Mechanical Engineering**

Prof. Dr. R. Orhan Yıldırım _____
Supervisor, **Mechanical Engineering Dept., METU**

Examining Committee Members:

Prof. Dr. Metin Akkök _____
Mechanical Engineering Dept., METU

Prof. Dr. R. Orhan Yıldırım _____
Mechanical Engineering Dept., METU

Prof. Dr. Can Çoğun _____
Mechanical Engineering Dept., METU

Asst. Prof. Dr. Yiğit Yazıcıoğlu _____
Mechanical Engineering Dept., METU

Dr. Rıdvan Toroslu _____
Lead Design Engineer, ASELSAN INC.

Date: 24.08.2011

I hereby declare that all information in this document has been obtained and presented in accordance with academic rules and ethical conduct. I also declare that, as required by these rules and conduct, I have fully cited and referenced all material and results that are not original to this work.

Name, Last Name : H. ANIL SALMAN

Signature :

ABSTRACT

INVESTIGATION OF RAIN EROSION ON GERMANIUM BY USING FINITE ELEMENT METHOD

Salman, Hüseyin Anıl
M.Sc., Department of Mechanical Engineering
Supervisor: Prof. Dr. R. Orhan Yıldırım

August 2011, 107 pages

Impact of rain drops at relatively high velocities, which is known as rain erosion, causes severe damages on various materials. Every material can withstand the rain erosion up to a specific impact velocity. However, this damage is critical for optical windows which are very important components for Electro-Optical (EO) systems such as thermal camera. Even a small scratch may affect the transmission capability of the optical window adversely and leads to some functional problems in the device due to insufficient transmitted data. Since it has a vital effect on the EO systems, the rain erosion is needed to be investigated on the special optical windows, particularly for determining the velocity that a damage initiates.

In this study, the rain erosion is investigated on germanium which is a kind of optical window, by means of numerical simulations in LS-DYNA. Damage Threshold Velocity (DTV) is examined for two different water shapes (which are spherical water drop and water jet) within a velocity range between 100 and 250 m/s. Both single and multiple impact cases are considered for both water shapes up to ten consecutive collisions. By using the results, the "DTV versus number of impact curves" are obtained in order to understand the amount of damage with respect to both single and multiple impacts. Results are compared with both literature and the experimental data within the scope of DTV and shape of the damage.

In the numerical simulations, ALE (Arbitrary Lagrangian Eulerian) method is used for modelling water. “JOHNSON-HOLMQUIST-CERAMICS (JH-2)” which is recommended for both ceramics and glass applications is used as the material model for Germanium. JH-2 is a complete material model which contains damage effects, failure criteria, and Equation of State (EOS) all together. Among the material models available in the library of LS-DYNA, “MAT-NULL + EOS-GRUNEISEN” is used for water.

Keywords: ALE; Brittle materials; Germanium; Johnson Holmquist; Rain erosion.

ÖZ

GERMANYUM ÜZERİNDEKİ YAĞMUR EROZYONUNUN SONLU ELEMANLAR YÖNTEMİ KULLANILARAK İNCELENMESİ

Salman, Hüseyin Anıl
Yüksek Lisans, Makina Mühendisliği Bölümü
Tez Yöneticisi: Prof. Dr. R. Orhan Yıldırım

Ağustos 2011, 107 sayfa

Yağmur erozyonu olarak bilinen yağmur damlacıklarının göreceli yüksek hızlarda çarpması çeşitli malzemelerde hasara yol açar. Bütün malzemeler yağmur erozyonuna belirli bir çarpışma hızına kadar dayanabilir. Ancak, bu hasar termal kamera gibi Elektro Optik (EO) sistemlerin çok önemli bir parçası olan optik camlarda kritiktir. Optik cam üzerinde oluşan küçük bir çizik bile geçirgenliği kötü yönde etkileyibilir ve sonuç olarak yetersiz bilgi aktarımından kaynaklı cihazda bazı fonksiyonel problemlere neden olur. Yağmur erozyonunun EO sistemler üzerinde hayati etkisi olduğu için, optik camlarda, özellikle hasarın başladığı bu hızın belirlenmesi açısından incelenmesine ihtiyacı vardır.

Bu çalışmada, bir çeşit optik bir cam olan germanyum'un yağmur erozyonuna karşı dayanımı sayısal benzetim ile LS-DYNA'da incelenmiştir. Hasar Eşik Hızı (HEH) iki farklı su şekli için (küresel su damlacığı ve su jeti) 100 ve 250 m/s hız aralığında incelenmiştir. Tek ve çoklu çarpışma durumları on ardışık çarpmaya kadar iki su şekli için de incelenmiştir. Hasarın boyutlarının tek ve çoklu çarpışma durumlarına göre incelenebilmesi için HEH'nin çarpışma sayısına göre eğrileri çizdirilmiştir. Sonuçlar hem literatür ile hem de deneysel çalışma ile HEH ve deformasyon şekli kapsamında karşılaştırılmıştır.

Sayısal benzetimlerde, suyu modellemek için ALE (Arbitrary Lagrangian Eulerian) tekniği kullanılmıştır. Germanyum için seramik ve cam uygulamalarında önerilen "JOHNSON-HOLMQUIST-CERAMICS (JH-2)" malzeme modeli kullanılmıştır. JH-2 malzeme modeli içersinde hasar etkisi, kopma kriteri ve durum denklemini barındıran bir malzeme modeli bütünüdür. LS-DYNA kütüphanesinde bulunan malzeme modelleri arasından su için "MAT-NULL + EOS-GRUNEISEN" kombinasyonu kullanılmıştır.

Anahtar Kelimeler: ALE; Kırılgan malzeme; Germanyum; Johnson Holmquist; Yağmur Erozyonu.

To My Family

ACKNOWLEDGMENTS

I would like to express my sincere gratitude to Prof. Dr. R. Orhan YILDIRIM for his endless support, supervision, encouragement and patience during the all research activities.

The current work is a part of a research and development project which has been conducted in ASELSAN Inc. I would like to thank to my company ASELSAN Inc., my manager Mr. İhsan ÖZSOY and my project manager Mr. Alp Eren Sinan ÖZHAN for providing me all the opportunities to take the advantage of computational capabilities of the company, educational attainments (for the use of LS-DYNA) and experimental activities.

I would like to thank to Dr. Ali M. ÇOLAKOĞLU for his encouragement, advice, support and guidance in all steps of the study.

I would like to express my appreciation to my colleague A. Levent AVŞAR for his valuable support and understanding.

Lastly, I would like to express my endless gratitude to my family for their love, support and faith in me.

TABLE OF CONTENTS

LIST OF TABLES

TABLES

LIST OF FIGURES

FIGURES

LIST OF SYMBOLS

P	Pressure
ρ	Density
C	Shock velocity
C_0	Acoustic velocity
k	Constant for shock velocity correction
C_L	Longitudinal wave velocity
C_T	Transverse wave velocity
v	Velocity
k	A constant in the first order shock correction
d	Diameter
r	Radius of the curvature
τ	Time for the high pressures start slowing down
τ'	Time for the complete release of the high pressure stage
$v_{treshold}$	DTV of a specific infrared material
K_{Ic}	Fracture toughness
C_R	Rayleigh wave speed
ν	Poisson's ratio
ρ_w	Density of water
d_w	Diameter of the rain drop
ρ_0	Initial Density
E	Young's modulus
S_1	Material constant for EOS-GRUNEISEN
S_2	Material constant for EOS-GRUNEISEN
S_3	Material constant for EOS-GRUNEISEN
γ_0	Material constant for EOS-GRUNEISEN
a	Material constant for EOS-GRUNEISEN
E_i	Initial internal energy for EOS-GRUNEISEN
V_i	Initial relative volume for EOS-GRUNEISEN

σ^*	Normalized strength of the material
σ_i^*	Normalized intact equivalent stress
σ_f^*	Normalized fracture stress
D	Damage
σ	Actual equivalent stress
σ_{HEL}	Equivalent stress at the Hugoniot elastic limit (HEL)
σ_x	Normal stress at x direction
σ_y	Normal stress at y direction
σ_z	Normal stress at z direction
τ_{xy}	Shear stress at x-y direction
τ_{xz}	Shear stress at x-z direction
τ_{yz}	Shear stress at y-z direction
A	Material constant for JOHNSON-HOLMQUIST Material Model
B	Material constant for JOHNSON-HOLMQUIST Material Model
C	Material constant for JOHNSON-HOLMQUIST Material Model
M	Material constant for JOHNSON-HOLMQUIST Material Model
N	Material constant for JOHNSON-HOLMQUIST Material Model
σ_{fmax}^*	Material constant for JOHNSON-HOLMQUIST Material Model
T	Maximum tensile hydrostatic pressure the material can withstand
T^*	Normalized maximum tensile hydrostatic pressure
P_{HEL}	Pressure at the Hugoniot elastic limit (HEL)
P^*	Normalized pressure
$\dot{\varepsilon}$	Actual equivalent strain rate
$\dot{\varepsilon}^*$	Dimensionless strain rate
$\dot{\varepsilon}_0$	Reference strain rate
$\Delta\varepsilon_p$	Equivalent plastic strain
ε_p^f	Plastic strain to fracture under a constant pressure
K_1	Pressure constant for JOHNSON-HOLMQUIST Material Model
K_2	Pressure constant for JOHNSON-HOLMQUIST Material Model
K_3	Pressure constant for JOHNSON-HOLMQUIST Material Model

j	Rain fall rate
V	Velocity
A	Cross sectional area
v_t	Terminal velocity
t	Duration

ABBREVIATIONS

ADTV	: Absolute Damage Threshold Velocity
ALE	: Arbitrary Lagrangian Eulerian
DTV	: Damage Threshold Velocity
DTV	: Damage Threshold Velocity
EO	: Electro Optical
EOS	: Equation of State
FEM	: Finite Element Method
FSI	: Fluid Solid Interaction
GE	: Germanium
HEH	: Hasar Eşik Hızı
HEL	: Hugoniot Elastic Limit
JH	: Johnson-Holmquist
LLNL	: Lawrance Livermore National Laboratories
LSTC	: Livermore Software Technology Corporation
MIJA	: Multi Impact Jet Apparatus
PMMA	: Polymethylmethacrylate
SEM	: Scanning electron microscopy
SIJA	: Single Impact Jet Apparatus
SST	: Single Shot Threshold

CHAPTER 1

INTRODUCTION

This chapter covers the important aspects of rain erosion on optical materials. How the rain erosion mechanism works and which materials are susceptible for this kind of damage are presented with the help of illustrative figures. Scope of the thesis is also introduced.

1.1 Motivation to Rain Erosion Problem

The rain erosion is a kind of damage which occurs when the rain droplets strikes to a target at relatively high velocities as the name implies. However, why this deformation is important and needed to be investigated is explained below.

1.1.1 Electro Optical Systems

Electro-Optical (EO) devices, such as thermal cameras basically use infrared lights to carry out their missions. These lights which cannot be sensed by normal eye are emitted from outer environment and converted to visible range of colors by these systems. Even though these technologies are used in defense systems mostly, they also serve for civil applications.

In order to work properly, EO devices should receive high amount of infrared lights which are reflected from the objects. These lights are taken into EO device by the help of optical windows. So, optical windows or lenses (as it can be seen in Figure

1.1) are critical components of the EO devices. Materials of these windows are commonly germanium (Ge), sapphire, and silicon for different optical operation ranges. These materials have high infrared transmission capability and by this way, they provide the sufficient amount of light taken into the EO system.

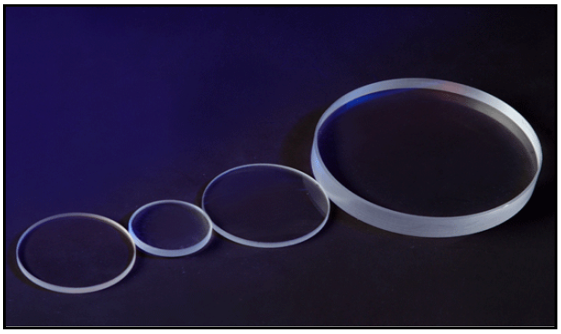

Figure 1.1 Optical windows.

Since the optical windows have a vital role on EO systems, they shouldn't be deformed in any shape or form in order not to affect the device negatively. However, the only interface component between the sensors and outer environment is just these optical components as it can be seen Figure 1.2. So, these special windows are exposed to all the external threats during the harsh operating/working conditions.

Figure 1.2 Electro Optical device.

1.1.2 Rain Erosion on Infrared Windows

Using EO systems on aircrafts which travels at supersonic speeds means that infrared window moves at the same speed also. Collision of raindrops, bugs or any other small particles impacting at relative high velocities can cause damage on the optical windows and reduce transmission capability accordingly. As a result, EO devices cannot keep its intended functions with a damaged window, lens or dome due to the insufficient amount of infrared lights.

Nora Osborne and George Graves [1] made a study with LANTIRN (low-altitude navigation and targeting infrared night pod system) and FLIR (forward-looking infrared) windows to investigate the damage on the optical window. LANTIRN and FLIR systems are EO devices mounted on supersonic aircrafts in order to provide vision at night and bad air conditions. According to the study, 68 damaged windows were analyzed and characterized by bug strike, rain erosion, sand erosion, surface atmospheric etching etc. The investigation methodology includes visual and low-magnification examinations, profilometry and scanning electron microscopy (SEM). Among the 68 condemned windows, 35% of them were characterized by rain erosion damage. Figure 1.3 shows the sub-critical bug strike damage and Figure 1.4 shows rain erosion damage [1].

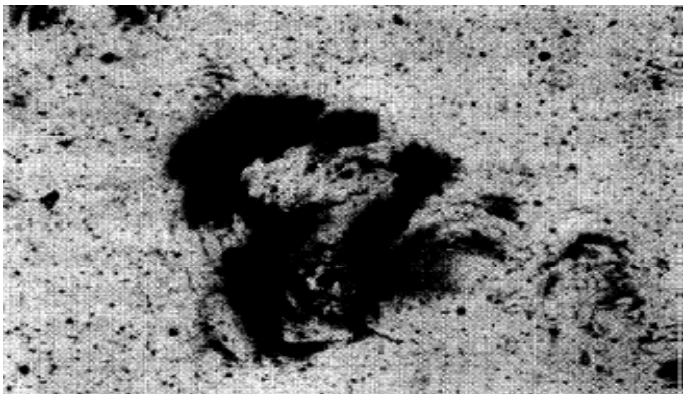

Figure 1.3 Bug strike damage.

Figure 1.4 Rain erosion damage.

There are several threats on the optical windows during the high speed flights. In this study, the rain erosion is investigated among the factors that lead to deformation or failure on the optical components. In a Defense Standard about the natural environment [2] the rain erosion is defined as damage caused to solid surfaces by the impact of raindrops and the liquid impact is described in a paragraph like that:

> *The behavior of a raindrop on impact depends largely on the velocity of impact. Based on laboratory observations, it is considered that with impact velocities up to approximately 300 m/s a waterdrop behaves like a hard projectile on impact but retains its liquid property of flow. At greater velocities the drop behaves progressively like a hard projectile which does not flow as a result of the collision. Tests have shown that a drop colliding with 3 mm thick 1100-H14 aluminum sheet at 600 m/s makes an impression similar to that made on the same material by the impact of a 5.5 mm diameter steel sphere at the relatively slow impingement velocity of 70 m/s* [2].

1.2 Scope of Thesis

It is clear that the optical windows can be damaged as a result of high velocity liquid

impact during the working conditions of the EO device. In order to avoid such a situation, having knowledge about the rain erosion resistance of the interested optical material is very important. If the velocity, under which there is no damage is occurred, is known for a specific optical window, the usage area of that material can be determined according to this information. For example, if this velocity is about 130 m/s, the EO device cannot be used in the applications that comprise higher speeds than 130 m/s such as supersonic aircrafts.

In order to understand the resistance of a specific optical material against rain erosion, generally experimental studies are conducted. It is understood from these studies that, the amount of damage is increased by each collision of the water drop/jet. The rain erosion is dependent not only the impact velocity, but also the number of successive impacts. There is numerical simulation studies regarding the liquid impact in the literature as well as the experimental studies, but the most of these studies are related with the single impact condition of the liquid.

In this study, it is aimed to find out the Damage Threshold Velocity (DTV) (under which there is no serious damage occurred) for the specific lens material germanium by the use of finite element method. The durability of germanium against rain erosion is investigated according to both single and multiple impact (up to 10 successive impacts) conditions.

CHAPTER 2

LITERATURE SURVEY ON RAIN EROSION

In this chapter, the general concepts found in the literature about the rain erosion are discussed. In the first section, a brief description of the liquid impact, water hammer pressure and mechanism of the out jetting of the water drop after the impact are mentioned. Then the numerical studies regarding the liquid impact are presented. These studies generally cover the single liquid impact onto a specified target. After that, a term DTV (Damage Threshold Velocity) which is frequently used in the rain erosion literature and the current work is explained in detail. To find the DTV of an optical window, an analytical approach with respect to the physical properties of the lens material is also described in the same section. The following section covers the most common test techniques used to simulate the rain erosion. Lastly, experimental studies found in the literature regarding the rain erosion are discussed.

2.1 Brief Theory of Liquid Impact

At high velocities, impact of a liquid mass to a solid surface can generate high transient pressures and may cause critical damage on the target. This type of damage may be unimportant for the materials used in the applications where optical transmission is not required. However, if the target is an optical component of an EO device, this damage may lead both transmission and strength losses during the high speed flights. Because of that the understanding the severity of the liquid impact is important.

Liquid impact can be divided into two phases which are compressible and incompressible [3]. In the early stage of the impact (compressible phase) the liquid becomes compressible due to the high transient pressures generated by the collision. Most of the damages occur during this phase. After the release of the high pressure period, liquid becomes incompressible and spreading or out jetting of the liquid starts. Both phases of the impact are briefly described below.

2.1.1 Compressible Phase: Water Hammer Pressure

If a column of water at a finite velocity is stopped by a stationary target, most of the velocity (kinetic) energy of the liquid is converted to the potential energy during the impact and high transient pressure occurs. This pressure causes a slight degree of compressibility in both solid and fluid.

Initial stage of the collision between a spherically shaped water drop and a solid target is shown in Figure 2.1 [2]. The liquid behind the shock envelope which consist of many wavelets is compressed due to the momentum of the fluid.

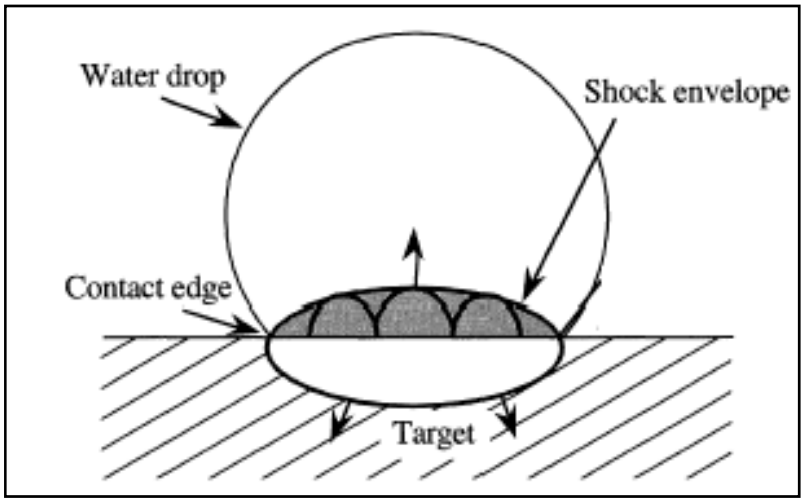

Figure 2.1 Initial stage of the water drop impact.

Cook [4] was the first to remark that high pressures can be generated in water drop

impact as a result of the so-called 'water hammer' effect. So, in the compressible phase of the impact, the occurred high pressures can be estimated by the water hammer pressure. Water hammer pressure, by definition, is the pressure as a result of impact of a liquid mass to a rigid target. This pressure is also mentioned in other studies [5-8] and it is given as;

$$P = \rho C v \qquad \text{or} \qquad P = \rho C_0 v[1 + k(V/C_0] \qquad (1.1)$$

where ρ is the density of the liquid, C is the shock velocity of the liquid and v is the impact speed. Shock velocity C is found from the first order shock correction $C = C_0 + kv$, where C_0 is the acoustic velocity and it is about 1500 m/s for water and k is a constant which is nearly 2 for water within the velocity range up to 1.2 Mach [5].

An interesting point should be underlined that the value of the water-hammer pressure is not dependent to the length of the liquid column and this can be seen in Equation 1.1. The length the liquid column can only change the duration of the total impact.

The high pressures start slowing down after a time of [6]:

$$\tau = rv/2C^2 \qquad (1.2)$$

The complete release of the high pressure stage and the end of the compressible phase could be defined as [6];

$$\tau' = 3rv/2C^2 \qquad (1.3)$$

where, r is the radius of curvature of the water drop (liquid mass).

2.1.2 Incompressible Phase: Out jetting of Liquid

Heymann [8], investigated that one of the occurred wavelets at the beginning of the impact attaches to the spreading edge contact point “e” in Figure 2.2, during the information of the collision is transferred to unaffected portion of the drop. It is well known from the impact mechanics that the information of the collision carried by the shock waves. The speed of the shock wave is about 1500 m/s for water. This shock velocity is considerably higher than the impact speed which is maximum 300-400 m/s under the normal conditions. It is observed that contact edge “e” (Figure 2.2) has a velocity nearly ten times faster than the normal impact speed [9]. Therefore, it can be interpreted that the contact edge moves faster even than the compression wave, if the impact speeds are higher than 150 m/s approximately.

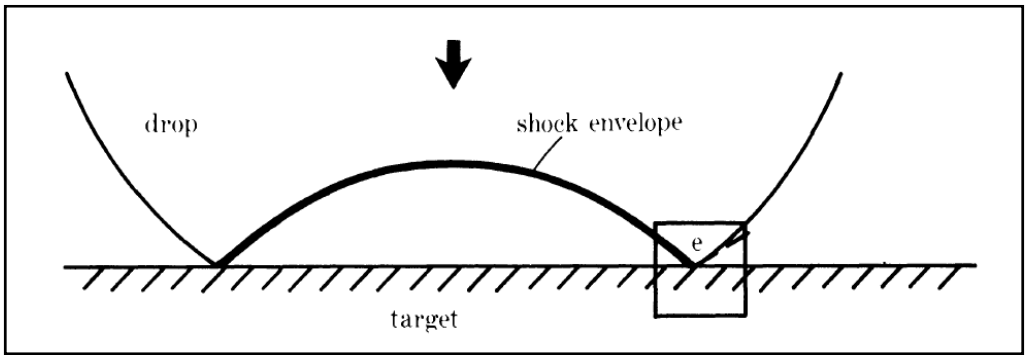

Figure 2.2 Contact edge of the impacted liquid [9].

Field and Lesser [9] make an explanation regarding the out jetting mechanism of the spherically shaped drop. As it has been mentioned above, according to the Heyman’s principle, the shock envelope must attach to the edge contact point. At the early stages of the impact, the contact boundary expands over the solid surface with a speed of exceeding the shock speed in the liquid. However, the speed of the contact edge is obstructed as a result of the convex surface of the spherical drop. This process will continue until the speed of the contact edge falls below the speed of the compression wave. When this occurs, the contact signal moves up the free drop

surface as it can be seen in Figure 2.3. As soon as the liquid meets the ambient conditions, compressed liquid undergoes an expansion. Finally, water spreads out from the compressed edge region.

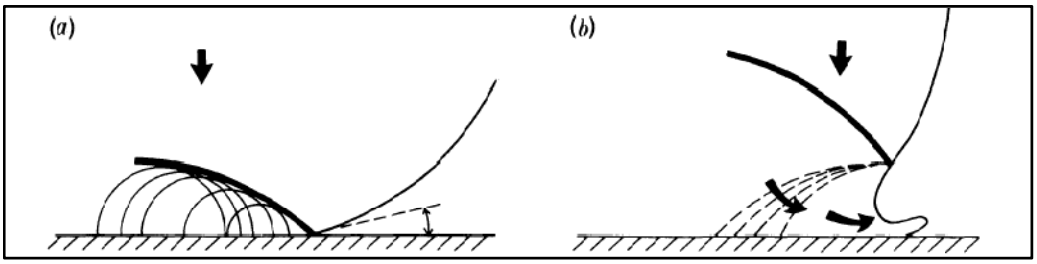

Figure 2.3 Spreading of the drop (out jetting) [9].

2.2 Numerical Simulation Studies Regarding Liquid Impact

An important issue should be mentioned before presenting the numerical simulation studies found in the literature regarding the liquid impact. The main aim of the current thesis is estimating the DTV of the target material (germanium) against the rain erosion by means of numerical simulation. The DTV, in a few words, is the maximum velocity of the impacted liquid (water) without causing any damage on the target. In the rain erosion literature, the DTV is also described by the multiple impacts of rain droplets. In other words, in working conditions of an optical system there are more than one rain drop may hit to the same place on the window and the damage may be formed after several impacts although there is no damage observed for the first impact. So, multiple impact condition is important and should also be considered as well as the single impact in the rain erosion studies. However, it cannot be found any numerical study that investigates the DTV of a specified target material (optical window) by considering the multiple impact condition. Most of the numerical studies in the literature focused on the single impact condition. Generally, the theoretical aspects of the liquid impact such as occurrence of the water hammer pressure, lateral jetting of the fluid and stress wave propagation was studied in detail. Actually, multiple impact condition is generally subjected to the experimental

studies. If it is looked at this point of view, the present thesis is said to be one of the first studies that investigates the DTV by employing the multiple impact of the liquid as well as the single impact in a commercial finite element software (LS-DYNA). For this reason, some previously made numerical simulation studies (in which only single impact condition is considered) regarding the liquid impact are presented here.

The fluid dynamics of the liquid impact onto a rigid surface was investigated in a computational study by Haller [10] at relatively high velocities (500 m/s) of the very small sized water drop (0.2 mm in diameter) by using the eulerian technique. The classical Heyman principle regarding the outjetting mechanism in the liquid impact was proved by this work. It was shown in the simulations that, a shock wave is attached to the contact edge of the droplet. As soon as this wave is generated, the liquid zone under the shock envelope is highly compressed and separated from the unaffected portion of the droplet. The radial velocity of the contact edge (which moves with a higher velocity than the shock wave) decreases below the shock velocity. After the shock wave moves up and releases from the contact edge, the pressure difference across the free surface triggers the discharge/outjetting of the fluid.

In a study which consists of two parts by Li N and co-workers [11], liquid impact is investigated in turbine blades by means of both numerical simulation and analytic (wave equations) approaches. The first part establishes one-dimensional nonlinear wave model. One of the important result according to the study is that, for 1-D liquid – solid impact condition, the peak pressure occurred at the initial stage of the impact is nearly 10% higher than the classic water hammer pressure.

The following publication [12] which is the second of the previous study, liquid impact is investigated again on the turbine blades in three dimensions. It is highlighted that the radial shock waves (out jetting direction) is faster than that is formed in the axial ones (impact direction) in the water drop. It is also mentioned that the stress wave at the front is almost in spherical shape. There are two regions specified as the high transient stress zones. One of them is near the axis and the other

near the contact edge.

William F. Adler and Dennis J Mihora [13] have built a three dimensional finite element model to simulate the waterdrop impact on a structured target. The basic model consists of four different materials which are waterdrop, infrared window (ZnSe Substrate), coating layer in a protective manner and a bond layer as it can be seen Figure 2.4. The bond layer is placed between the coating and the substrate material in order to provide adhesion. DYNA2D and DYNA3D finite element codes which are the basis of LS-DYNA were used as a solver. In the study, critical stress states were identified however, the description of the failure modes within the target has been left as a future work. The available strength data of the target material were compared with the computational results. According to the study, the protective layer over the substrate has been of vital importance. The stresses in the substrate were significantly reduced by using protective layer.

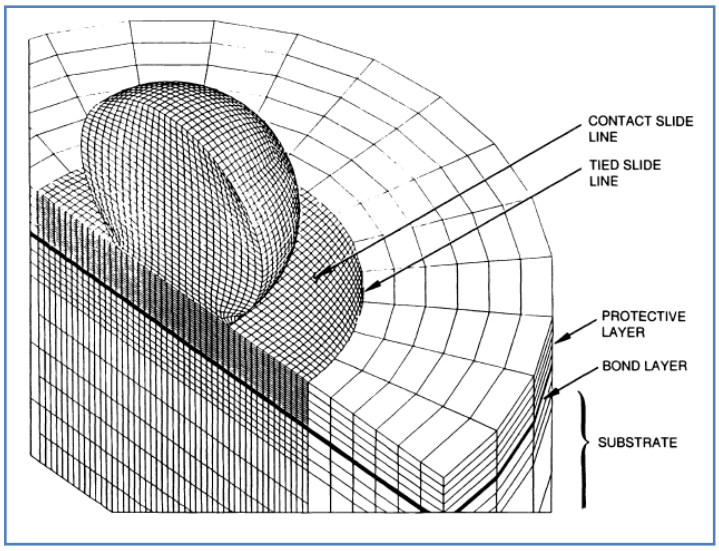

Figure 2.4 General finite element model of water drop impact [13].

Yale Chang [14] has shortly mentioned to rain erosion of missile radomes in a study which includes numerical simulation of the liquid impact but the main aim of the study is not the liquid impact. Rain drop was modelled by using SPH technique and

the target is selected as glass as it is seen in Figure 2.5. The modelled water is spherical in shape. Although there is no specific impact velocity is indicated at this reference, it is seen that the glass plate is perforated as result of the collision of the water drop. There is no information about the diameter of the spherically shaped water drop either but, it is seen that the thickness of the glass plate nearly the half of the diameter of the water drop. At this ratio between the diameter of water drop and the plate thickness, it is normal to expect perforation on the target if the impact velocity is relatively high.

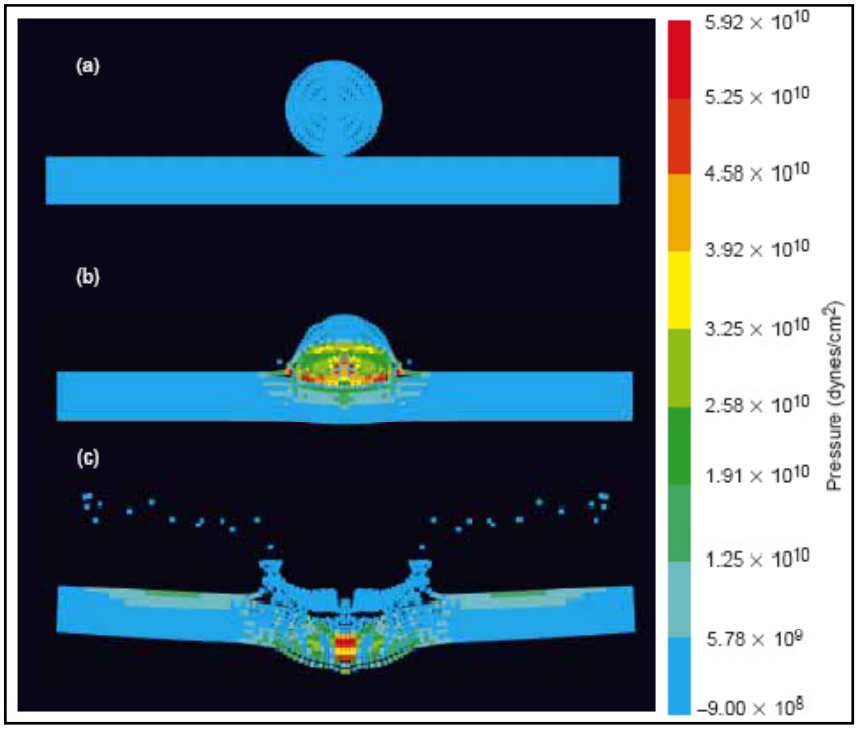

Figure 2.5 Impact of spherical rain drop to a glass plate at (a) 0 µs, (b) 2 µs and (c) 20 µs [14].

Benjamin A. Tutt and Anthony P. Taylor [15] investigate the water landing characteristics of space vehicles by using ALE technique in LS-DYNA. The general view of the finite element model is shown Figure 2.6. The model represents the drop of Apollo Capsule which is a kind of earth landing system onto the water. Occurred acceleration values in three dimensions as a result of the impact are compared with

the test data from NASA (National Aeronautics and Space Administration) and high level of consistency is acquired from the finite element simulation. Although there is no water drop or water jet impact subjected into this study, the current work can be readily regarded as the liquid impact problem since there is a fluid-solid interaction as it has been in the other studies.

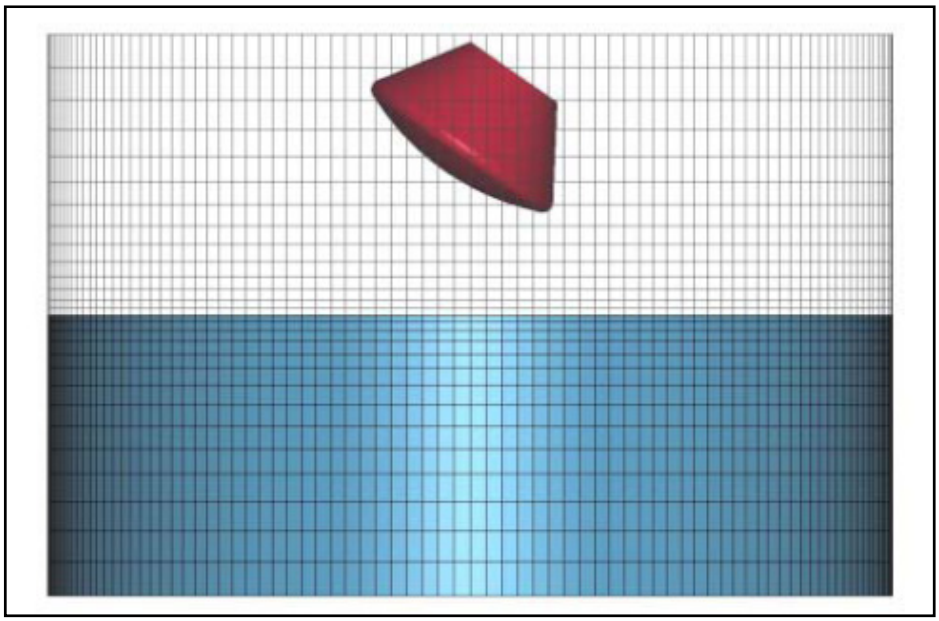

Figure 2.6 The general view of the finite element model for Apollo 17 capsule.

2.3 DTV and an Analytical Approach to DTV

DTV (Damage Threshold Velocity) is a commonly used term regarding the rain erosion. DTV can be defined easily that; the velocity under which there is no serious damage on the target material. However, DTV is a general term and there are some add-ons are used with this term in the literature in order to specify the meaning. This is because the damage caused by a single impact and several impact can be different on the target material. The initiation of the failure of the target caused by a single drop is specified as “Single Shot Threshold (SST)” or “DTV (single impact)”. The initiation of the failure of the target caused by multiple impacts is specified as “DTV

(Number of the impact)" for example, DTV (5 impacts). The highest velocity that doesn't cause any damage on the target and if the damage is independent from the number of impacts, this condition is defined as: Absolute Damage Threshold Velocity (ADTV). Actually, if there is only the rain erosion of a specific lens material is interested in, the most appropriate threshold value is the ADTV. The single impact or several impact results cannot provide the rain erosion resistance of the target material absolutely.

The threshold velocity values with respect to single impact, DTV (single impact), for several lens materials are listed in Table 2.1 by Harris [7]. It is seen that the most durable optic material against the single impact is sapphire which can withstand nearly 1.5 mach impact velocity of the water drop. However, the least durable optic material against the single impact is ZnSe. It is also remarkable that the different atomic structure of the same materials causes different responses against the liquid impact.

Table 2.1 DTV (single impact) or SST values of some infrared lens materials for 2 mm diameter water drop.

Material	Threshold (m/s)	Material	Threshold (m/s)
ZnS	<175	MgF2 (hot pressed)	340-381
ZnSe	137-152	MgF2 (single crystal)	274-320
Si(single crystal)	<274	Spinel (single crystal)	<395
Sapphire	457-533	Spinel (fusion cast)	<457

ADTV of a specific infrared material can be estimated by the following mathematical expression [7]:

$$v_{treshold} \approx 1.41 \left(K_{Ic}^2 \, C_R \Big/ \rho_w^2 \, C_0^2 \, d_w \right)^{1/3} \qquad (2.1)$$

where, K_{Ic} is the fracture toughness of the infrared material, some of which are listed in Table 2.2 [7], C_R is the Rayleigh wave speed of the infrared material, ρ_w is the density of the water, C_0 is the compression wave speed (acoustic speed) in water (~1500 m/s) and d_w is the diameter of the raindrop.

Table 2.2 Fracture toughness values of some important lens materials.

Material	Fracture toughness (MPa$\sqrt{m}$)	Material	Fracture toughness (MPa$\sqrt{m}$)
ZnSe	0.5	MgAl2O4(spinel)	1.9
ZnS(standard	1.0	ALON	1.4
GaAs[(100 face)]	0.4	Y2O3(doped/undoped)	0.7
GaP(single crystal)	0.8	Al2O3(sapphire)	2.0
Ge(single crystal)	0.7	Si3N4(silicon nitride)	4.0
Si	0.9	SiC(silicon carbide)	4.0
Fused SiO2	0.8	Diamond	7.0

Rayleigh wave speed on an elastic solid can be calculated as [7]:

$$C_R = \left(0.862 + 1.14 \, \nu / 1 + \nu \right) \sqrt{E / 2(1 + \nu)\rho} \qquad (2.2)$$

Where, ν is the Poisson's ratio, E is young's modulus and ρ is the density of the window material.

Physical properties of some infrared windows including the germanium are listed in

Table 2.3 by Kiocek [16].

Table 2.3 Physical Properties of IR Window and Dome Materials.

	ZnS-s/ ZnS-m	GaP	GaAs	Si	Ge	Diamond	ZnSe	Al_2O_3	Y_2O_3	ALON	$MgAl_2O_4$	MgF_2
M.P. (K)	2130	1740	1511	1693	1210	3770	1790	2300	2723	2425	2400	1528
σ (MPa)	96	100	89	127	93	1000	68	400	125	300	190	52
α (10^{-6}/K)	6.8	5.3	5.7	2.3	6.0	1.0	7.0	5.3	7.1	7.8	8.0	8.5-13.7
v (Poisson's ratio)	0.29/0.32	0.31	0.31	0.28	0.278	0.16	0.28	0.27	0.29	0.24	0.26	0.27
k (W/mK)	17	97	53	140	60	2000	19	34	14	11	15	0.25
ϱ (g/cc)	4.08	4.13	5.317	2.33	5.323	3.51	5.42	3.98	5.03	3.69	3.57	3.176
E (GPa)	74.5/87.6	102.6	85.5	130	103	1050	70.9	380	164	317	193	139
G (GPa)	60	90	79	98.5	77	514.7	40	249.6	130.2	203.2	134	55
Bandgap (eV)	3.58	2.24	1.43	1.12	0.67	5.40	2.7	9.9	5.6	—	—	—
Hardness (kg/mm^2)	230/160	845	700	1150	850	9000	137	1800	650	1970	1645	415
Structure	Cubic	Cubic	Cubic	Cubic	Cubic	Cubic	Cubic	Hexa-gonal	Cubic	Cubic	Cubic	Tetra-gonal
K_{IC} ($MPam^{1/2}$)	1.0	0.8	0.43	0.95	0.66	7.0	0.75	3.3	1.1	2.0	1.6	—
n (refractive index)	2.2	2.9	3.3	3.4	4.0	2.4	2.4	1.7	1.9	1.6	1.7	1.3
dn/dT (10^{-6})	45	100	150	160	400	10	75	13	32	≈13	≈13	—

2.4 Test Techniques on Rain Erosion

A variety of test techniques was used over the years in order to simulate the rain erosion or water drop impact over the infrared materials experimentally. The aim of the experimental studies is to determine/evaluate the DTV of the infrared materials within the scope of the liquid impact.

Among the various test techniques available in the literature and published by Seward and co-authors [17], only the most common three methods are explained in this section. The first one is the whirling arm test technique, the second is the single impact jet apparatus (SIJA) and the last is multi impact jet apparatus (MIJA).

2.4.1 Whirling Arm

Benjamin Robins (1745) was the first who used whirling arm rigs so as to establish

foundations of the aerodynamic drags. Although the test setup was mostly replaced by the wind tunnels in 1900 in order to serve aerodynamics, whirling arm rigs continued to its job with the purpose of simulation of the rain erosion by Robertson (1946) at the Radiation Laboratory of the Massachusetts Institute of Technology [17].

The schematic of a typical whirling arm is shown in Figure 2.7. As it has been understood from the sketch below, when the whirling arm rotates in the chamber at a certain speed, the specimen mounted on the end of the arm strikes to the water drops released from the rain nozzles above. In this way multiple drop impact results can be obtained. Multiple impact experiment in the rain erosion can be made in several minutes (such as 5 minutes) by this technique. However, the exact number of the drops that impacted to the specimen cannot be measured by this way.

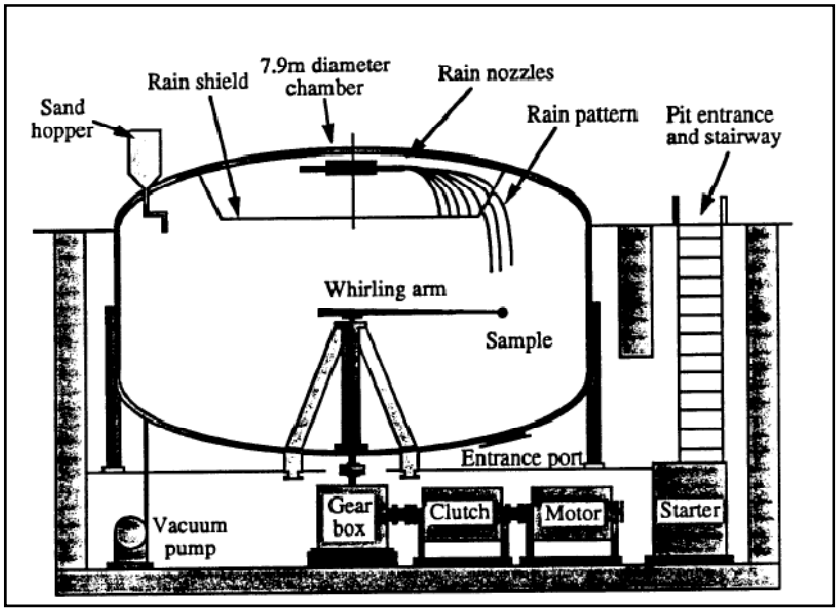

Figure 2.7 Bell Aerospace Company whirling arm ring [17].

Several whirling arm test facilities are listed in Table 2.4. As can be seen that the maximum arm radius belongs to the SAAB-SCANIA among the listed test facilities.

On the other hand, maxiumum velocity (3.0 mach) and rainfall rate (320 mm/h) can be reached in Dornier.

Table 2.4 Whirling arm test facilities.

Facility*	Maximum Mach number	Arm radius (m)	Nominal drop size (mm)	Rainfall rate (mm/h)
UDRI	0.8	1.22	2	25.4
NAWC	0.65	1.22	2	12.2
Bell Helicopter	0.75	1.22	Natural rain	76.2
RAE	0.7	1.45	2	25.4
SAAB-SCANIA	1.0	2.19	1.2-2	1.4-25
Dornier	3.0	1.2	0.5-1.7	1.8-320

*UDRI:University of Dayton Research ınstitute.Wright-Patterson Air Force Base,Dayton,Ohio,NAWC:Naval Air Warfare Center (formerly Naval Air Development Center),Warminster,Pennsylvania.Bell Helicopter:Fort Worth, Texas,RAE:Royal Aircraft Establishment,Farnborough,Great Britain. SAAB-SCANIA:Linköping,Sweden,Domier,Friedrichshafen,Germany.

2.4.2 Single Impact Jet Apparatus (SIJA)

The least expensive way to simulate the water drop impact is shown in Figure 2.8 which is developed by the Bowden and Brunton [18]. The nozzle is initially filled with water or any other liquid which will be fired to the target. A neoprene diaphragm disk holds the liquid in the nozzle and has a slight curvature to the outwards in the direction of the air gun. While the air gun fires a bullet towards the neoprene diaphragm disk liquid inside the nozzle is extruded and strikes to the target. Velocity of the water jet can reach up to 1000 m/s. By using this method DTV of a single rain drop can be determined for a specific lens material. All the necessary velocity measurements of the jet and its motion during impact are recorded by high speed photographic methods [18].

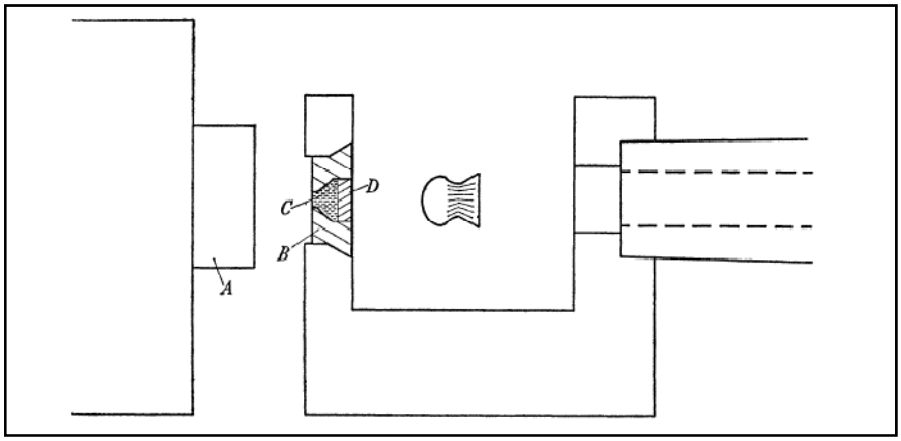

Figure 2.8 Single Impact Jet Apparatus (SIJA); A, target; B, chamber; C, liquid; D, neoprene disk.

2.4.3 Multi Impact Jet Apparatus (MIJA)

Multiple Impact Jet Apparatus (MIJA) is an improved version of SIJA described in previous section. The main difference between two systems, as the name implies, is that the MIJA can simulate the multiple impact conditions faster than the SIJA.

The general view of the test setup is seen in Figure 2.9 [17]. The apparatus basically comprises a horizontal pressure vessel on which pressure sensors and solenoids are connected. Solenoids control the hydraulic fluid flow and open or close the valve according to the amount of pressure. When the required pressure is obtained on the pressure vessel, the solenoid let the compressed air pass down through the vertical cylinder of the apparatus. Inside this cylinder, there is a piston that can move up and down within its stroke. The piston stays at the top of the main body initially and is pushed down as result of the pressurized air released from the pressure vessel. At the end of the travel through the cylinder, the piston hits to a nozzle which is filled full of water. The specimen that is required to be investigated against the rain erosion is placed on the X-Y stage, just below the nozzle. The velocity of the water jet is measured by ultrafast electronics through the distance between nozzle and the

specimen. This operation is repeated for each individual impact after cleaning the residual water over the specimen and returning the piston its initial position.

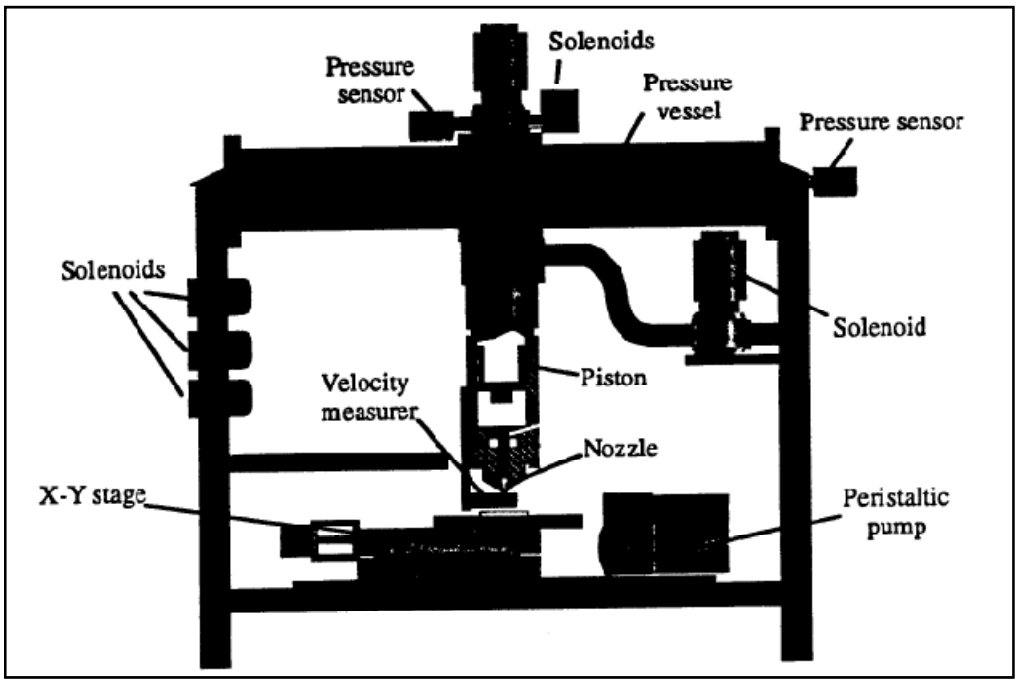

Figure 2.9 Multiple Impact Jet Apparatus.

It has been noted both for SIJA and MIJA experiments that the water is pushed from a nozzle at high velocities in order to realize the impact. However, the shape of the water does not remain like spherically shaped water. The shape of the water resembles to a water jet as it can be seen in Figure 2.10 [6] which shows high speed photographs taken from the MIJA experiment. Moreover, it is interesting that the diameters of the water jet are not the same as the nozzle diameters. For example, the water pushed from a 0.8 mm diameter nozzle becomes nearly 2 mm in diameter at a distance of 20 mm below the nozzle moving at a velocity nearly 120 m/s. The diameter of the water jet gets larger during its travel from nozzle to the target. Apart from this issue, one more thing should also be mentioned in Figure 2.10 that the roundness of the water jet increases as the diameter of the nozzle increases.

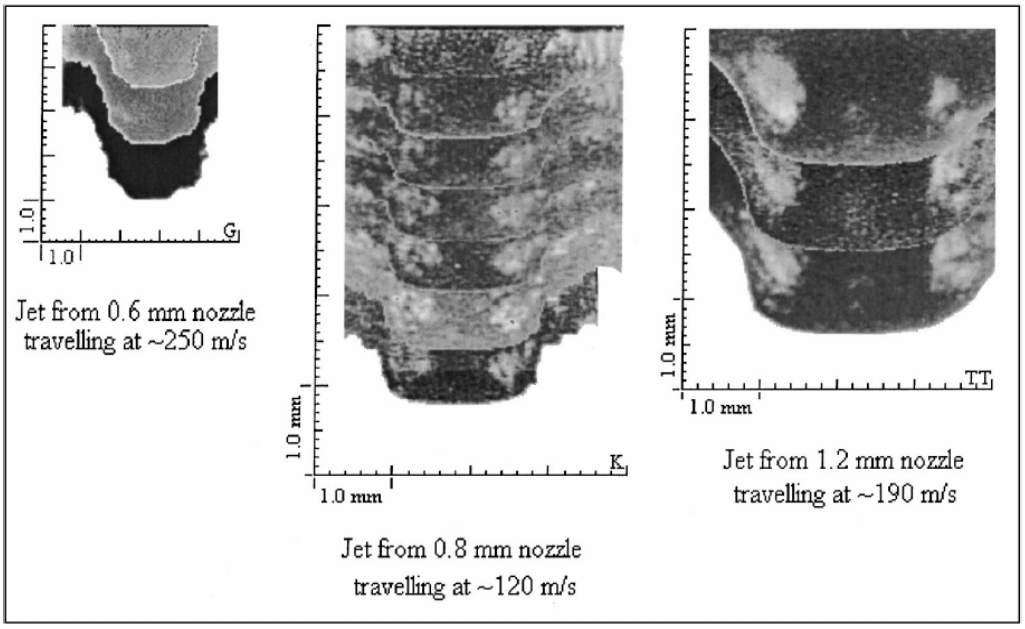

Figure 2.10 Shape of the water jet 20mm below the nozzle.

2.5 Experimental Studies on Rain Erosion

Every infrared material can be damaged if the specific DTV value of the material is exceeded in the rain erosion simulations or any other damage mechanisms such as particle impact occurs in the harsh working conditions. Since EO devices cannot carry out its basic missions with a damaged window, lens or dome as it has been mentioned previously, the information about the velocity that the material can withstand should be known primarily.

This section covers mostly the experimental works on germanium and other materials briefly.

2.5.1 Experimental Studies on Germanium

Zwaag and Field [19] carried out an experimental study regarding the liquid impact

on germanium which is the one of the most important lens material for optical systems in 8-12, 3-5 and 5-12 μm spectral transmission. Impact damage caused from rain erosion was examined on both carbon coated and uncoated germanium substrates at relatively high velocities (>100 m/s). Furthermore, durability of anti-reflection, hard carbon coatings was studied separately by means of ball indentations. At two different thicknesses of carbon coatings (1μm and 3μm) over germanium samples (2mm as thickness and 25mm as diameter) were examined by using tungsten carbide balls (0.4 and 1.0 mm as the diameters) and hardened steel balls (2.0 and 4.0 mm as the diameters) as indenters. According to the results, as the increase of coating thickness and ball radius, the load that cause fracture also increases as it can be seen in Figure 2.11 [19]. However, it is also mentioned that, although 3μm coating provide more protection to the substrate (germanium), risk of the debonding of the coating increases due to the lateral outflow of the liquid on the surface at high impact velocities. 1μm thickness coating served better performance at lower impact velocities, because thin films are less susceptible to debonding and provide sufficient protection to the optical lens.

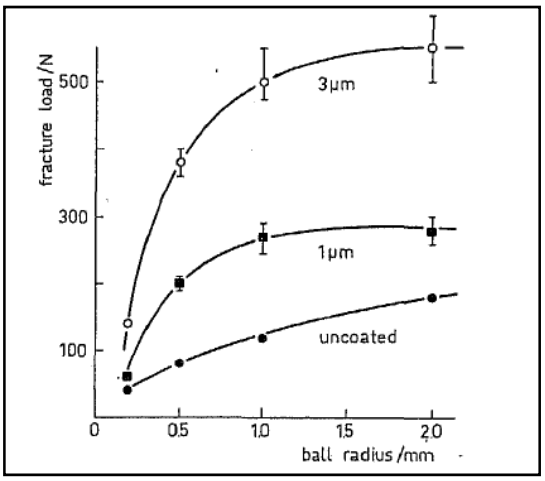

Figure 2.11 Ball indentation test results on both carbon coated and uncoated germanium samples.

Damage patterns caused from the impact of water jet pushed from 0.8 mm diameter

nozzle is shown in Figure 2.12 [19] for both uncoated (left) and carbon coated (right) samples. Successive three impacts at 260 m/s caused considerable damages on uncoated germanium, even at first impact. On 3μm carbon coated samples, debonding of the coating was experienced. Light areas in Figure 2.12 (right side) are the regions that bonding of the coating fails. This is because of the outflow of the water which causes shear stresses on the surface.

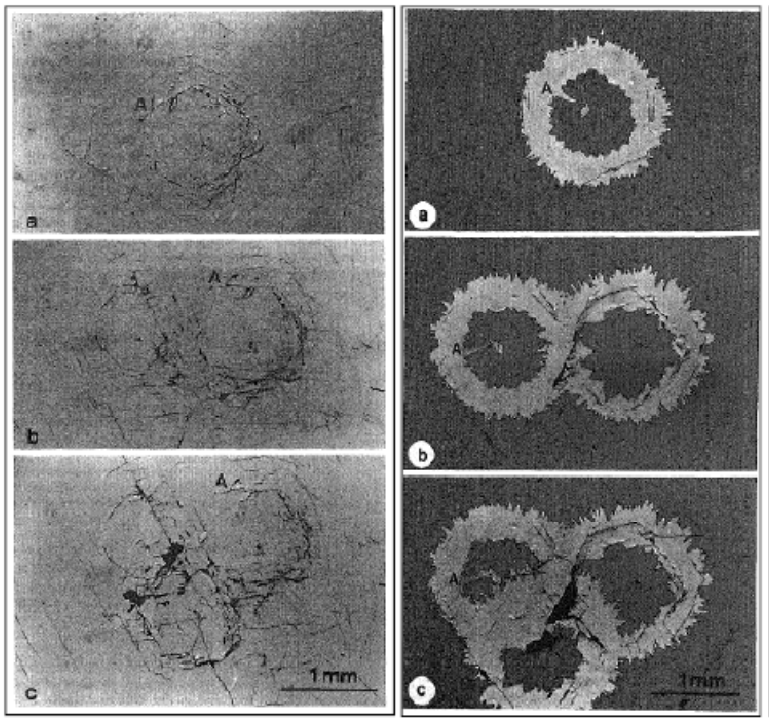

Figure 2.12 Damage patterns after impact of water-jet pushed from 0.8mm diameter nozzle at 260 m/s for uncoated (left) and 3 μm carbon coated (right) germanium samples. Lowercase characters at every picture indicate (a) first impact, (b) second impact and (c) third impact. Uppercase character "A" at every picture is a common feature to compare size of the crack.

Impact velocity was reduced to 220 m/s in Figure 2.13 [19] and damage patterns can be seen for both uncoated and 3 μm carbon coated Germanium samples. Uncoated samples were damaged completely at each impact. However, 3 μm carbon coated samples were protected except only a few isolated cracks on the coating.

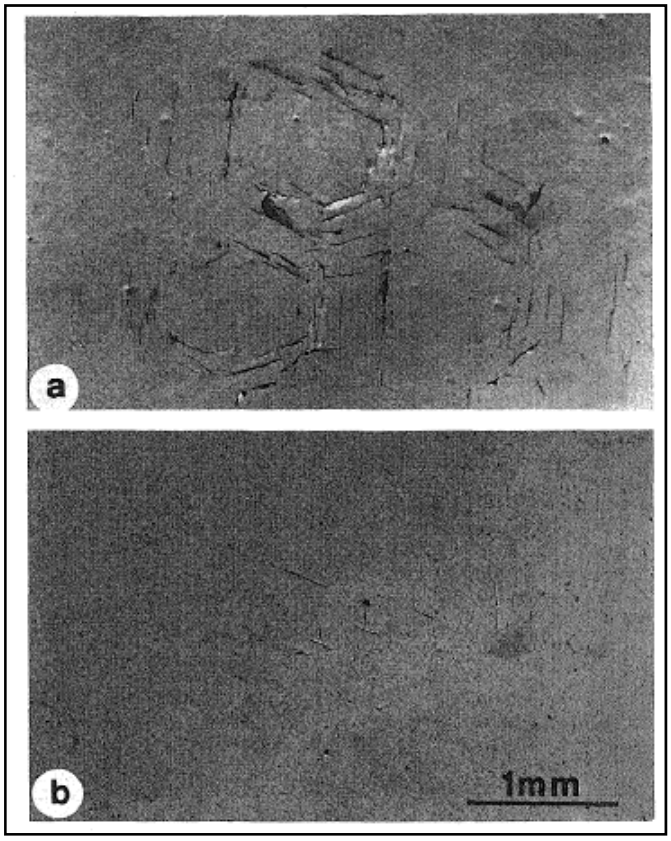

Figure 2.13 Damage patterns after three successive water-jet impacts (0.8 mm diameter) at 220 m/s on (a) uncoated and (b) 3 μm carbon coated Germanium samples.

Coatings with 1 μm thickness were tested also for 220 and 260 m/s impact velocities under the same conditions. Although these results are mentioned in the text, pictures of these cases are not provided in the reference. At 220 m/s impact velocity, no significant differences were reported about the 1 and 3 μm carbon coated samples. At 260 m/s impact velocity, 1 μm coating provides less protection to the germanium lens but debonding does not occur. As a result, it was mentioned that thin film coatings (1 μm) showed better performance at lower impact velocities. At higher velocities, the 3 μm carbon coated samples were also damaged by debonding of the coating.

For the uncoated germanium, Zwaag and Field [19] claim that the ADTV of

germanium window is 150 m/s according to the impact of water jet pushed from 0.8 mm diameter nozzle.

In a report regarding the rain erosion by Seward and co-authors [17], experimental studies of uncoated germanium is presented. All the results are given according to the impact of water jet released from the 0.8 mm diameter nozzle. Two different methods are used in order to plot the threshold curves for uncoated germanium. The first the threshold curve (Figure 2.14) is obtained with a nozzle that is not producing round damage marks on polymethylmethacrylate (PMMA), while the second threshold curve (Figure 2.15) was obtained after the nozzle had been polished so the damage produced was round. After 300 impacts of water pushed from 0.8 mm diameter nozzle, measured ADTV is 155 m/s for the former (Figure 2.14) and 122 m/s for the latter (Figure 2.15).

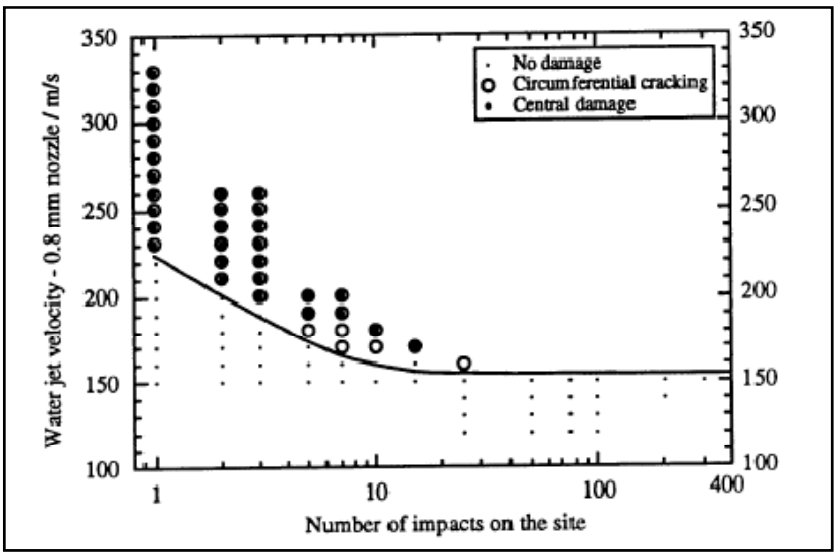

Figure 2.14 Threshold curve for germanium with the nozzle producing non-round damage [17].

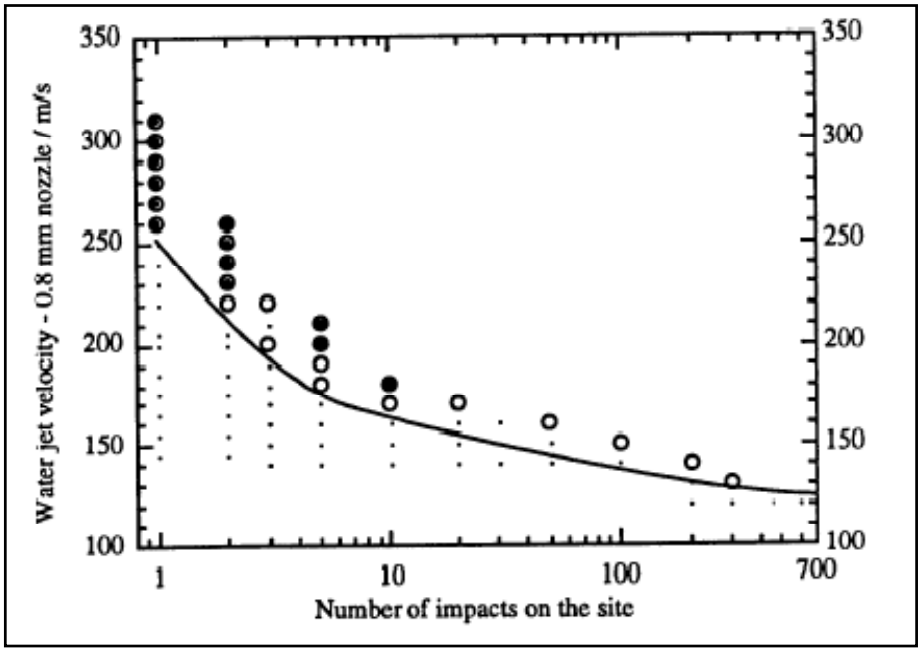

Figure 2.15 Threshold curve for germanium with the nozzle polished producing round damage [17].

2.5.2 DTV of Other Optical Materials

A very comprehensive work has been done by Seward, Coad, Pickles and Field [20] on various optical materials including germanium also. The DTV evaluations of all materials were presented according to water jet pushed from 0.8 mm nozzle. The all results were summarized in a single graph in Figure 2.16.

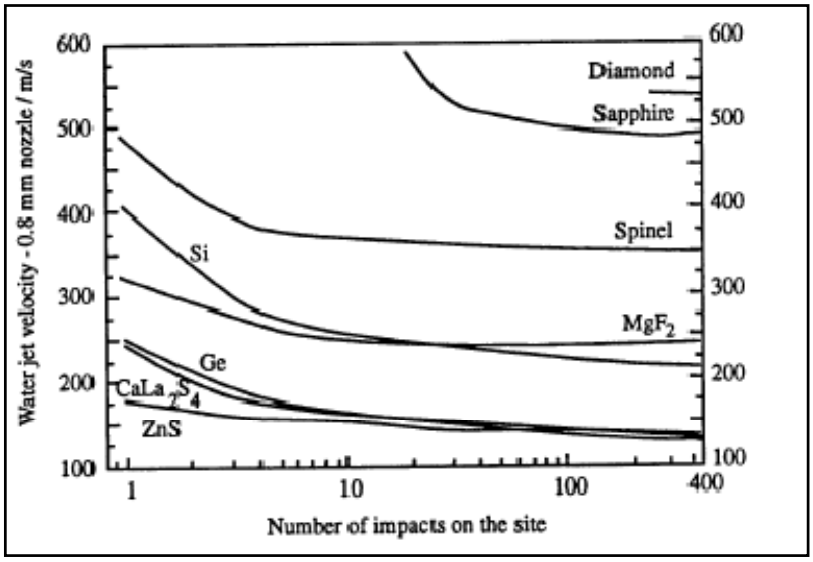

Figure 2.16 A summary of the threshold curves for various optical materials [20].

Among the materials which were used in the scope of the study, it is seen that diamond is the most durable material to rain erosion. However, the least durable material is ZnS among tested materials.

CHAPTER 3

NUMERICAL SIMULATION OF LIQUID IMPACT IN LS DYNA

This chapter covers the topics regarding the numerical simulation of the rain erosion. First of all, a brief introduction is made about the LS-DYNA which is nonlinear, explicit finite element. Afterwards, some of the available solution techniques are mentioned in LS-DYNA and Arbitrary Lagrangian Eulerian (ALE) technique which is an appropriate finite element method for modeling the fluid flow and/or liquid impact problems is described in detail. Since the ALE technique requires a special mesh algorithm in order to provide the fluid flow, the configuration of the nodes and elements for water and void are described with illustrative figures within the same section. The next section covers the coupling algorithm occurred between the water and the germanium during the collision of these two parts. The material models for all parts used in the numerical simulation are described in the following section. And lastly, mesh sensitivity analyses are mentioned.

3.1 Brief Description of LS-DYNA

LS-DYNA is developed by LSTC (Livermore Software Technology Corporation) and its roots go to DYNA3D/2D from LLNL (Lawrance Livermore National Laboratories). Both have been developed by Dr. John Hallquist [21].

LS-DYNA is a pure solver, therefore needs an input file in a specific format and produces results in the form of binary and ASCII data. Input file is generated by

using a pre-processor such as LS-Prepost (LSTC), ANSA (Beta CEA Systems), ANSYS/LS-DYNA, HyperMesh (ALTAIR), Primer (OASYS) and Patran (MSC Software). All the pre-processors have in common that they produce a specific text file as an input (keyword file) for LS-DYNA. By using the results data in binary and ASCII format, post-processing can be performed in LS-Prepost as well as, ANSA, HyperMesh, ANSYS/LS-DYNA, Oasys D3PLOT [21].

Within the scope of the this study, as a solver ANSYS/LS-DYNA is used. LS-DYNA solver module is embedded to ANSYS software and this solver can be directly utilized by using the ANSYS interface. LS-Prepost is used for both pre and post processing operations.

3.2 Solution Techniques in LS-DYNA

Solution of a scientific or an engineering problem via Finite Element Method (FEM) requires an appropriate solution technique and suitable mesh configuration according to the problem while developing the model. Three methods are argued in the current discussion within the scope of the mesh configurations for different FEM applications. These are Lagrangian, Eulerian and ALE techniques. In each technique, there are some common points. Among these techniques ALE is an appropriate one for modeling the fluid impact problem and it will be discussed in detail below.

3.2.1 Common Definitions and Concepts

The main difference between the three techniques is the mesh structure. In each method, the behavior of the mesh is different. There are generally two main issues regarding the mesh configuration. These are material coordinates and spatial coordinates. The former, material coordinates are the imaginary points or nodes which are on the geometry. The latter, spatial coordinates are the points or nodes at the space.

3.2.2 Lagrangian Method (Lagrangian Meshes)

In Lagrangian technique, the spatial coordinates are coincident with material points throughout the simulation with respect to deformation of the body. Since the mesh points (spatial coordinates) follow the body coordinates (material coordinates), the shapes of the elements change with the material. As shown in Figure 3.1, elements move with the body which is exposed to shearing deformation in Lagrangian Method.

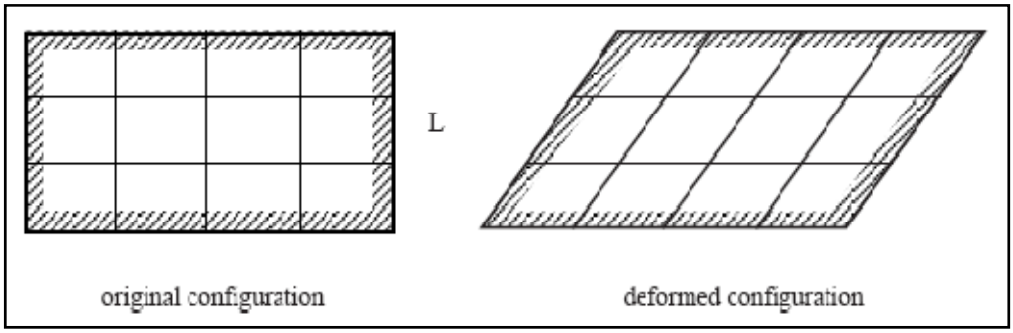

Figure 3.1 Shearing of a two dimensional block in Lagrangian technique [22].

At the end of the simulation, each Lagrangian element (mesh) attached to the material deforms as much as the material. However, the elements should deform up to some extent. If the deformation limit of a specific element is exceeded, the simulation may have errors or leads to wrong results. Therefore, Lagrangian technique becomes insufficient for simulating large deformations such as fluid flows. However, Lagrangian technique has more straight-forward equations and less costly relative to Eulerian and ALE technique.

Solution process in Lagrangian technique is simple and shown in Figure 3.2 below. At t=0, the central node on which the loading is presumed to be applied is at the initial position. At $t=\Delta t$, central node moves on the direction of the force and if the loading continues in the same way, the central node proceed to its new position at $t=2\Delta t$. The spatial coordinates follow the material points as mentioned previously.

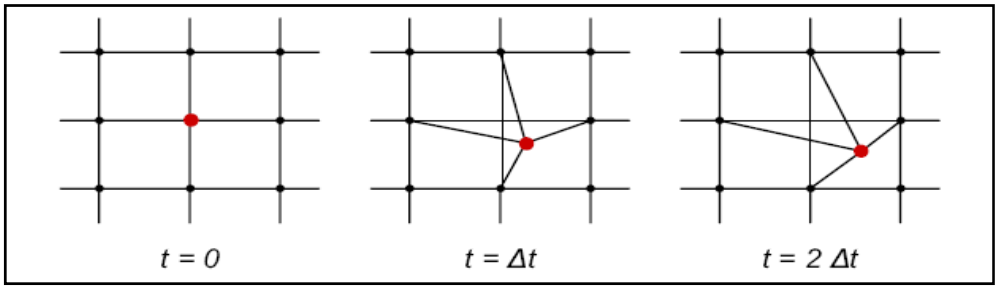

Figure 3.2 Movement of the spatial coordinates in Lagrange Technique [23].

One thing is not to be distinguished in Figure 3.2 that the sliding node represents the spatial coordinates that is attached on the material coordinates. The cells on the background stand for just visualization.

3.2.3 Eulerian Method (Eulerian Meshes)

In Eulerian technique, the spatial coordinates do not remain coincident with material coordinates. The spatial coordinates are fixed in the space and coincident with material coordinates only at t=0. As it is shown at bottom of the Figure 3.3, one time step later from the beginning, the material starts to flow through the fixed Eulerian meshes in the direction of the loading. However, Lagrangian elements follow the material by deforming with respect to direction of the motion (at top of the Figure 3.3). So that, Eulerian elements are never deformed with the material throughout the simulation.

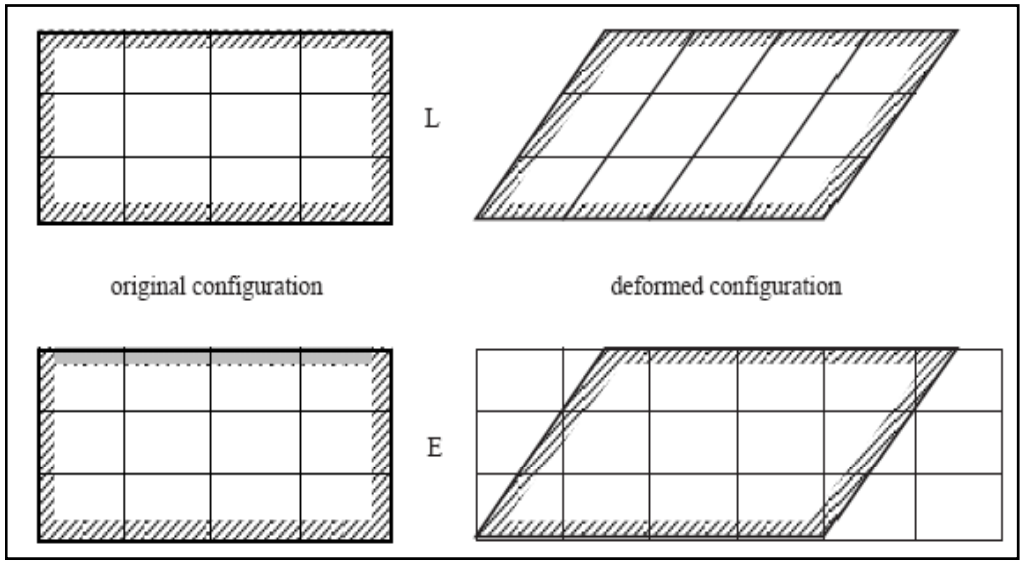

Figure 3.3 Shearing of a two dimensional block in Lagrangian (at top, indicated by L) and Eulerian (at bottom, indicated by E) Techniques [22].

Since the background mesh (spatial coordinates) is not deformed throughout the simulation, elements are not exposed to any shape changes. Because of that, high deformations (observed generally in fluid problems) can be simulated in Eulerian technique.

Solution procedure in Eulerian technique is a little bit different than Lagrangian technique and shown in Figure 3.4. Due to the loading, central node transforms to its new position in the half of the one computational time step as it has been in the Lagrangian mesh. Spatial coordinates are also being deformed initially in the same time step. However, before the time step has completely finished the following operations are performed as mentioned by Vesenjak and co-authors [22]:

- **Mesh smoothing** : deformed nodes in Eulerian mesh due to the loading move back to their original position.

- **Advection** : the element state variables such as stresses, velocity fields, flow fields for all nodes which are calculated at the current time step

are recomputed (interpolated) so that they have the same spatial distribution as before the mesh smoothing. Therefore, the mesh smoothing does not affect the element state variables.

These processes are repeated for all time steps throughout the simulation and it is provided that there is always non-deformed mesh provided for the deformation of the material.

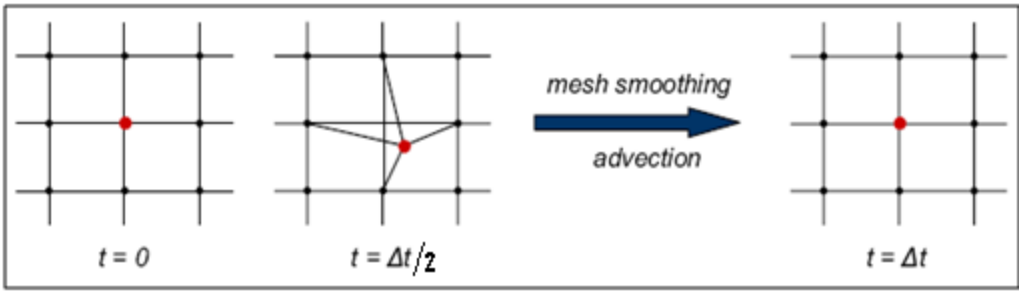

Figure 3.4 Movement of the spatial coordinates in Eulerian technique [23].

3.2.4 ALE Method

ALE method takes the advantages of both Eulerian and Lagrangian techniques as the name suggests. The background mesh (which is fixed in Eulerian technique) can move in the ALE technique with respect to the spread of the material. The spatial coordinates are not attached to the material in a similar way but, not fixed in the space like it has been in the Eulerian technique. The ALE mesh can move arbitrarily in the space and shape of the elements can also change according to the way of simulation. The movement of the ALE mesh is usually in the spread direction of the fluid.

Solution procedure of ALE technique basically resembles to Eulerian techniuqe except the amount of mesh smoothing. In the Eulerian technique, the spatial

coordinates moved back to their initial positions exactly. Because of that the background mesh is always fixed in the space. However, although the mesh smoothing operation is also applied to the ALE elements, deformed nodes do not return to their exact original positions as shown in Figure 3.5. Therefore, ALE mesh is distorted a little bit as the material nodes flow through the spatial coordinates. Because of that ALE mesh can move in the space.

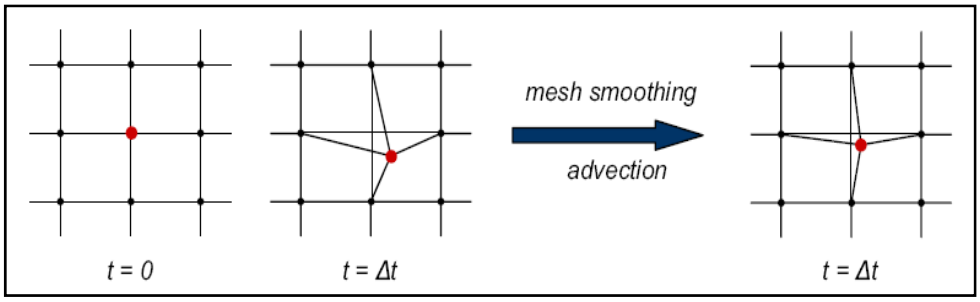

Figure 3.5 Movement of spatial coordinates in ALE technique [23].

Jim Day [24] made study in order to compare all of the mentioned three methods (Lagrangian, Eulerian and ALE) in LS-DYNA. As it is seen in Figure 3.6, the fluid is impacted to a rigid surface simulated by means of all three methods. In the Lagrangian technique (at the top row), the spatial coordinates and the material coordinates are coincident throughout the simulation. Because of that, there is no mesh structure such as void or background mesh can be seen in this kind of simulations. Since the spatial coordinates follows the material deformation in Lagrange technique, elements are highly deformed across the contact region at the end of the simulation. In the second technique (Eulerian method – the middle row), there is a background mesh which is fixed in the space throughout the simulation. This mesh is the so-called spatial coordinates and bigger than the fluid. It is seen that, the fixed background mesh is not deformed throughout the simulation and the fluid freely flows inside undeformed mesh. Lastly, the ALE (the bottom row) was used for the third technique. In this method, there is again a background mesh. However, this background mesh of ALE technique can move and expand with respect to motion of

the fluid. The fluid again flows inside the background mesh as it has been in the Eulerian technique. Since the background mesh for ALE can move in the space, there is no needed a big volume to be filled with the spatial coordinates as it has been in the Eulerian technique. This is the advantage of the ALE technique with respect to Eulerian.

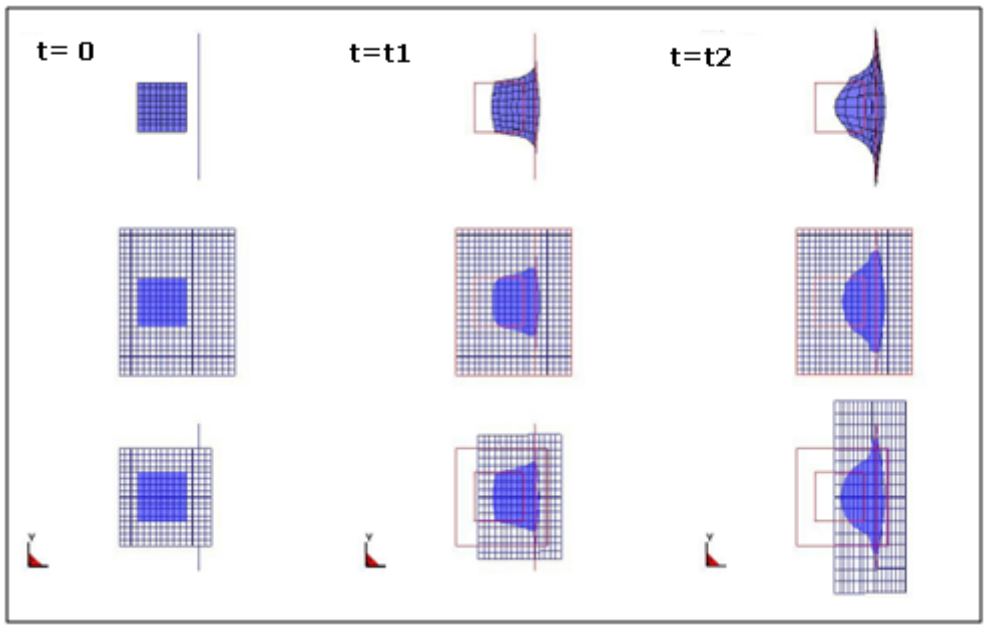

Figure 3.6 Comparison of Lagrange (top row), Eulerian (middle row) and ALE (bottom row) techniques [24].

Another similar comparison study is made by M'hamed Souli [25] regarding elastic ball impact in LS-DYNA. Two methods, ALE and Lagrangian technique, were imposed in this study. An elastic ball was impacted to a rigid surface by ALE and Lagrangian technique. As it can be seen in Figure 3.7 (right), the elements are exposed to high distortions across the impact interface due to the deformation of the ball in Lagrangian technique. However, in the ALE technique (left), the background mesh in which elastic ball flows is not distorted excessively with the deformation of elastic ball.

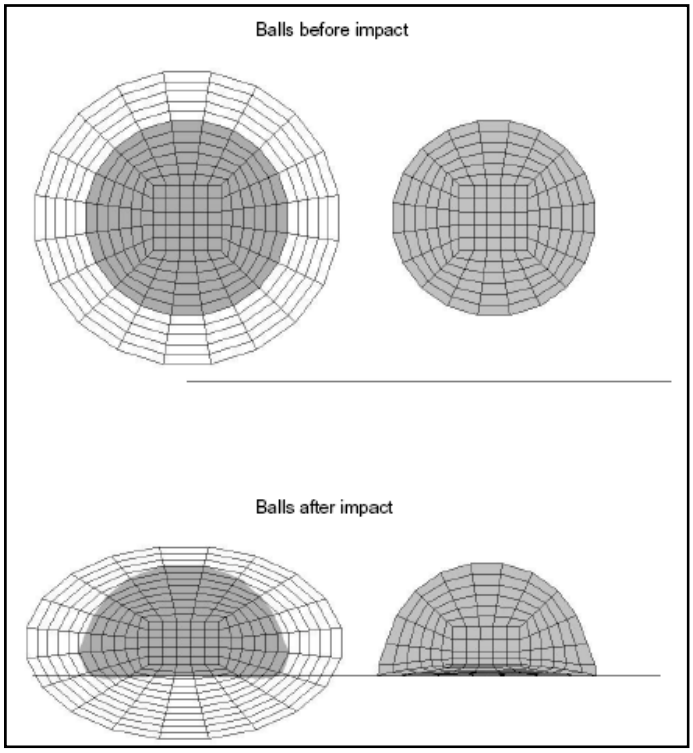

Figure 3.7 Impact of a elastic ball to a rigid surface in ALE (left column) and Lagrangian (right column) Method [25].

3.3 Modeling of Geometries Used in Numerical Simulation

Three different media are used in the numerical simulation. The first one is the water which is used for the impactor in the numerical simulation. The second one is the void which is required for the ALE technique. The void is the spatial coordinates and explained in previous section. The last one is the germanium which is the target material. Since there is no 2-D axis-symmetric ALE elements in Ls-Dyna Rev. 7600.398, full model are used for all geometries.

These three geometries can be divided into two groups. The first group consists of the water and void and can be called as ALE group of the simulation. Since water is exposed to large deformations throughout the simulation, water and void constitute the ALE part of the simulation. However, there is no need to use ALE technique for

the germanium because there are no large deformations are expected. The only initiation of damage is aimed to be investigated within the scope of this thesis. Therefore the second group only includes the germanium and called as Lagrangian group.

These all three media are explained separately in this section. Geometrical and mesh properties are described for each media with the help of representative figures.

3.3.1 Water

In numerical simulations, water is used in two different shapes which are water drop and water jet. These water shapes are determined according to the different test techniques. In whirling arm test technique (Section 2.4.1), water makes a free fall motion and can keep its drop shape. On the other hand, it is certain that, the aerodynamic forces occurred in front of the sample can change the pure drop shape of the water slightly due to the high rotational velocities in the whirling arm test technique. However, since the modeling of these kinds of shapes is relatively hard in the ALE technique, the water is simply assumed as sphere. However, in SIJA and MIJA (Section 2.4.2 and 2.4.3), the water is pushed from a nozzle at high velocities, such as 150 m/s. In this case, the shape of the water resembles to water jet due to the high loading applied on the water before the impact. Because of that, the second water geometry is selected as the water jet. The quarter views of both water shapes are shown in Figure 3.8.

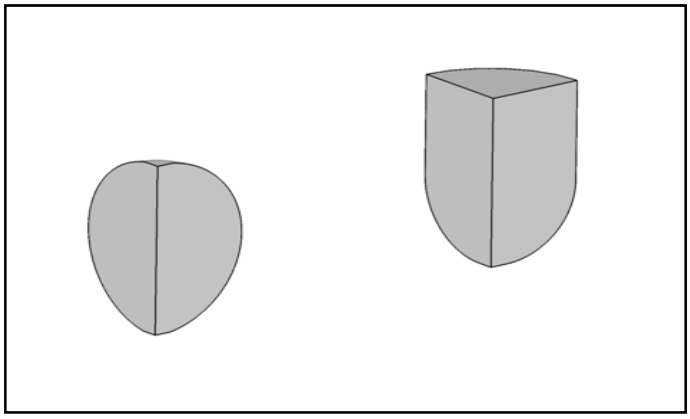

Figure 3.8 Quarter views of water drop (left) and water jet (right).

3.3.2 Void (Background Mesh / Spatial Coordinates)

The void represents the background mesh or spatial coordinates in the definition of ALE technique. In ALE solution technique, whole periphery of the fluid should be surrounded by the void completely at t=0. So that, the shape of the void may be a cylinder from which the water geometry is subtracted. Since there are two different water shapes, two corresponding voids should be prepared. The quarter views of the modeled voids are shown in Figure 3.9.

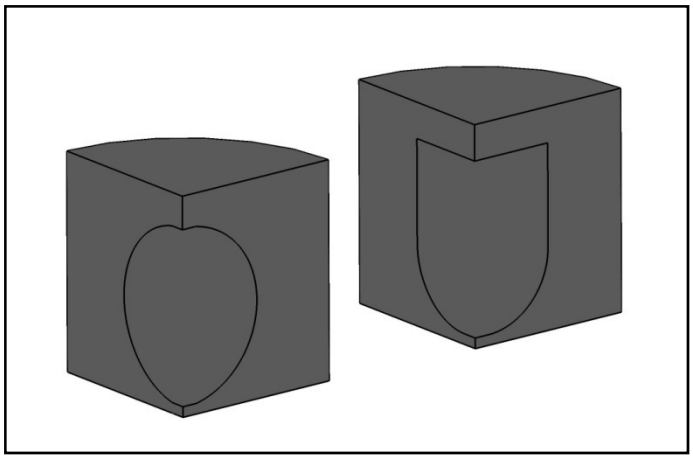

Figure 3.9 Quarter views of voids for water drop (left) and water jet (right).

3.3.3 Water and Void (First Group: ALE Group)

In order to make a correspondence between void and water, the all nodes on the outer surface of the water should be in consistent with the nodes on the cutout surface of the void. The nodes at this contact surface should be shared between the both geometries. Because of that these two surfaces have the nodes in the same order initially. So that, when these two parts are assembled, all the interface nodes can be coincident. After these arrangements are established, these coincident nodes are merged/shared so that two separate nodes (one of them belongs to the water and the other belongs to the void) at same location reduce to a single node.

The elements and the nodes of each part are shown in Figure 3.10. In this 2-D representation, the water (left) and the void (right) can be seen separately. The Figure 3.10 stands just for understanding the establishment of the node arrangement in the ALE technique. The meshing operation of each part has been done one by one and the location of the nodes at the contact surface is adjusted in the same order.

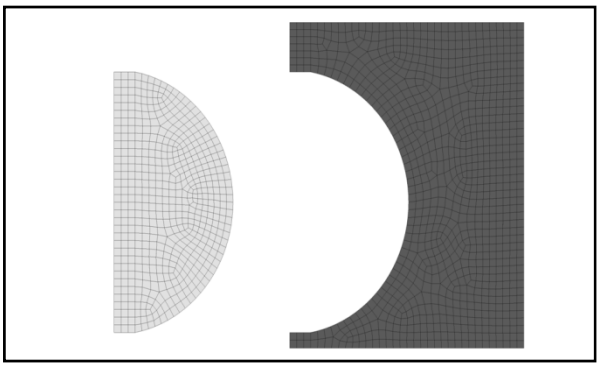

Figure 3.10 Node arrangement for water (left) and void (right).

The united configuration of water and void is shown in Figure 3.11. The all nodes on the water-void interface boundary are merged in this figure. These nodes are shared and belong to both water and void.

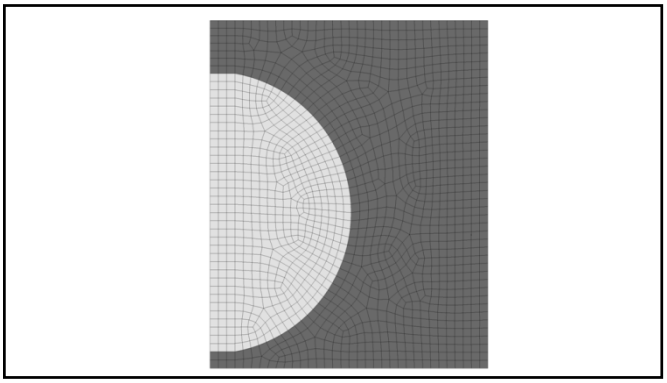

Figure 3.11 Merged/shared nodes in water-void boundary.

After the geometrical constraints and mesh consistency between the water and void are established, geometrical the modeling of the ALE group can be finished. The assembled configuration of water-void geometries are shown in Figure 3.12 for both water drop and water jet.

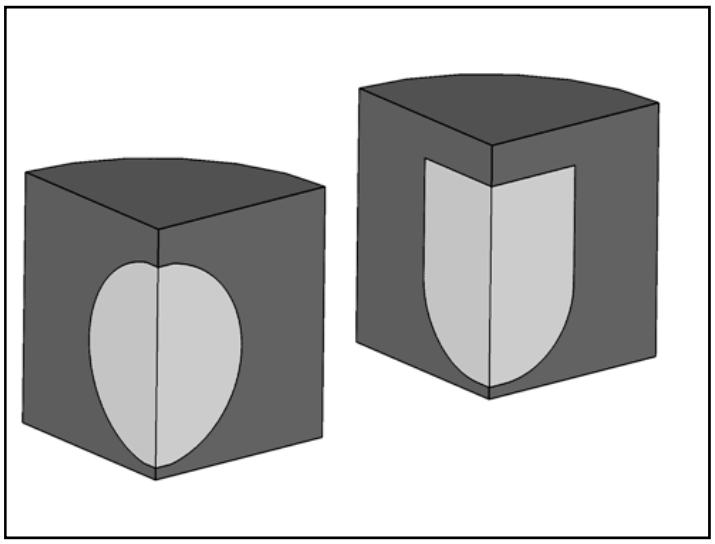

Figure 3.12 Quarter views of assembled water and void configurations for water drop (left) and water jet (right).

3.3.4 Germanium (Second Group: Lagrange Group)

The second group only consists of the target material germanium which is the third part of simulation. The mesh arrangement is done by Lagrangian method and there is no need to use an extra part such as void.

The target material is a cylinder disc which has a diameter of 25 mm and thickness of 5 mm. These dimensions are selected according to the specimens used in the experiment and is clearly mentioned in Chapter 4. The general view of the germanium is shown in Figure 3.13.

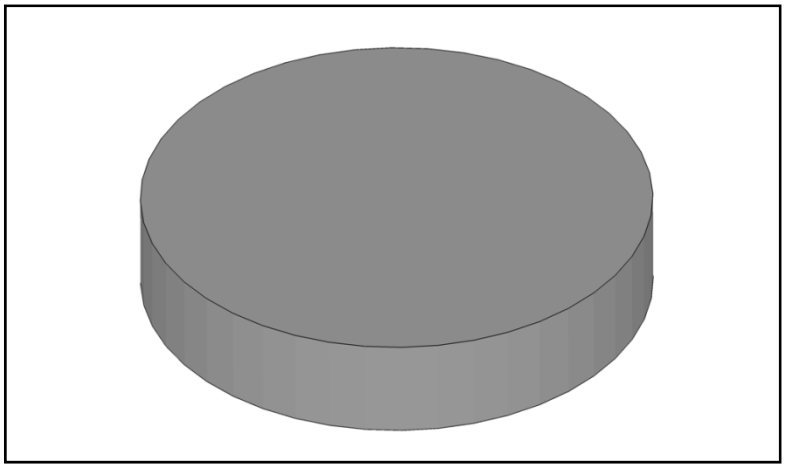

Figure 3.13 General view of the germanium (diameter = 25mm, thickness = 5mm).

3.4 Fluid – Solid Coupling

The simulations that include the interaction of a fluid with solid is known as FSI (Fluid Solid Interaction) and requires a special coupling algorithm. This coupling is generated between solid which is constructed generally using Lagrangian elements and fluid which is constructed using ALE (or Eulerian) elements. This coupling based on penalty formulation which tracks the relative displacements between the Lagrangian surface and ALE fluid elements [26]. LS-DYNA always seeks an

intersection between the Lagrangian and ALE elements. When the intersection is detected, the independent motion of two materials is tracked over the current time step and afterwards penetration distance is computed. Then coupling forces computed from penetrations are distributed to both materials.

This process is seen in Figure 3.14 between Lagrangian shell elements and Eulerian material. The point X which is on the Eulerian material is at the fluid-solid interface initially at left. When the shell elements start to move into Eulerian elements, penetration occurs and this penetration creates the coupling forces [27].

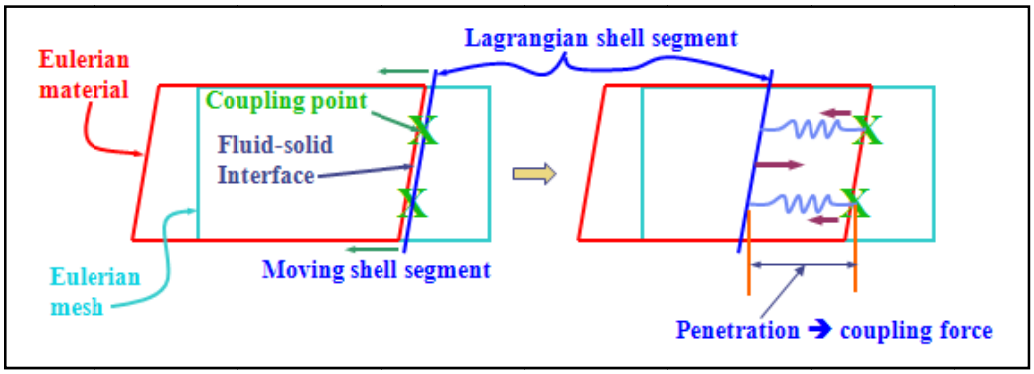

Figure 3.14 Coupling between Lagrangian and Eulerian methods [27].

The coupling algorithm between solid and fluid can be constructed by using CONSTRAINT_LAGRANGE_IN_SOLID card in LS-DYNA. Details of this card can be found in the LS-DYNA user's manual [28].

3.5 Material Models

Nonlinear, explicit finite element programs need material models in order to define the behaviour of the materials throughout the simulation. The material models are actually the mathematical formulations by which the response of the material is settled down. These mathematical expressions in some material models may require very complex parameters/constants in order to define.

Different material models may come up with the different results. So, the material model selection and determination of its parameters properly play very important role in explicit simulations.

There are two different material models needed for this study. Water and void use the same and one material model according to definition of the single material ALE [28]. The other one is required for the germanium.

3.5.1 Material Model for Water and Void

Water is generally represented by MAT_NULL material model in LS-DYNA [29], because the null material has no yield strength and behaves in a fluid-like manner. However, this material model needs an EOS (Equation of State) in order to simulate behaviour of the fluid material. The EOS calculates the hydrostatic pressure in the material. EOS is needed in the situations such that; when the pressure in the material is far in excess of yield stress and/or when there are high strain rates [30].

There are EOS formulations for different applications such as water, air, explosive etc., in the library of the LS-DYNA. An appropriate and the most common EOS in the literature is EOS-GRUNEISEN for water applications such as [31], [32], [33], [34]. MAT_NULL + EOS_GRUNEISEN combination is also used in the current study for both water and void and the constants are given in Table 3.1. Density is defined in MAT_NULL card and the other parameters are defined in the EOS_GRUNEISEN card.

Table 3.1 Gruneisen Constants for Water [31], [34].

SYMBOL	PROPERTY	WATER VALUE
ρ_0	Initial Density	1000 kg.m^{-3}
C_0	Shock velocity	1484 m.s^{-1}
S_1	Material constant	1.979
S_2	Material constant	0
S_3	Material constant	0
γ_0	Material constant	0.11
a	Material constant	0
E_i	Initial internal energy	0
V_i	Initial relative volume	0

The pressure in the compressed material is defined as [34]:

$$P = \left[\frac{\rho_0 {C_0}^2 \mu \left[1 + \left(1 - \frac{\gamma_0}{2}\right)\mu - \frac{a}{2}\mu^2\right]}{\left[1 - (S_1 - 1)\mu - S_2 \frac{\mu^2}{\mu + 1} - S_3 \frac{\mu^3}{(\mu + 1)^2}\right]^2}\right] + (\gamma_0 + a\mu)E_i \qquad (3.1)$$

where: $\mu = {\rho}/{\rho_0} - 1$.

3.5.2 Material Model for Target Plate (Germanium)

The other material model is required for target plate germanium which is generally used as infrared window of the EO devices. Germanium is brittle, silverly-white, semi-metallic element under normal conditions.

3.5.2.1 Selection of the Material Model for Germanium

In real life, use of ductile materials such as metal, composite, plastic etc., is much more common than brittle materials. Therefore, most of the material models in the library of the LS-DYNA are for the ductile materials such as steel or aluminium.

All options can be reviewed / assessed in order to make a good selection for germanium in the LS-DYNA library. Material Model Reference Table in the LS-DYNA Keyword User's Manual [28] is a good comparison tool for this operation. All the material models in LS-DYNA library are listed in this table and basic properties such as strain rate effects, failure criteria, damage effects, EOS etc. are presented. Moreover, the applications such as composite, metal, ceramics, glass, fluid, foam etc. are also given in the same table.

Ceramics are the general name of the window and dome materials used in the EO devices [7] so that, ceramics applications are well suited to germanium. Moreover, since the germanium is a kind of glass also, the Material Model Reference Table is reduced only for the Ceramics and/or Glass applications as shown in Table 3.2. In order to understand this reduced table well, the explanations made in the LS-DYNA Keyword User's Manual [28] is exactly given here:

> *If a material model includes any of the following attributes, a "Y" will appear in the respective column of the table:*
>
> *SRATE* - *Strain-rate effects*
> *FAIL* - *Failure criteria*
> *EOS* - *Equation of state required for 3D solids and 2D continuum elements.*
> *THERM* - *Thermal effects*
> *ANISO* - *Anisotropic/orthotropic*
> *DAM* - *Damage effects*

TENS - *Tension handled differently than compression in some manner*

Potential applications of the material models, in terms of classes of physical materials, are abbreviated in the table as follows:

GN - *General*
CM - *Composite*
CR - *Ceramic*
FL - *Fluid*
FM - *Foam*
GL - *Glass*
HY - *Hydrodynamic material*
MT - *Metal*
PL - *Plastic*
RB - *Rubber*
SL - *Soil, concrete, or rock*
AD - *Adhesive*
BIO - *Biological material*
CIV - *Civil Engineering Components* [28].

Table 3.2 The Material Model Reference Table (Reduced for the Ceramic and Glass Applications) [28].

Material Number and Description	**SRATE**	**FAIL**	**EOS**	**THERM**	**ANISO**	**DAM**	**TENS**	**Application**
MAT17-Oriented Crack (Elastoplastic w/ Fracture)		Y	Y		Y		Y	HY, MT, PL,**CR**
MAT32-Laminated Glass (Composite)		Y						CM, **GL**
MAT33-Barlat Anisotropic Plasticity (YLD96)	Y				Y			**CR**, MT
MAT59-Composite Failure (Plasticity Based)		Y			Y		Y	CM, **CR**
MAT60-Elastic with Viscosity (Viscous Glass)	Y			Y				**GL**
MAT110-Johnson Holmquist Ceramics (JH-2)	Y	Y				Y	Y	**CR, GL**

The all material model options for the target material germanium are listed in Table 3.2. Among the listed choices for the germanium above; MAT17, MAT33, MAT59 is for ceramic applications and MAT32, MAT60 is for glass applications. However, MAT32, MAT33, MAT59 and MAT60 have no damage effects. MAT33 and MAT60 have no failure criteria either. MAT17 needs an EOS definition separately for the pressure constants in order to work and has no damage effect either.

In addition to these mentioned material models, MAT110 is recommended for both ceramics and glass applications in the reference table. MAT110 contains damage effects and failure criteria together that are useful tools in post processing.

Furthermore, JH-2 is a complete material model which has also the EOS constants at the same time and there is no need to utilize a separate EOS formulation for this material model.

Consideration of all these suggestions together makes MAT110 (Johnson Holmquist Ceramics – JH2) the most appropriate choice among the other mentioned alternatives for the germanium in the present study.

3.5.2.2 Johnson Holmquist Ceramic Material Models

Johnson Holmquist ceramic models are in three types: JH-1 (Johnson and Holmquist, 1992), JH-2 (Johnson and Holmquist, 1994) and JH-3 (Johnson, Holmquist, and Beissel, 2003). All of these models have damage parameter that shows the state of the ceramic material varying from intact to completely fractured. The strength of the material is defined in two boundaries which are intact and fractured. The main difference of the JH-1 and JH-2 is the exactly right here. The JH-1 model [35] is not designed to give any response between these two boundaries. So, only completely intact and completely fractured state can be seen while the material undergoes transformation from the intact state to the fractured state under the applied load. However, in this transformation region the damage is being accumulated and JH-2 model [36] captures all this progress in the material during the simulation. In other words, the JH-2 model incorporates a mechanism of gradual decrease of strength (damage evolution rule) and accumulation of bulking pressure as damage increases [37].

The JH-3 model given by Johnson and Holmquist [38] is the latest version of the JH models and incorporates most features of the JH-2 model with a modification (simplification) on shape of the strength envelope. The capability to include a phase change under the conditions of high velocity impact is the primary new feature of this model. Moreover, projectile dwell phenomena can be more accurately simulated

in the JH-3 model than the JH-2 model as explained by Gazonas [39].

Since multiple impact case is thought in this study, damage proceeds progressively at each impact in the material. So that, JH-2 model more convenient material model than JH-1 for the present study since JH-2 material model allows for gradual softening of the material under the increasing plastic strain. Furthermore, since there is no need to model projectile dwell phenomena in the simulation of rain erosion, the JH-2 model is also more convenient than the JH-3 model. Therefore, JH-2 model which is already implemented and validated into LS-DYNA [40] is used for this thesis.

3.5.2.3 Johnson Holmquist Ceramic 2 (JH-2) Description

JH-2 material model is improved for brittle materials such as ceramics and glass subjected to large strains, high strain rates and high pressures by G. R. Johnson and T. J. Holmquist and is compatible with both the Lagrangian and Eulerian codes. There are mainly three set of equations within the body of the material model. These equations control the strength, damage and pressure in the material as shown in Figure 3.15.

The strength of the material is defined as [36]:

$$\sigma^* = \sigma_i^* - D(\sigma_i^* - \sigma_f^*), \qquad (2.1)$$

where, σ_i^* is the normalized intact equivalent stress, σ_f^* is the normalized fracture stress, and D is the damage $(0 \leq D \leq 1)$. When D = 0 the material is said to be intact, and when D = 1 the material is completely damaged or fractured. Between 0 and 1, material softens gradually with increasing plastic strain in JH-2 model.

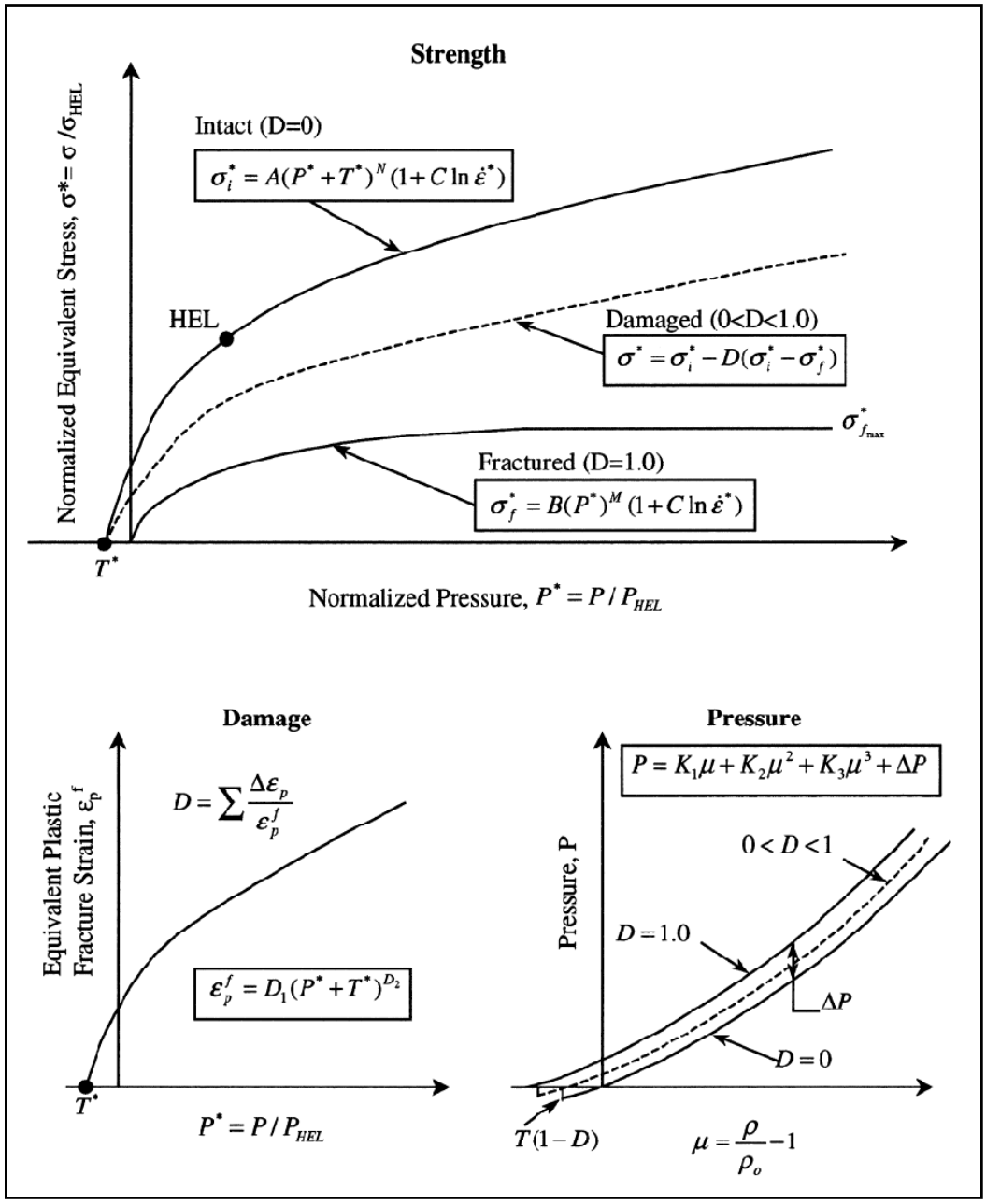

Figure 3.15 Description of the JH-2 ceramic model [36].

The general form of the normalized equivalent stresses $(\sigma^*, \sigma_i^*, \sigma_f^*)$ is [36]:

$$\sigma^* = \sigma / \sigma_{HEL}, \tag{2.2}$$

where, σ is the actual equivalent stress and σ_{HEL} is the equivalent stress at the Hugoniot elastic limit (HEL). The equivalent stress is [41]:

$$\sigma = \sqrt{1/2\left[(\sigma_x - \sigma_y)^2 + (\sigma_x - \sigma_z)^2 + (\sigma_y - \sigma_z)^2 + 6(\tau_{xy}^2 + \tau_{xz}^2 + \tau_{yz}^2)\right]} \qquad (2.3)$$

where, σ_x, σ_y and σ_z are the three normal stresses, and τ_{xy}, τ_{xz} and τ_{yz} are the three shear stresses.

The normalized intact strength in the material is defined by [36]:

$$\sigma_i^* = A(P^* + T^*)^N(1 + C \ln \dot{\varepsilon}^*) \qquad (2.4)$$

and, the normalized fracture strength is defined by [36]:

$$\sigma_f^* = B(P^*)^M(1 + C \ln \dot{\varepsilon}^*), \qquad (2.5)$$

The material constants are A, B, C, M, N and σ_{fmax}^*. The normalized maximum tensile hydrostatic pressure is $T^* = T/P_{HEL}$, where T is the maximum tensile hydrostatic pressure the material can withstand. The normalized pressure is $P^* = P/P_{HEL}$, where P is the actual pressure and P_{HEL} is the pressure at the HEL. The dimensionless strain rate is $\dot{\varepsilon}^* = \dot{\varepsilon}/\dot{\varepsilon}_0$, where $\dot{\varepsilon}$ is the actual equivalent strain rate and $\dot{\varepsilon}_0 = 1.0s^{-1}$ is the reference strain rate.

In a study [41] in which the determination of the constants of the JH-2 model is explained in detail, there is a statement regarding T^* that; "T^* is the maximum hydrostatic tensile pressure, or spherical stress, the material can withstand and the authors are not aware of any test technique that is capable of explicitly determining its value. The parameter T^* is obtained indirectly by using the model and experimental data. The general form of Equation 2.4 is driven through the HEL, the spall, and an estimate of the high rate uniaxial compressive strength and then

Equation 2.4 is solved for T^*" [41].

The damage for fracture is accumulated with this expression [36]:

$$D = \sum \Delta \varepsilon_p / \varepsilon_p^f, \tag{2.6}$$

where, $\Delta\varepsilon_p$ is the equivalent plastic strain during a cycle of integration and $\varepsilon_p^f = f(P)$ is the plastic strain to fracture under a constant pressure P. The specified expression is [36]:

$$\varepsilon_p^f = D_1(P^* + T^*)^{D_2}, \tag{2.7}$$

where, D_1 and D_2 are constants and P^* and T^* are as defined previously in Equation 2.4. According to Equation 2.7, the material cannot undergo any plastic strain at $P^* = -T^*$, but ε_p^f increases as P^* increases [36].

The hydrostatic pressure, prior to damage ($D = 0$), is [36]:

$$P = K_1\mu + K_2\mu^2 + K_3\mu^3, \tag{2.8}$$

where, K_1, K_2 and K_3 are constants and $\mu = \rho/\rho_0 - 1$ for current density ρ and initial density ρ_0. For tensile pressure ($\mu < 0$), Equation 2.8 is replaced by $P = K_1\mu$ [36].

3.5.2.4 Determination constants of JH-2 model for Germanium

JH-2 material model constants are comparatively hard to define relative to the other material models in LS-DYNA. There are mainly four categories for the constants in JH-2 model apart from the density. They are elastic, damage, pressure and strength

constants. Since the JH-2 material model reflects the dynamic properties, defining the constants of JH-2 model for a specific material requires a several dynamic experiments and corresponding test setups. After gaining the results from the experiments, some special methods are used to reach the value of the constants of the JH-2 model.

In ASELSAN Documentation System there is a report for JH-2 constants of germanium [42]. This report which is prepared by Mustafa Güden and Alper Taşdemir in İzmir Yüksek Teknoloji Enstitüsü includes the results of the tests for the determination of JH-2 constants. The germanium samples which are needed for both dynamic and static experiments were also provided by ASELSAN. The detailed information regarding the test methods and all other required knowledge about determining the constants of the JH-2 model is available in the work by Holmquist [41].

3.6 Mesh Sensitivity Analysis

Four models were prepared with different element sizes for the mesh sensitivity analyses. Spherical water drop was used in the mesh sensitivity analyses. The only difference between the four models is the size of the used elements. Water drop is impacted to germanium at 250 m/s in each model. The general view of the model is shown in Figure 3.16 and dimensions are given in the Table 3.3.

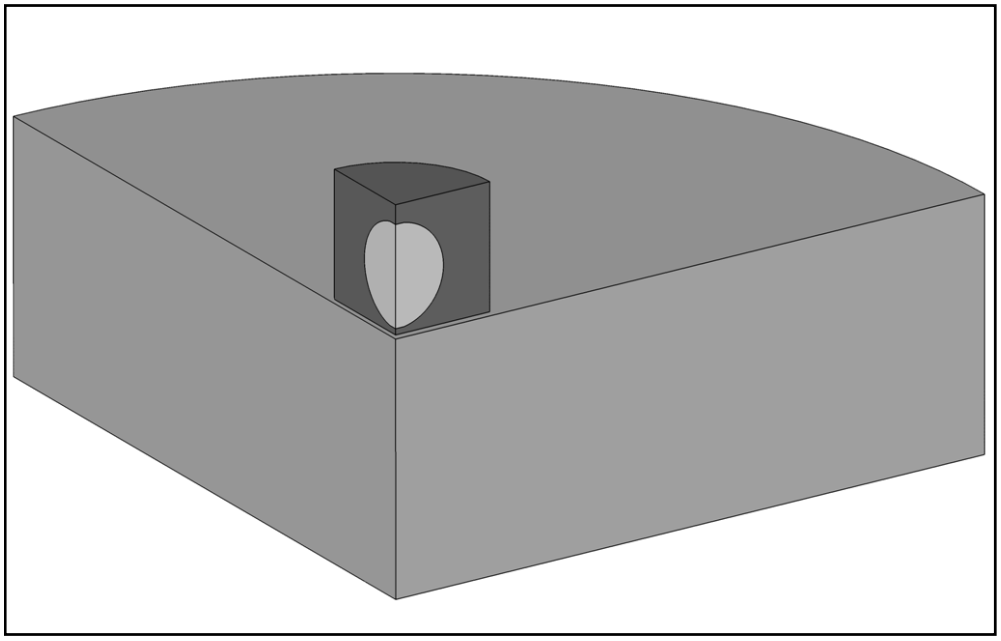

Figure 3.16 General view of the sensitivity model.

Table 3.3 Dimensions of the sensitivity model.

	Radius (mm)	Length (mm)
Void	2	2.5
Water, spherical	1	2
Germanium	12.5	5

Variable size is used for the elements in the germanium model. Since the impact is occurred at the center of the target material, using variable mesh sizes and concentrating on the centre is more feasible. So, the smallest elements are located at the centre and the size of the mesh is progressively increases with a convenient proportion from centre. At each model the increasing ratio of the elements are also the same. Water and void are meshed with the same element sizes which have been used at the centre of the corresponding germanium model.

The first model which is labeled with capital letter “A” is the coarsest model and shown in Figure 3.17 below. There are 40 elements in the radial direction, 44 elements in circumferential direction and 21 elements through the thickness. The radial length of the elements at the center is 0.125 mm and progressively increases to 0.65 mm at the perimeter. There are totally 40364 solid element used for Model A. Similarly, models with finer elements are created in models B, C and D. The number of elements is given in Table 3.4.

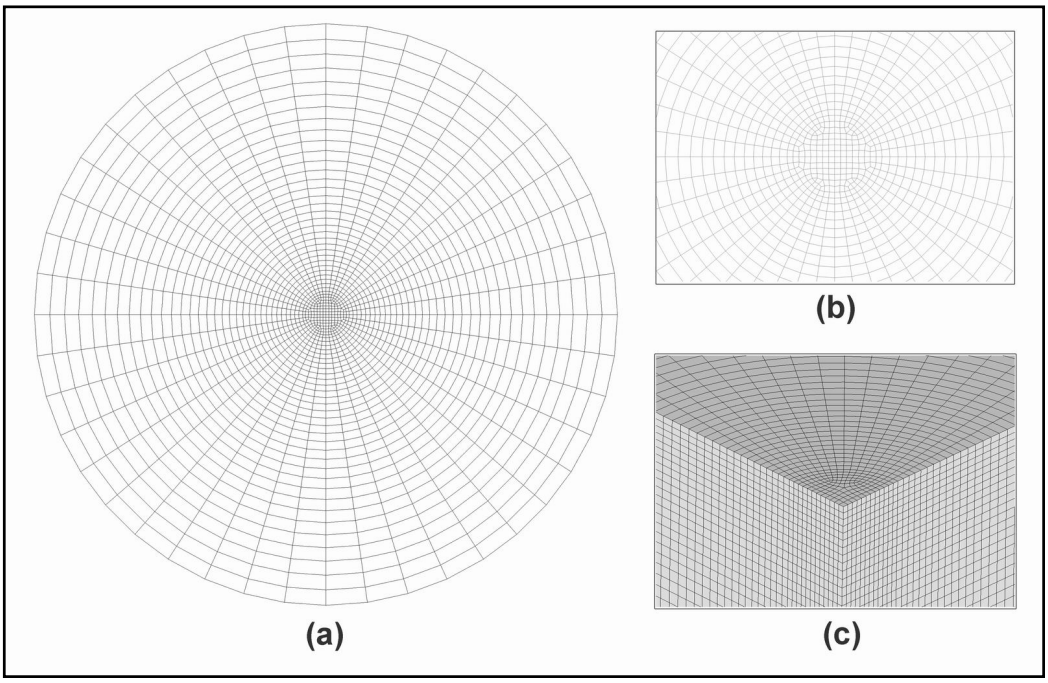

Figure 3.17 Sensitivity model A; (a) top view, (b) detail view at the centre, (c) detailed view through the thickness.

Table 3.4 Properties of the sensitivity models.

	MODEL A	MODEL B	MODEL C	MODEL D
Number of elements in radial direction	40	64	84	102
Number of elements in the circumferential direction	44	72	96	116
Number of elements through the thickness	21	32	42	66
Number of total elements	40364	147920	346008	939724
Radial size of the elements at centre / at perimeter [mm]	0.125 / 0.65	0.083 / 0.4	0.0625 / 0.3	0.05 / 0.25
Thickness of the elements on surface / at bottom [mm]	0.072 / 0.36	0.072 / 0.24	0.072 / 0.18	0.072 / 0.12
Run Times [seconds (minutes)]	75 (1.1)	288 (4.5)	708 (11.5)	3180 (53.0)

At every model, two measurement stations are defined at the R=0 and R=0.5 as it can be seen in Figure 3.18. The size of these stations is 0.25 mm X 0.25 mm in each model and consists of only the top layer elements in the germanium. There are only 4 elements filled this area for model A and number of elements at the same area increases to 9, 16 and 25 in models B, C and D respectively. In order to obtain the same volume for the measurement stations, the thickness of the top layer elements is kept constant at each model. Therefore, two stations with equal size and volume in each model are created for the sensitivity models.

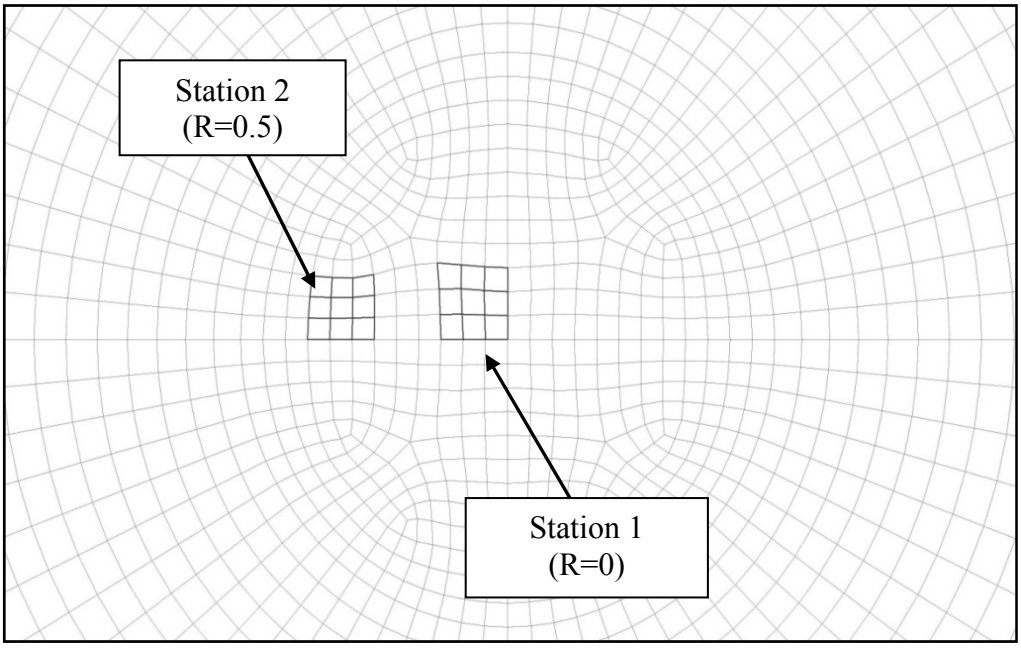

Figure 3.18 Location of the measurement stations on model B.

As it is known that the maximum principal stress theory is very useful for the brittle materials as the yield criterion. According to this theory failure occurs when the maximum principal stress in a system reaches a value that is over the elastic limit of the material in simple tension. Since the germanium is also a brittle material, the principal stresses are thought to be convenient for the comparison of the models within the scope of the mesh sensitivity analyses. Moreover, since the stresses in the germanium are dominantly compressive, the minimum principal stress graphs are also plotted at two measurement stations for the comparison of the models.

The stresses for the selected elements inside the mentioned stations are saved throughout the simulation for each model. In order to make a true comparison, the average values of these elements are taken for both stations. The first two figures (Figure 3.19 and Figure 3.20) show the maximum and minimum principal stresses of the elements at R=0. It is seen that stresses are always the compressive throughout the simulation for both graphs at the center. As the size of the elements is reduced, both the amount of the peak values and the difference between the models decreases

at nearly one microsecond. So, at t=1 μs, the curves converge to each other with peak values of -75 MPa for maximum and -350 Mpa for minimum principal stresses in Figure 3.19 and Figure 3.20 respectively.

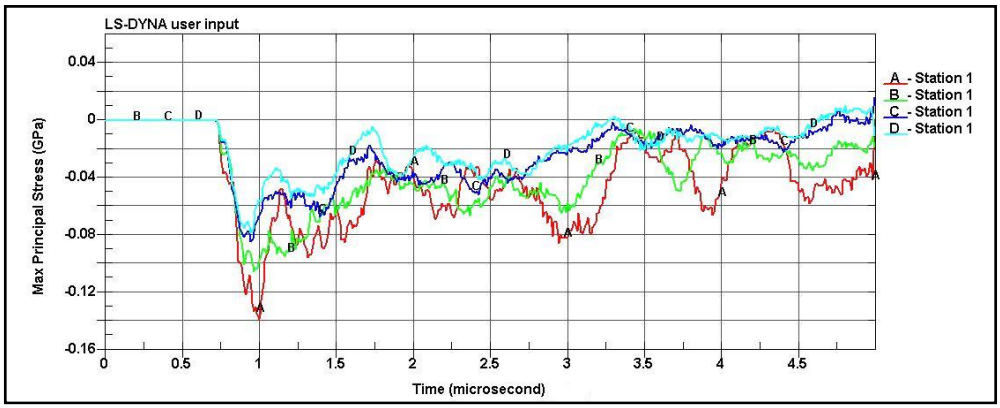

Figure 3.19 Maximum Principal Stress at R=0 (Station 1).

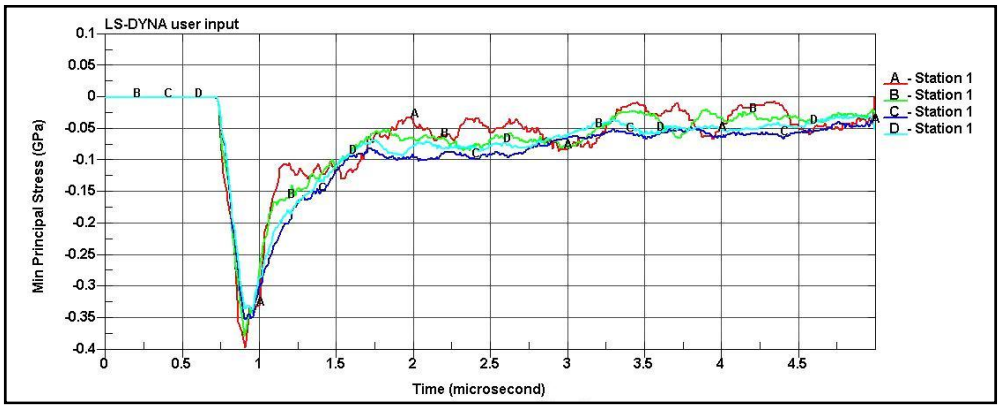

Figure 3.20 Minimum Principal Stress at R=0 (Station 1).

In a similar way, the maximum and the minimum principal stresses are measured for R=0.5 mm station. In contrast to central zone, there is a tensile region for a short duration between 0.8 and 1.25 microseconds in Figure 3.21 due to the tensile stresses seen at the xx and yy directions at the same interval of the time. On the other hand, the minimum principal stresses are compressive at R=0.5 as it can be seen in the

Figure 3.22.

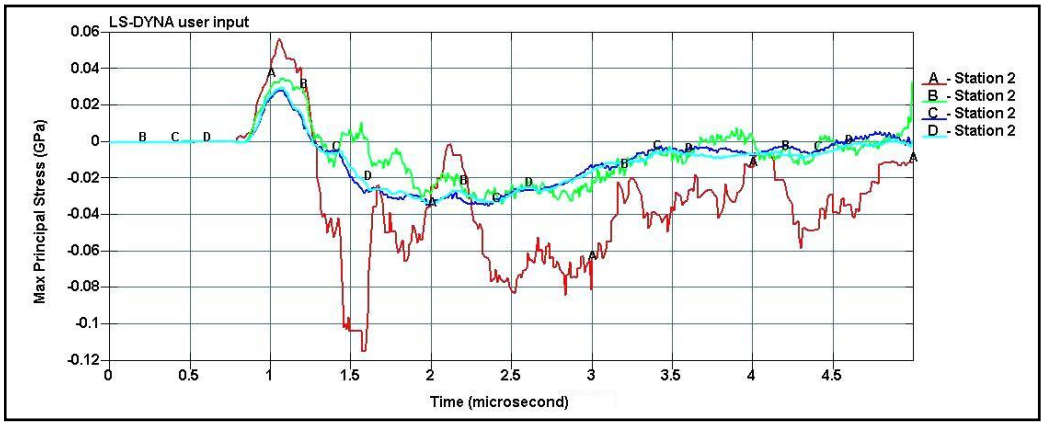

Figure 3.21 Maximum Principal Stress at R=0.5 (Station 2).

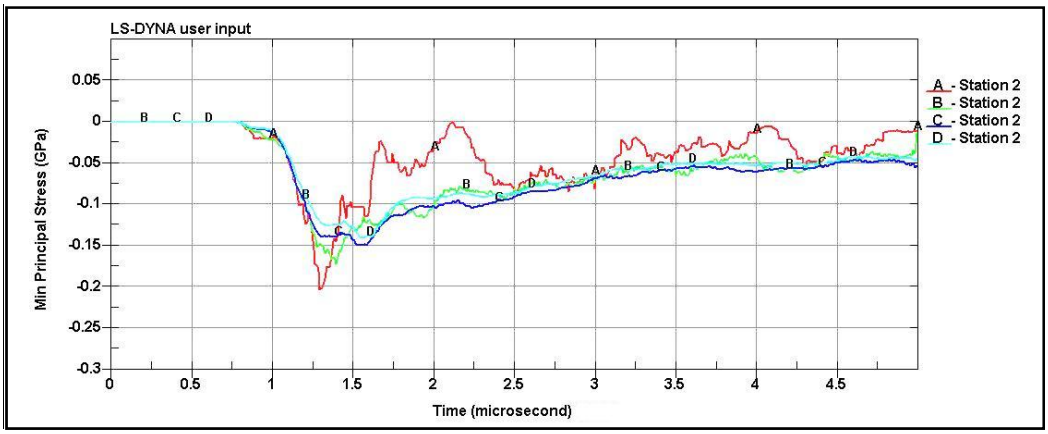

Figure 3.22 Minimum Principal Stress at R=0.5 (Station 2).

It seen in all the figures that, the peak values converge to the model D which is the finest among the all sensitivity models. However, since the values for model C are very close to the model D in the all graphs, the convergence is said to be satisfied for model C especially for Figure 3.20 and Figure 3.21. Keeping in mind that, since the run time for model D is about 5 times greater than that of model C, one can sacrifice some amount of accuracy for gaining from the run time. Therefore, model C is used for the further simulations regarding the rain erosion throughout the current thesis.

CHAPTER 4

TEST FACILITY AND EXPERIMENT CONDITIONS

In the experiment of the rain erosion within the scope of the current study, whirling arm technique, mentioned and described briefly in Section 2.4.1, was used. This section covers description of the test facility and experimental conditions. The whirling arm experiment was performed in SAAB Aerosystems in Sweden and financial support was provided by ASELSAN.

4.1 Description of the Test Facility

The general view of the test facility is shown in Figure 4.1. In the whirling arm test technique the specimen is mounted at the end of a rotating arm which can move centrifugally at different speeds. While this motion continues, the target material is exposed to rain erosion by the released water drops from the emitters. The rain emitters are placed at six places around the circler test field in order to provide the desired rain fall rate. In this test technique released water drops hit to the target randomly and number of the drops that hits to the specimen cannot be known exactly. However, there is an approach which is explained at the end of this chapter (Section 4.3) that estimates the number of rain drops which impacts to the target in a specified rain fall rate with respect to diameter of the water drop, impact velocity, duration time and terminal velocity of the water drop.

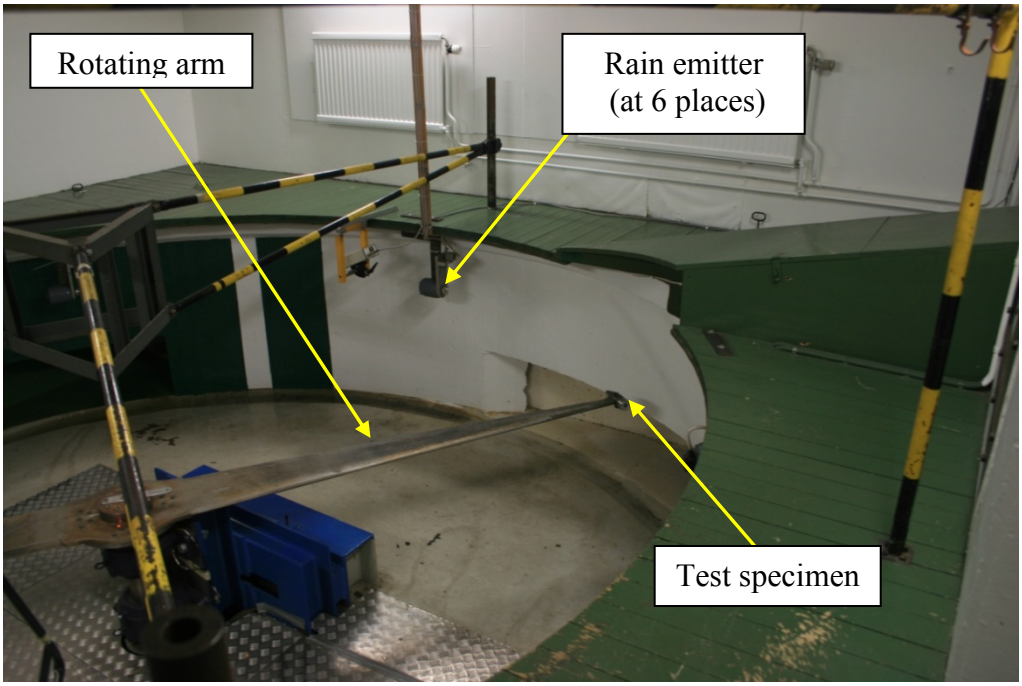

Figure 4.1 General view of the test facility.

Technical details of the test facility [43] are below:

Dimensions:

- Arm radius : 2.19 m
- Number of the Rain emitter : 6
- Test specimen : 50 mm

Performance:

- Speed range : 0-300 m/s
- Drop size : 1.2, 1.6 and 2 mm (Mean diameter)
- Rain density : From 1.4 mm/h to 25 mm/h in 16 steps
- Attact angles : 90^0, 60^0, 45^0

Rain density is the fall rate of the water droplets on a flat surface and generally given by the length of the fluid accumulated after a certain amount of time such as one hour. In order to measure the density of a natural rain in a region, a reservoir in which the water is collected can be used. For example, 25 mm/hour of rainfall is equivalent of 25 litres of water per square meter in one hour.

The components of the test facility are shown in Figure 4.2. After required rain fall rate adjusted on the rain emitters, the arm starts rotating with a constant velocity. At each tour, the rotating arm passes through the six rain emitters located symmetrically in the test field. According to the rain fall rate, the specimen exposed to liquid impact at each time when the rotating arm at the bottom of the rain emitters as shown in Figure 4.3. As the rain fall rate increases, the number of impact also increases at each tour of the rotating arm. Similarly, as the velocity of the rotating arm increases, the number of completed tour increases at fixed test duration (for example 5 minutes), and number of liquid impact increases too.

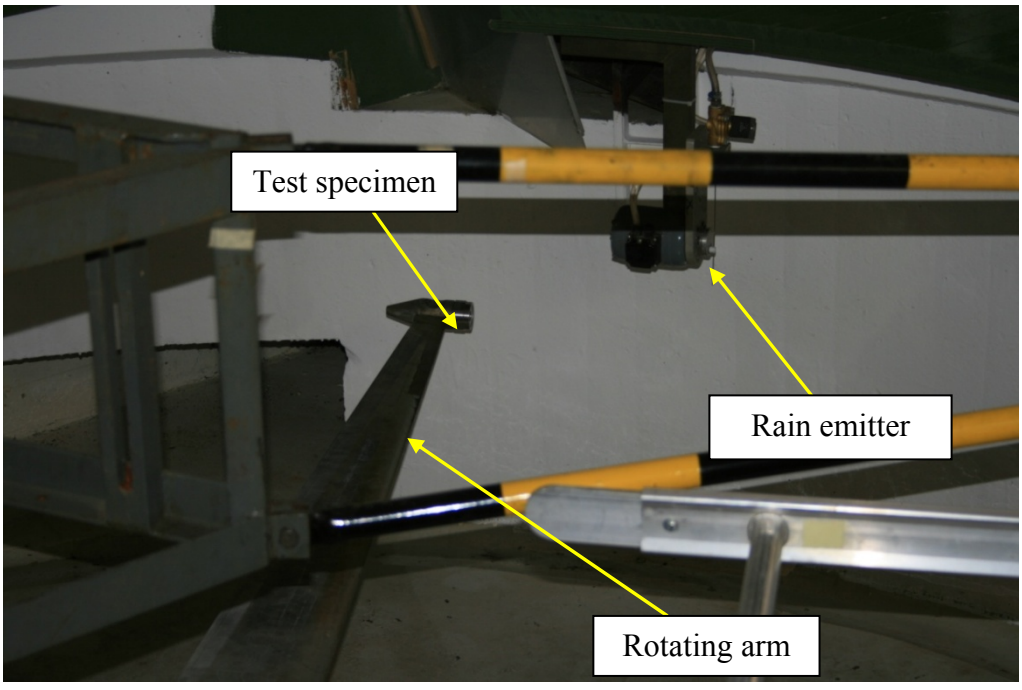

Figure 4.2 Rotating arm, rain emitter and test specimen.

Figure 4.3 When the test specimen passes below a rain emitter.

The mounting of the specimen at the end of the rotating arm is shown in Figure 4.4. The dimensions of all specimens are the same and the shape is cylindrical with 25 mm in diameter and 5 mm in height within the scope of the current study. The specimen is fixed at the bottom surface as it is understood from the Figure 4.4. And, since the centrifugal force is applied to specimen in the course of the experiment, the lateral surface of the specimen is also fixed.

Figure 4.4 Mounting of the test specimen on end of the rotating arm.

The adjustment of the rain fall rate is made by using a calibration reservoir which is seen in Figure 4.5. The amount of the water inside the capsule gives the rain intensity. After the desired intensity of the rain is acquired at the desired velocity, the test setup is ready for the experiment.

Table 4.1 shows the calibration study made by the authorized staff member. At different rotating arm velocities (50 m/s, 70 m/s, 150 m/s and 200 m/s), the rain fall rate was tried to be adjusted about 25 mm/h. Among the 10 tries, test number 2 is seen to be the best approximation for 50 m/s, test number 8 is the best for 70 m/s, test

number 6 is the best for 150 m/s and test number 7 is the best for 200 m/s.

Figure 4.5 Calibration reservoir for adjustment of the rain fall rate.

Table 4.1 Rain erosion rig calibration of rain intensity.

Rain Erosion Rig Calibration of Rain Intensity										
Test No	Drop dia	Rain Emiters	Run Time	Total Rounds	RPM	Speed	Collected Water	Density	Rainfall	Water Pressure
	Ø mm	number	s	r	r/min	m/s	g	ml/m3	mm/hr	kPa
1	2	6	600,0	2161	216,1	49,5	9,9	1,308	28,3	1,2
2	2	6	600,0	2183	218,3	50,0	8,7	1,138	24,6	1,2
3	2	6	600,0	2182	218,2	50,0	9,1	1,191	25,7	1,2
4	2	6	600,0	1325	132,5	30,3	5,9	1,272	27,5	1,2
5	2	6	600,0	3036	303,6	69,5	10,1	0,95	20,5	1,2
6	2	6	300,0	3282	656,4	150,3	13,0	1,131	24,4	1,2
7	2	6	300,0	4356	871,2	199,5	18,3	1,2	25,9	1,2
8	2	6	600,0	3045	304,5	69,7	13,1	1,229	26,5	1,2
9	2	6	300,0	3278	655,6	150,1	12,4	1,08	23,3	1,2
10	2	6	300,0	3285	657,0	150,5	12,4	1,078	23,3	1,2

Various materials can be tested against rain erosion under the specified environment conditions. There is an example of rain erosion damage on flexi glass, composite and glass fiber in Figure 4.6. Damage starts appearing at low speeds (100 m/s), and enhances while the velocity increases.

Figure 4.6 Test specimens subjected to rain at high speed [43].

4.2 Experimental Conditions

In the experimental there are three different velocities were used according to the environmental conditions that aerial platforms are exposed to. The specimens are cylindrical with 25 mm in diameter and 5mm in height as mentioned previously.

Velocity profiles and other conditions that the germanium specimens were tested are shown in Table 4.2 which is obtained from an internal report in ASELSAN [44]. The rain fall rate adjusted constant to 25 mm/h and diameter of the raindrops used in the

experiment is 2 mm. The all of the six rain emitters were used in the experiment.

Table 4.2 Test conditions for Germanium specimens.

Test protocol		Customer				Issued by		Date				
Rain Erosion Test		Aselsan A.S				TFG-KE		26.05.2009				
Date	Test Specimen	Rain emitters	Rain fall	Drop-size	Impact angle	Run time		Total rounds	RPM	Impact velocity	Weight before	Weight after
		number	mm/hr	Ø mm	deg.	min.	sec.	r	r/min	m/s	g	g
26.05.2009	44	6	25	2	90	5	0	1081	216,2	49,51	13,61	
26.05.2009	44	6	25	2	90	5	0	1523	304,6	69,753		
26.05.2009	44	6	25	2	90	5	0	1965	393	89,997		
26.05.2009	44	6	25	2	90	5	0	3278	655,6	150,13		
26.05.2009	44	6	25	2	90	5	0	4359	871,8	199,64		13,607
26.05.2009	45	6	25	2	90	5	0	3282	656,4	150,32	13,62	13,623
26.05.2009	46	6	25	2	90	5	0	2742	548,4	125,58		

Although the detailed microscopic views are to be presented in the next chapter (Section 5.2), the pictures of the specimens after the experiment are also given here. The specimen number 46, exposed to rain erosion at lowest impact velocity 125 m/s, can be seen in Figure 4.7. There is no damage is seen by normal eye in number 46. The next specimen is the number 45 which is seen in Figure 4.8 and some surface disorders can be distinguished relative to the number 46 specimen. The last specimen is the number 44 exposed to the worst condition can be seen in Figure 4.9. The damage can be seen even by a normal eye. Of course, microscopic views of these specimens which are presented in Section 5.2 are needed to be investigated in order to make a damage analysis.

Figure 4.7 Test specimen number 46 after experiment.

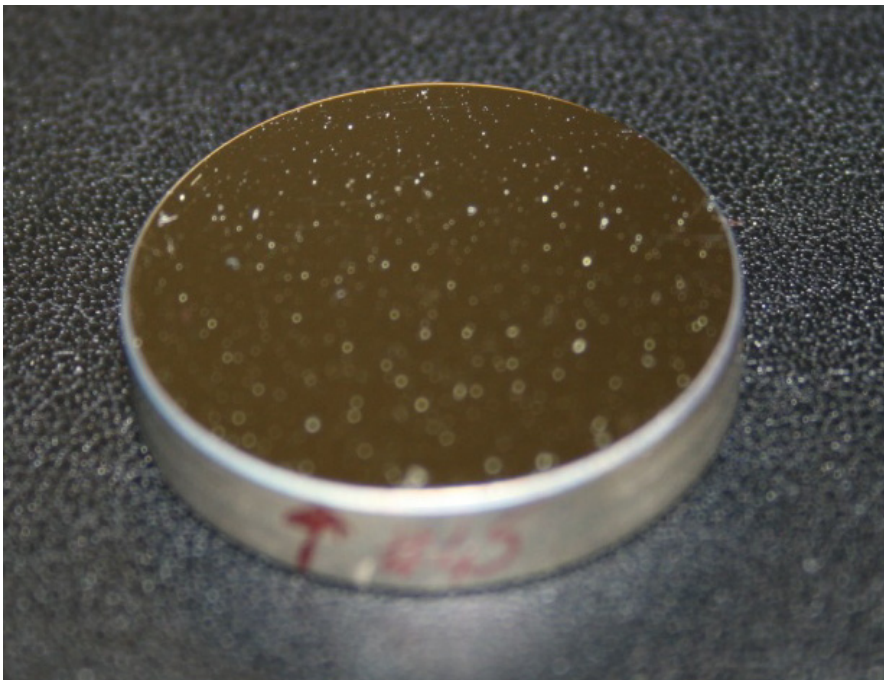

Figure 4.8 Test specimen number 45 after experiment.

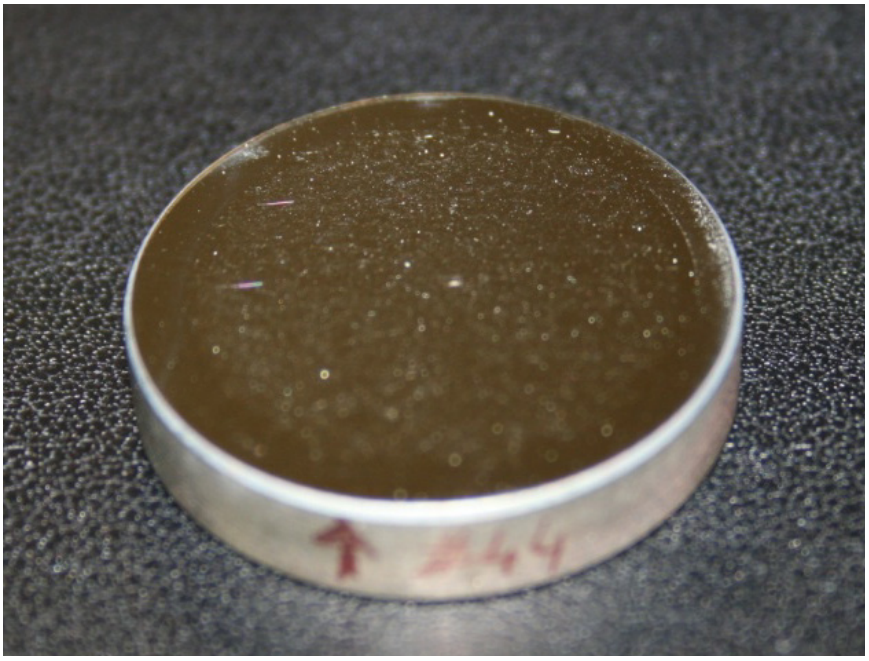

Figure 4.9 Test specimen number 44 after experiment.

4.3 Calculation of Number of Rain Drops

As mentioned previously, the exact number of liquid impact cannot be known through a rainfield. However, this can be calculated approximately with the formula below [7]:

$$impacts = {}^{10\,j\,V\,A\,t}\Big/_{6\,\pi d^3 v_t} \tag{4.1}$$

where, j is rain fall rate (cm/h), V is travelling velocity through the rain field (m/s), A is cross sectional area (cm^2 normal to the velocity vector), t is duration (s), v_t is terminal velocity which is expressed by:

$$v_t = 9.65 - 10.3e^{-0.6d} \tag{4.2}$$

where d is the diameter of raindrop in mm.

The mathematical expression for the terminal velocity of the rain drops comes from experimental studies and is confirmed by other authors also [45]. Figure 4.10 shows the measurement of the terminal velocity for rain drops in different diameters by Gunn & Kinzer 1949, Beard & Prupacher 1969, Gossard et al 1992, Best 1950 and Uplinger 1977. It is seen that for 2mm diameter rain drop reaches about 6.4 m/s in the air. If it is calculated by using the Equation 2.10 for 2 mm rain drop, the terminal velocity is; $v_t = 9.65 - 10.3e^{(-0.6)(2)} = 6.55\, m/s$. These two values are close to each other in an engineering accuracy.

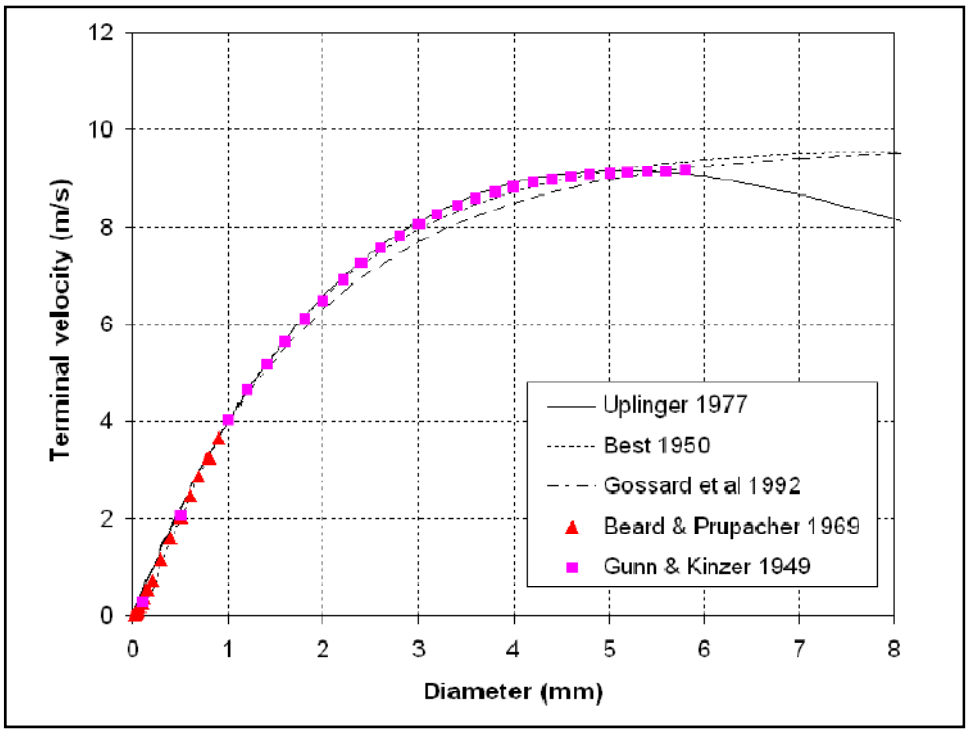

Figure 4.10 Terminal velocity measurements of fall for raindrops [45].

The terminal velocity measurements of the rain drops mentioned above have been studied experimentally under the natural conditions and this is true for the outer environment. However, the same situation is not true / realistic for the rain erosion test (whirling arm) since the rain is generated artificially from rain emitters above the

target as explained in Section 4.1. Since, the distance (between the position of the rain emitters that the droplet releases and the target) is also a parameter in this condition, the terminal velocity of the rain drop in whirling arm experiment should be determined in a different way.

Figure 4.11 shows the terminal velocity of the rain drop as a function of fall distance of rain drop up to 2 meters as well as the diameter [45]. The drops of 0.1 to 0.4 mm diameter reach their terminal velocity before 1 meter. However, drops of 0.7 mm diameter and larger need a fall path of more than 2.0 meters to reach their terminal velocities.

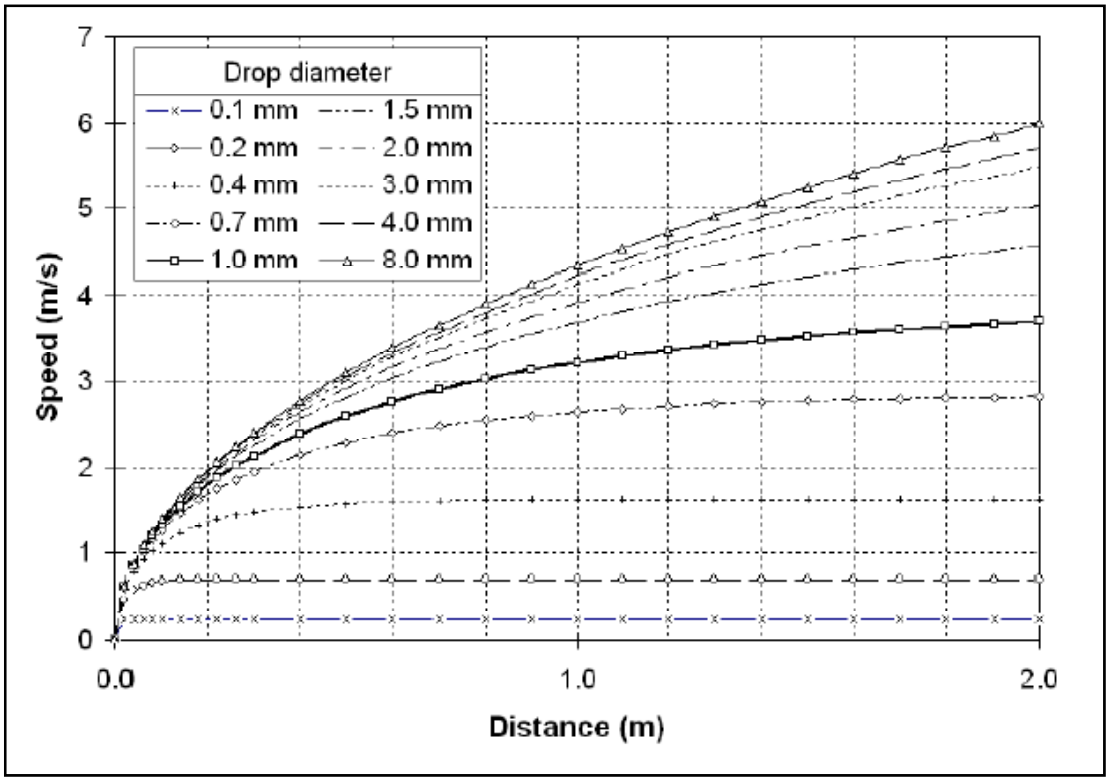

Figure 4.11 Velocity of raindrops as a function of fall distance [45].

In order to use this knowledge about the terminal velocity, the travel distance of the rain drops should be known. In Figure 4.3, the distance between the rain emitter and the target (germanium) can be seen. This value is approximately 0.15 m if the

diameter of the specimen (25.4mm) is scaled to the distance between the target and rain emitter. It seen from the Figure 4.11 that the fall speed of 2mm diameter rain drop is 1.75 m/s approximately for the fall distance of 0.15m.

In order to calculate the number of rain drops strikes to the target in whirling arm experiment, the vertical fall velocity of the drop (terminal velocity) before the impact is found as 1.75 m/s. An example of the calculation number of drops hitting to the target by considering the whirling arm experiment conditions for the 125 m/s impact speed is given in Appendix-A.

As it is calculated in Appendix-A, there are approximately 17438 drops hitting to the target in five minutes for the defined experimental conditions in the whirling arm experiment. However, a shock accelerometer can be used with this test setup to measure the exact number of water droplets. Moreover, if high speed cameras are used in two directions, the location of the impacted water droplets can be investigated.

CHAPTER 5

NUMERICAL AND WHIRLING ARM EXPERIMENT RESULTS

The first two chapters have presented the general view of the rain erosion problem as a result of high velocity liquid impact. Chapter 3 has gone through the details of the numerical simulation technique in LS-DYNA and the experimental setup regarding the rain erosion has been explained in Chapter 4. This chapter covers the outcomes of the numerical study and the whirling arm experiment results. Additionally, the damage threshold velocity for the germanium is reviewed with respect to numerical studies, whirling arm experiment and experimental studies discussed in Chapter 2.

5.1 Results of the Numerical Simulation

In this section, the results obtained in the numerical simulations are presented. The main aim of the numerical simulation is to find out the impact velocity at which the failure is realized. However, a question is aroused at this point that; what is the amount of damage that is sufficient for failure? Because of that, first of all, a criterion for the failure of the material is stated in this section. Secondly, the DTV estimation for the germanium is established by using a method in which several operations are performed. For this reason, the explanation of this method is also mentioned before the presentation of the numerical results.

5.1.1 Criterion of Failure in Rain Erosion

The JH-2 material model used for the germanium includes a damage parameter "D" changing between 0 and 1. As it has been mentioned previously, when the material is undamaged (intact) $D = 0$ and when the material is completely fractured $D = 1$. When post processing the results, the D is used for the fringe parameter during the impact and the change of this parameter can be seen in different colours on the germanium. The completely fractured regions are indicated by red, and intact regions are indicated by blue colour. The number of the elements marked by red colour shows the progress of the damage on the germanium. However, under which circumstances the material can be regarded as failed? Or in other words, how many elements are required to be red ($D = 1$) for the failure of germanium window?

Failure due to the rain erosion is defined in a publication [17] like that:

> *"…With SIJA it is clearly impractical to fire this many impacts, and it is therefore suggested that DTV data published from SIJA quote the values for the first appearance of any visible circumferential cracking at x200 magnification after 1, 3 and 10 impacts"* [17].

In the numerical simulations, the edge length of the element at the centre is 0.06 mm. This distance becomes 12 mm at x200 magnification level. Since 12 mm is sufficiently big enough to be diagnosed, even a small region that is failed on the germanium can readily be recognized at this magnification level. It is seen that, this is a very strict failure criteria for the rain erosion. Therefore, it is understood that, whenever a red (D=1) region is seen on the germanium, the material can be regarded as failed. On the other hand, the minimum red region comes up with the size of a single element only throughout the all impact cases for the numerical simulations. This situation can be seen in Figure 5.1. So, under these conditions it is possible to make such an assumption for the failure in the numerical simulation:

- *If there is any $D = 1$ (fully fractured) region diagnosed on the germanium, even in the size of a single element, the material is regarded as failed.*

The sufficient amount of damage to regard the material as failed is shown in Figure 5.1. Although the observed damage is relatively small in Figure 5.1, this could be interpreted as a failure of the window according to the assumption which is mentioned above. It is clearly seen that there is a red region which is labelled as $D = 1$ in the fringe between four elements and nearly in the size of single element. Since this region is fully fractured ($D = 1$), there is a crack can be expected here.

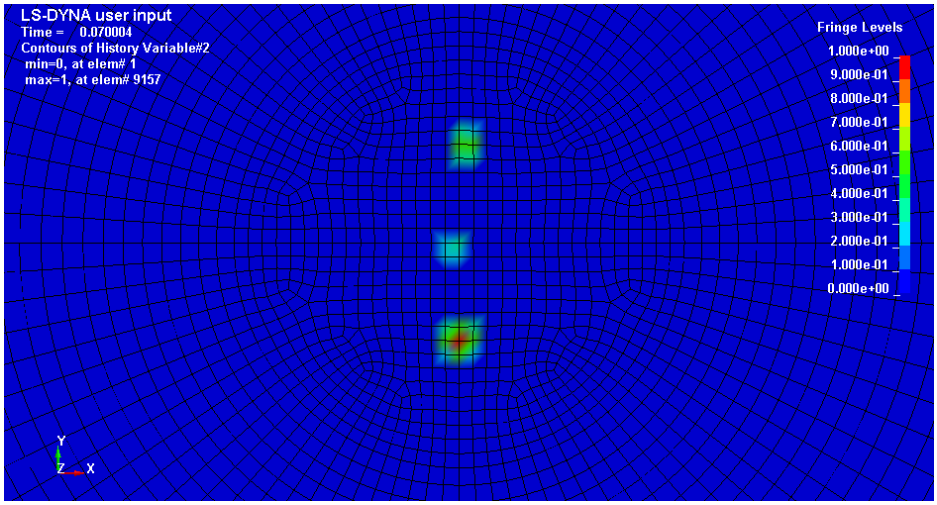

Figure 5.1 Amount of damage for failure (tenth impact of water drop at 150 m/s).

5.1.2 Numerical Estimation Method of DTV for Germanium

A series of simulations was performed in LS-DYNA in order to predict the DTV of germanium against rain erosion numerically within the scope of the thesis. The DTV is searched in a velocity range of 100 m/s - 250 m/s. The intermediate velocities are 120, 135, 150, 175, 200 and 225 m/s.

In the rain erosion problem, expectation of damage after a single impact may be true

for higher impact velocities, but it is not true for the lower velocities. Depending of the velocity, failure of the window may be observed at the first impact, may be second or sixth etc. The number of impacts is also related with the failure of the window material as well as the velocity. Because of that, two kinds of DTV stand for as explained in Section 2.3. One of them is single impact DTV and the other is multiple impacts DTV. The latter can be indicated that DTV(X impacts) where "X" shows the number of impacts. In the same way, single impact can also be presented as "DTV (Single impact)".

In order to simulate the multiple impact conditions numerically, restart module of the LS-DYNA is used for the present study. If the failure is not observed at the first impact, the germanium is conserved at the same stress level (at the same amount of damage), and the impacted water is replaced by the new one. The same velocity is attained to the new water and the second impact loading is applied to the target that preserves damage of the previous simulation. This process continues up to 10 impacts until the damage is observed as it can be seen Figure 5.1.

In order to predict the single and multiple impact DTV's for germanium against rain erosion, the number of impact versus damage threshold velocity curve is used. However, there are three steps required in order to draw this graph. These steps are as follows:

1. Counting of failed elements (D=1) in all simulations and making a table with these values.

2. By using the table in step 1, plotting "impact velocity versus number of failed element" graph with respect to number of impact.

3. By using the graph in step 2, plotting "number of impact versus damage threshold velocity" graph within the scope of failure criterion.

The first step is counting of the failed elements one by one. For example, in Figure 5.1, the damage is in the size of one element nearly, so it is understood that the failure is initiated and the number of failed element can be counted as 1 at this situation. This example is for impact of water drop for ten times at 150 m/s. Another example may be given from impact of water jet for two times at 200 m/s in Figure 5.2. In this case, it is seen that the all red regions correspond to nearly 48 elements in total. Therefore, the amount of damage can be measured in this way. After these measurements are completed for all the simulations, the data is collected in a table for the first step.

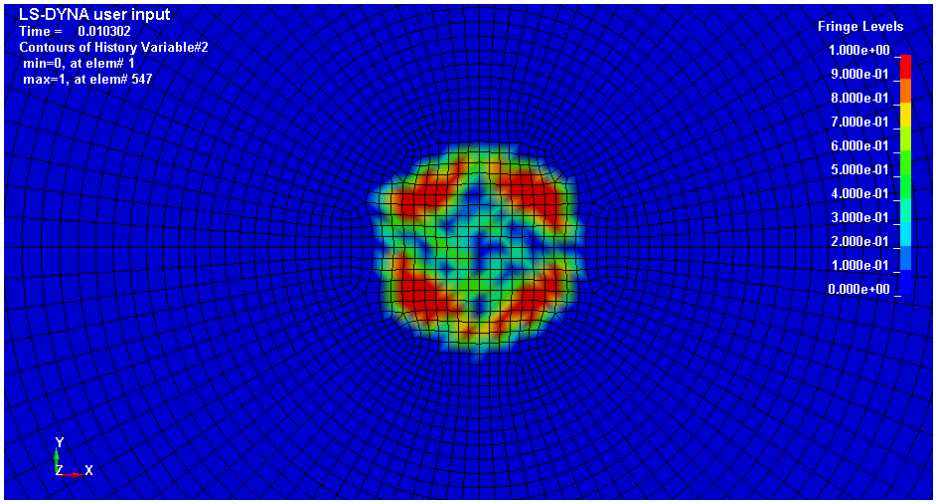

Figure 5.2 Damage for water jet impact for two times at 200 m/s.

The second step is plotting “impact velocity versus number of failed element” with respect to the measured failed elements in all simulations. In this graph the horizontal axis shows the impact velocity and the vertical axis shows the number of failed elements. The vertical axis is arranged in a logarithmic scale in base ten. The reason for the logarithmic scale is examining the failed elements between 1 and 10 in detail. The series of the graphs show the successive impact numbers.

For the third step, the “number of impact versus damage threshold velocity” graph is

derived by using the “impact velocity versus number of failed element” graph drawn in step 2. Initially, a horizontal line is drawn which passes through 1 on the vertical axis. The reason is that only one element is sufficient for the failure of the window according the failure criterion. Then, the intersection points between this line and the number of impact series are determined. By using those points “number of impact versus damage threshold velocity” curve is obtained. The interpretation of the DTV of the germanium against rain erosion becomes easy to understand by this graph. The DTV values for germanium between one impact and ten impacts, such as DTV (3 impacts) or DTV (7 impacts) etc., can be read in this graph.

5.1.3 Results of Water Drop Impact

In the light of the explanations mentioned in previous section, the failed elements are listed in Table 5.1 with respect to the impact velocity and the number of impact. In this table each filled cells represent an individual simulation. However, there are some empty cells also such as fourth impact at 225 m/s. For these situations, no simulations are needed to be performed since the damage has already reached beyond the required at previous impact.

Although “no damage” should be indicated as zero normally, it is indicated as 0.1 both in the Table 5.1 and Figure 5.3. The reason is the logarithmic vertical axis used in Figure 5.3. In this axis, zero and negative values cannot be plotted correctly. Only positive values can be interpreted on a logarithmic scale. Therefore, in order to show the lines (the number of impact series) between 1 and 0, the zero damage is indicated as 0.1 in the graph of this chart (Figure 5.3).

Table 5.1 The output of the numerical simulations for water drop.

	Impact Velocity (m/s)							
	100	120	135	150	175	200	225	250
	Number of Failed Elements							
1st impact	0.1	0.1	0.1	0.1	0.1	0.1	0.1	4
2nd impact	0.1	0.1	0.1	0.1	0.1	0.1	17	226
3rd impact	0.1	0.1	0.1	0.1	0.1	15	204	
4th impact	0.1	0.1	0.1	0.1	0.1	114		
5th impact	0.1	0.1	0.1	0.1	1	323		
6th impact	0.1	0.1	0.1	0.1	10			
7th impact	0.1	0.1	0.1	0.1	56			
8th impact	0.1	0.1	0.1	0.1	146			
9th impact	0.1	0.1	0.1	0.1	286			
10th impact	0.1	0.1	0.1	1	433			

The graphic version of Table 5.1 can be seen in Figure 5.3 and each impact number can be seen in different colours (step 2). For the first impact (which is at the right hand side), there is no failure up to 225 m/s and four elements are failed at 250 m/s. Similarly, for the second impact, there is no failure up to 200 m/s, 17 elements are failed at 225 m/s and 226 elements are failed at 250 m/s. The other curves can also be interpreted by this way.

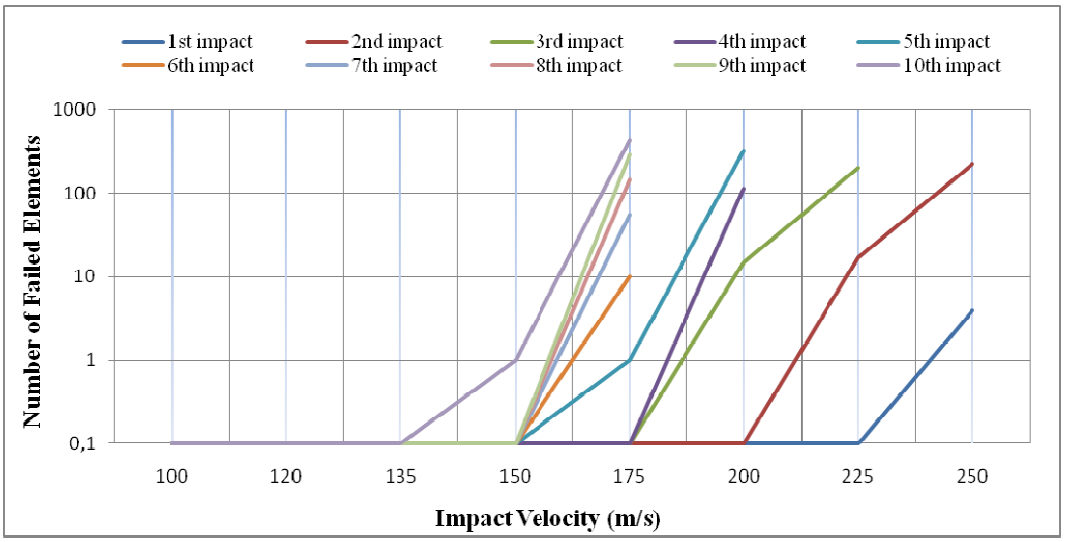

Figure 5.3 Number of failed elements with respect to impact-number and velocity of water drop.

As it is explained in step 3 in previous section, “the DTV versus number of impacts curve” can be constructed by using Figure 5.3. The obtained new graph is seen in Figure 5.4. It is seen that, the DTV decreases as the number of impacts increases. Each successive impact on the same position decreases the strength of the material as expected. Therefore, the DTV is high for the first few impacts and low for the further impacts.

According to Figure 5.4, the germanium can withstand water drop impact up to 250 m/s for the first impact. However, the DTV reduces to 211 m/s for the second and 187 for the third impact due to accumulated damage from previous impacts. This rate of fall continues as long as the number of impacts increases and after the sixth impact, the DTV curve starts slowing down. The influence of number of impacts on the DTV decreases as long as the impact number increases. Finally, the DTV of germanium reduces 150 m/s after the tenth impact.

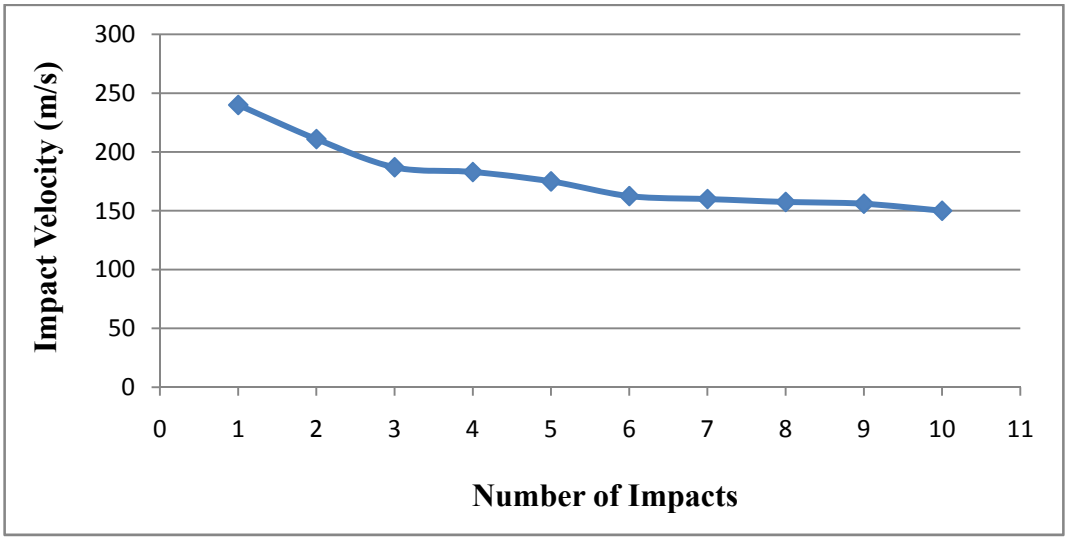

Figure 5.4 DTV curve for germanium with respect to water drop.

5.1.4 Results of Water Jet Impact

The results of the water jet impact on germanium window are presented in this section in a similar way. The number of failed elements is listed in Table 5.2 with respect to impact velocity and the number of impact. The graphical representation of these three parameters (impact velocity, number of impact and number of failed elements) is shown in Figure 5.5. Finally, transformation to the DTV curve for one failed element is presented in Figure 5.6.

Table 5.2 The output of the numerical simulations for water jet.

	Impact Velocity (m/s)							
	100	120	135	150	175	200	225	250
	Number of Failed Elements							
1st impact	0.1	0.1	0.1	0.1	0.1	0.1	1	41
2nd impact	0.1	0.1	0.1	0.1	0.1	48	200	
3rd impact	0.1	0.1	0.1	0.1	32	265		
4th impact	0.1	0.1	0.1	3	161			
5th impact	0.1	0.1	0.1	19	363			
6th impact	0.1	0.1	2	75				
7th impact	0.1	0.1	8	197				
8th impact	0.1	0.1	42					
9th impact	0.1	3	115					
10th impact	0.1	4	220					

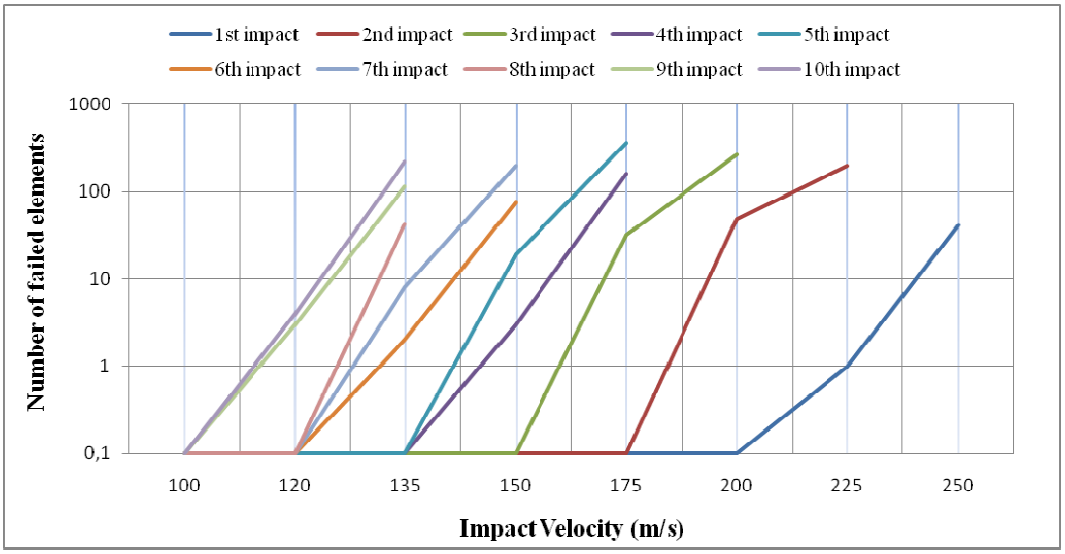

Figure 5.5 Number of failed elements with respect to impact-number and velocity of water jet.

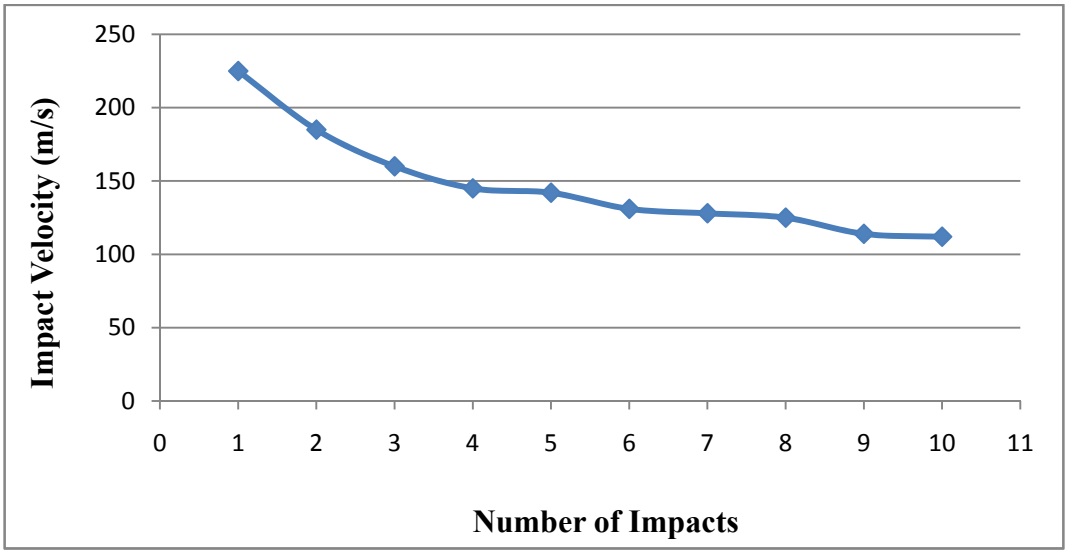

Figure 5.6 DTV curve for germanium with respect to water jet.

According to Figure 5.6 the germanium can withstand water jet impact up to 225 m/s. Under that velocity, no damage occurred for one impact. However, the DTV reduces to 185 m/ for the second and 160 for the third impact due to accumulated damage of previous impacts. This rate of fall continues as long as the number of impacts increases and after the fourth impact, the DTV curve starts slowing down gradually. The influence of number of impacts on the DTV decreases as the number of impact increases. Finally, the DTV of germanium reduces 112 m/s after the tenth impact for the water jet impact.

5.2 Whirling Arm Test Results

In this section, the results of whirling arm experiments are presented for three different velocities which are 125, 150 and 200 m/s. Details of the whirling arm test technique are given in Section 2.4.1 and the test facility is described in Section 4.1. Additionally, the test conditions for the whirling arm experiment are explained in Section 4.2.

5.2.1 Whirling Arm Results at 125 m/s

The first sample is exposed to impacts of water drops at 125 m/s for 5 minutes. Since, in whirling arm experiment, there is no exact data was provided regarding the number of water droplets hitting to the target, the approximation technique which is explained in Section 4.3 is used here. The specimen travels at 125 m/s through a 2.5 cm/h rain fall for 5 minutes. It is calculated that there are 17438 drops hitting to specimen which is 25.4 mm in diameter (see the example in Appendix-A). Since the conditions in that example is the same as the experimental conditions for 125 m/s impact speed, the result (17438 impacts) can be used here directly.

The approximation of how many drops hit to the same place on the window can be estimated roughly by proportion of window area ($\pi 25^2/4$) to the cross sectional area of the rain drop ($\pi 2^2/4$). Since the geometries are the same, this proportion is just the square of the diametric proportion which is $(25/2)^2 \cong 156$. So that, the number of drops hit to the same place over the window becomes approximately $17438/156 = 112$ drops at the 125 m/s impact velocity. This approach is surely just an approximation and shouldn't be interpreted as the exact value. This calculation only gives a reference value in order to make sense the number of the drops hitting to the same point.

The microscope view of the first specimen after the test is seen in Figure 5.7. Among the total 17438 striking to germanium, only 112 of them hit to the same position approximately. It is seen that there is no visible crack observed on the germanium window after the impact of water droplets more than one hundred times at the same point. Although there are some asperities seen on the surface of germanium, those are not caused from the collision of the raindrops. They are the production induced damages and cannot be regarded as the rain erosion. However, it should be noted that there is a very small hill which is taken in a circle in Figure 5.7. This hill is different from the surface asperities aroused from the production and can be regarded as the very beginning or the signature of the initiation of the damage. The surface at this

location is swelled a little bit but it is seen that there is no crack observed. Therefore, it can be said that the ADTV of the germanium window is very close to 125 m/s. Since this damage is just a small hill and needs a further load in order to turn into a crack, the ADTV of germanium is said to be higher than 125 m/s.

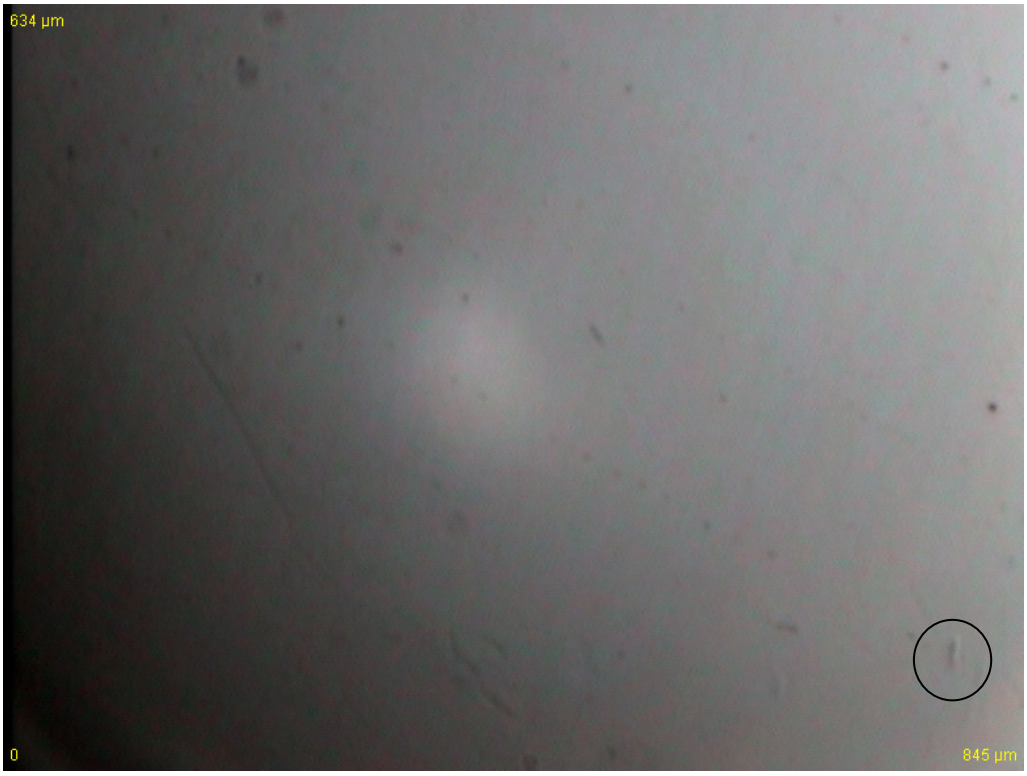

Figure 5.7 Whirling arm test result at 125 m/s impact velocity in 5 minutes through 2.5 cm/h fall rate for 2 mm diameter water drop.

5.2.2 Whirling Arm Results at 150 m/s

The second test condition in the whirling arm is the impact of water drops to the germanium sample at 150 m/s for 5 minutes through the 2.5 cm/h fall rate. If the impact velocity increases at the same rain fall rate in the whirling arm experiment, the number of water drops hitting to the target also increases expectedly. Since only the velocity is changed with the previous test condition and the calculations are linear, the number of rain drops impact to target can be obtained directly by using the

existing value that is found for 125 m/s previously. If there are 17438 drops hitting to germanium at 125 m/s, by a linear relationship, there should be 20925 drops hit to the sample at 150 m/s. Moreover, by using the same areal ratio, the number of raindrops hitting to the same place becomes approximately 20925/156 = 134 drops at 150 m/s.

In 5 minutes, there are approximately 134 drops hitting to the same place on germanium at 150 m/s in the second test condition. The damage can be clearly seen in Figure 5.8 and Figure 5.9 which are the views on the surface of germanium. In some locations on germanium, the damage can be interpreted as the circumferential cracking which is seen in Figure 5.8. There are two partially (may be quarter of a circle) circular damage seen in upper left and lower right corner of the view.

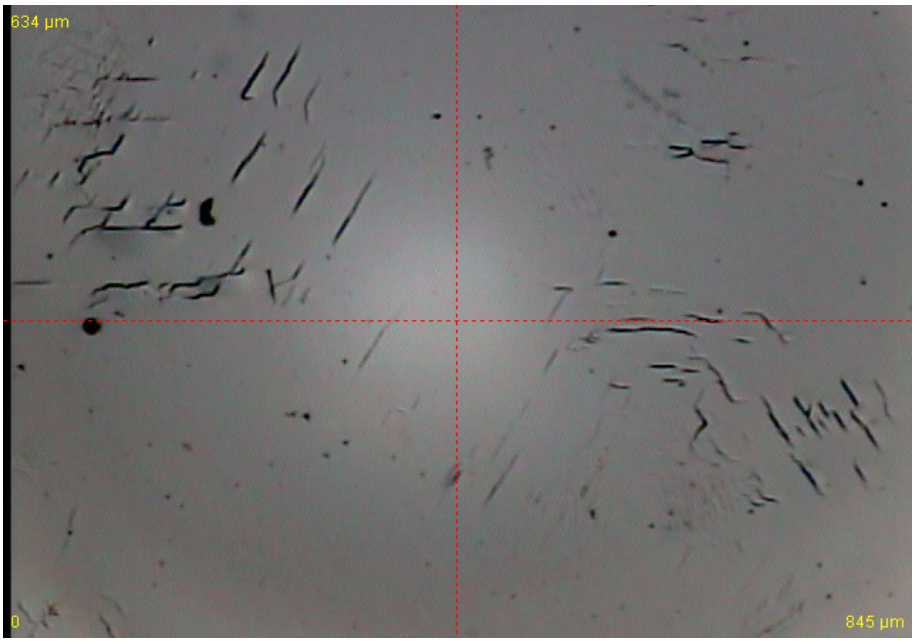

Figure 5.8 Whirling arm test result at 150 m/s impact velocity in 5 minutes through 2.5 cm/h fall rate for 2 mm diameter water drop (1).

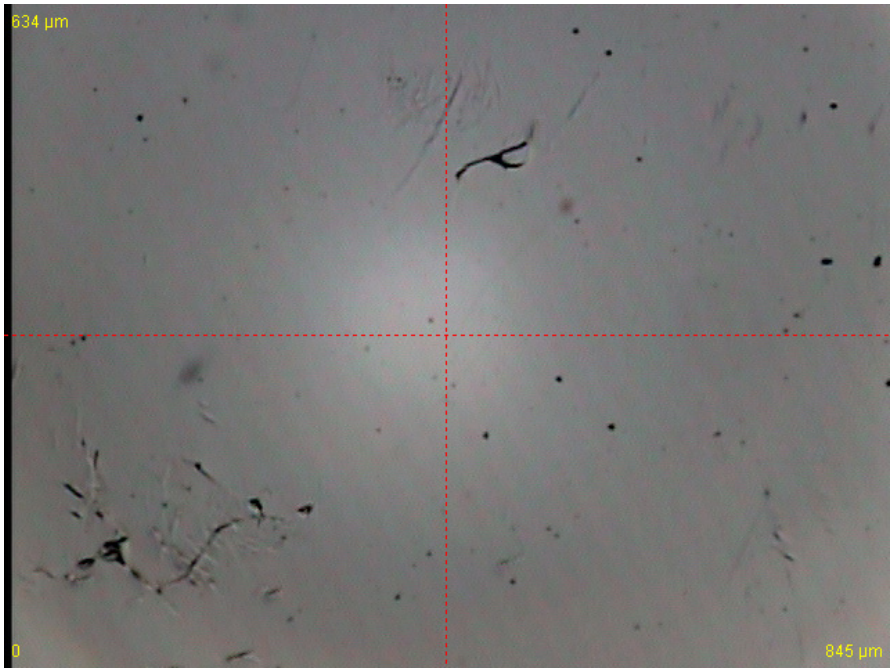

Figure 5.9 Whirling arm test result at 150 m/s impact velocity in 5 minutes through 2.5 cm/h fall rate for 2 mm diameter water drop (2).

5.2.3 Whirling Arm Results at 200 m/s

The last test condition is different from the other two cases. In the first two tests (125 m/s and 150 m/s); the duration was the same and 5 minutes for both velocities. However, this time, the germanium specimen exposed to rain erosion for 25 minutes continuously and the impact velocity is changed five times throughout the test. The specimen waits 5 minutes for each velocity and after this time is up, the velocity is increased to an upper level. The starting velocity is 50 m/s, the second is 70 m/s, the third is 90 m/s, the fourth is 150 m/s, and the last is 200 m/s. The number of water drops hitting to the same position on germanium is calculated in a similar way. In this test condition, there are approximately 45 drops hitting to same place at 50 m/s on germanium and there are 63, 81, 134 and 179 drops hitting to the same place for 70, 90, 150 and 200 m /s impact velocities respectively.

After the test, which is the worst condition between the all three test conditions, the damage patterns can be seen in Figure 5.10 and Figure 5.11. Although the dimension of the view shows a little portion of the specimen on the surface, everywhere has full of similar damage patterns. Since no damage is diagnosed for the 125 m/s in the first test condition, it is hard to expect any damage for the lower velocities such as 50 m/s, 70 m/s and 90 m/s on germanium for the current test condition. It can be said that most of the damage occurred at the end of 150 m/s and 200 m/s impact velocities. However, circumferential damage patterns, which exist in 150 m/s, cannot be seen in this test condition. This situation can be explained by the propagation of the damage during 200 m/s impact velocity. Those circumferential damage patterns occurred at 150 m/s are enhanced/propagated by the impacts of water drops at 200 m/s and boundaries are disappeared due to the severity of the test condition.

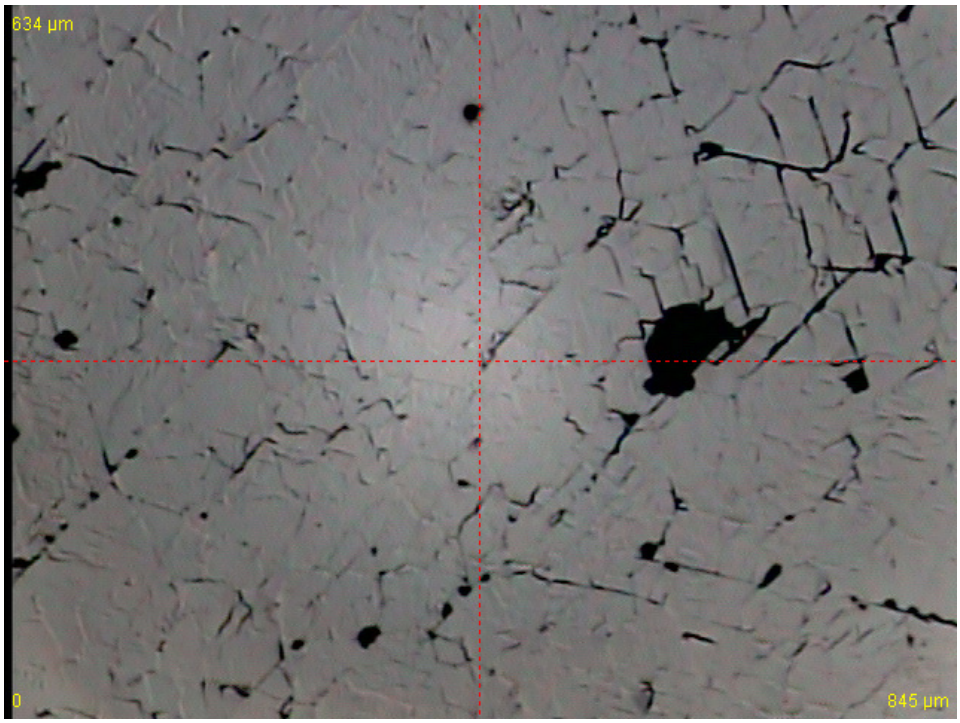

Figure 5.10 Whirling arm test result after the impact of water drops at 50, 70, 90, 150 and 200 m/s for 5 minutes at each velocity (25 minutes total test duration) respectively through 2.5 cm/h fall rate (1).

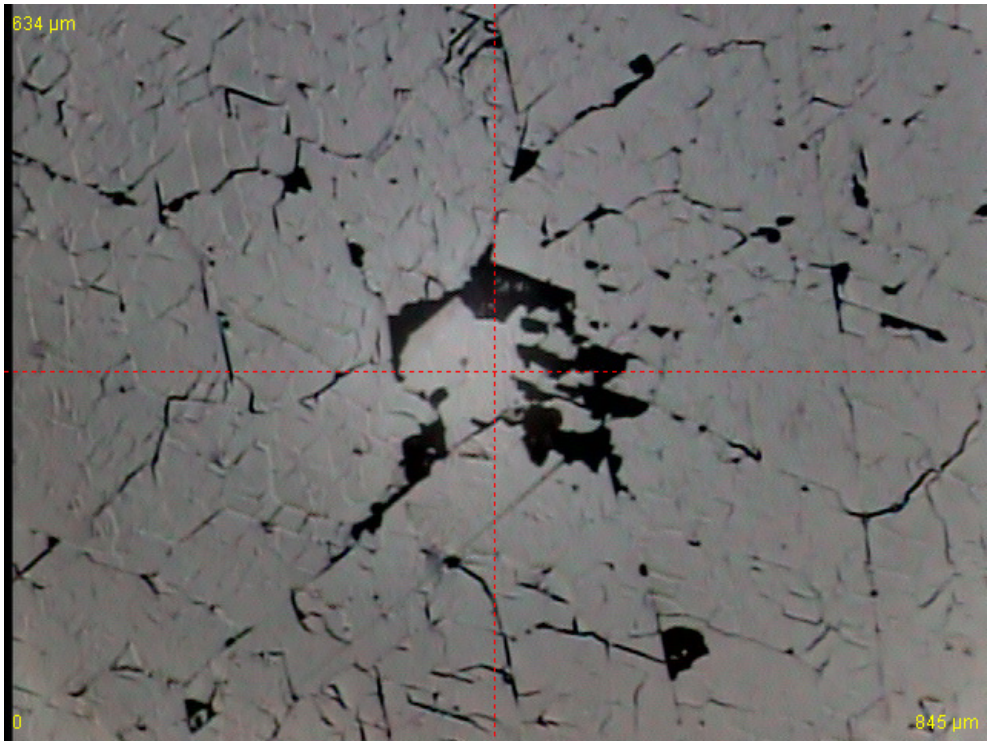

Figure 5.11 Whirling arm test result after the impact of water drops at 50, 70, 90, 150 and 200 m/s for 5 minutes at each velocity (25 minutes total test duration) respectively through 2.5 cm/h fall rate (2).

5.3 Review of DTV for Germanium

The main aim of the rain erosion studies in the literature is to find out the DTV values for the different window materials. If the durability of a specific material against the rain erosion is known, probable hazards in the harsh environmental conditions can be prevented in advance. Because of that, knowing the rain erosion resistance of the infrared windows that are used in high velocity applications is very important.

Discussions in this section are only about the germanium window. There are three set of results coming from different sources about the rain erosion resistance of germanium. The first source is the numerical simulation which is the main objective

of the present study. In this context the Figure 5.4 and Figure 5.6 (which are the output of the numerical simulation) are evaluated. The second source is the experimental study which has been held on the whirling arm test facility in Sweden. And the last source is the previously made experimental studies found in literature and discussed in Section 2.5.1. In this context, MIJA experiment results (Figure 2.14, Figure 2.15 and Figure 2.16) are evaluated.

5.3.1 DTV of Germanium Obtained by Numerical Simulation

In the numerical simulations, there are two different geometries used to make comparison with different sources. The first geometry is sphere which is modeled to make a comparison with the whirling arm experiment and the second geometry is the water jet which is modeled to make a comparison with the MIJA experiment in the literature. Therefore, both of the geometries are designed for the different experiment conditions.

Obtained threshold curves for both water shapes (Figure 5.4 and Figure 5.6) are plotted in one singe graph as it can be seen in Figure 5.12. It is clear that, the trend of slope is more or less similar in both curves. In other words, the change in the DTV decreases as the number of impacts increases in both curves with a similar rate and most of the change occurs between 1^{st} and 4^{th} impacts. However, the water jet curve is following the spherical water curve with an offset. Mainly, the threshold velocity for water jet is less than the spherical water at each impact. Therefore, it can be interpreted that the damage caused by the water jet is more than that is caused by the water drop. The reason of this difference can be explained by the pressure distribution curves on germanium for two water shapes. As seen in Figure 5.13 the pressure distribution at the center of germanium different for water drop and water jet. Although the peak pressure values are nearly the same for both shapes, the duration at the peak is longer for water jet than that is for the water drop. Therefore, it can be said that the damage effect of the water jet is more than the water drop. Incidentally, although both pressure curves start to reach at the peak value at the

same time actually, the water drop curve is translated to a little bit right on the time axis intentionally in order to show the both curves in a single figure.

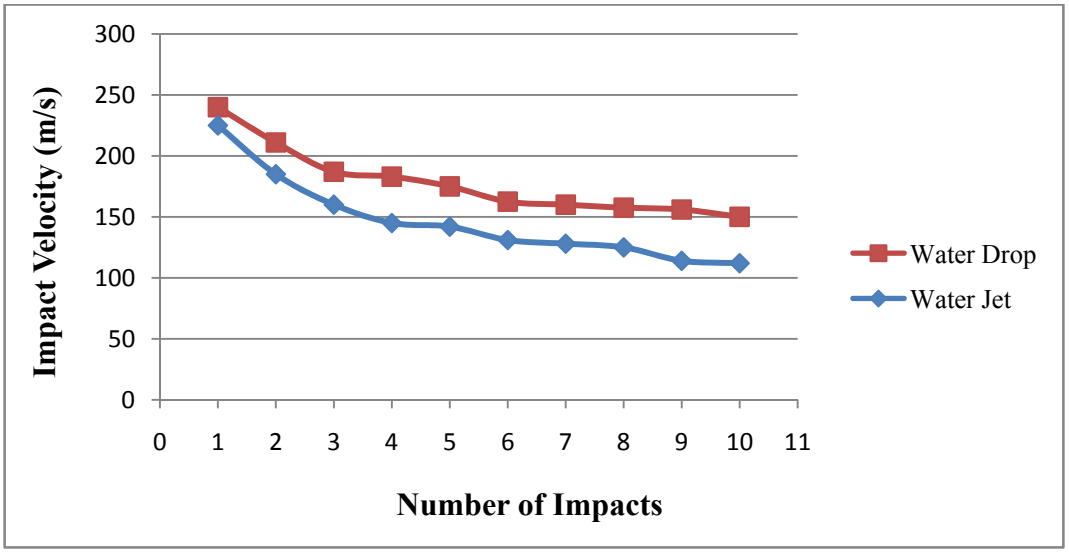

Figure 5.12 Comparison of Water Drop and Water Jet.

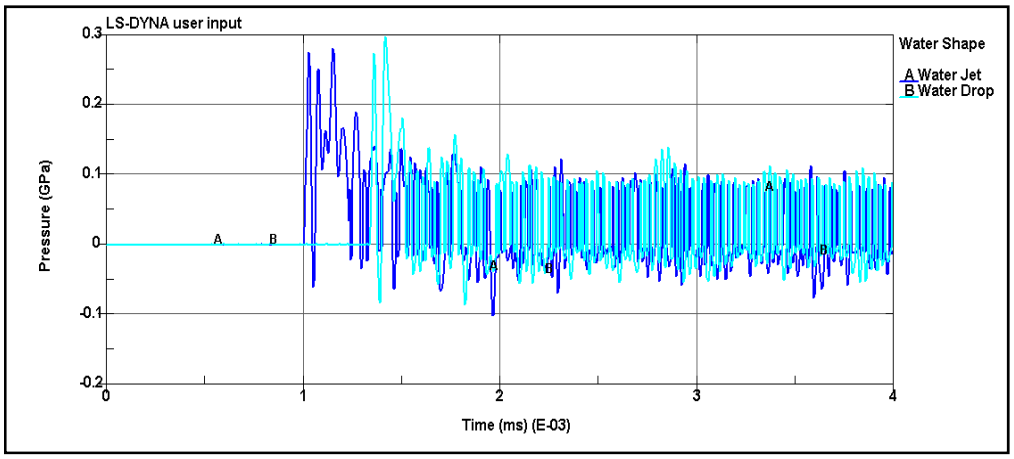

Figure 5.13 Pressure distributions on germanium for water drop and water jet at 150 m/s impact velocity.

There is another remarkable point that should be mentioned in the Figure 5.13. The water hammer pressure is given in the first chapter by Equation 1.1 which is

$P_c = \rho C v$ and occurs at the first stages of the liquid impact. According to the formula, water hammer pressure is calculated as 270 MPa at 150 m/s. It is seen that, the pressure occurred at the center of germanium is consistent with the literature and can reach up to calculated water hammer pressure. This pressure prevails for very short durations (fractions of a microsecond) for both water drop and water jet.

5.3.2 DTV of Germanium Obtained by Whirling Arm Experiment

In the whirling arm experiment, it is impossible to measure the single impact resistance of germanium due to the nature of the test conditions. Therefore, the whirling arm experiments provide the multiple impact damage resistance of the materials.

In the first test condition, it is seen that there is not any crack observed at 125 m/s (Figure 5.7) for total of 17438 drops hitting to germanium sample in 5 minutes. According to a rough estimation (area ratio of water drop and the germanium sample), there are more or less 112 drops hitting to germanium nearly the same place. Therefore it can be said that, germanium can withstand against the rain erosion at 125 m/s or below velocities for 2 mm diameter rain drops.

The second test condition is performed at 150 m/s impact velocity. The rain erosion damage can clearly be seen at views of 0.845 mm x 0.634 mm in Figure 5.8 and Figure 5.9. This kind of damages can be readily regarded as a failure of the germanium window.

In the third test condition, a different experiment design is utilized relative to previous two considerations. Instead of a constant velocity and duration as it has been in other two ones, there are different velocities; starting from 50 m/s and reaches up to 200 m/s. Since there are velocities above from 150 m/s, the damage is enhanced and can be seen in Figure 5.10 and Figure 5.11.

The experiments revealed that the rain erosion damage starts between 125 m/s and 150 m/s. Since there is no obvious crack observed at 125 m/s, the ADTV of germanium should be higher than 125 m/s. On the other hand, the cracks at 150 m/s are too much with respect to the amount of damage which is sufficient for the initiation of the failure according to criterion mentioned in Section 5.1.1. Therefore, it can be interpreted that, the initiation of the damage is below 150 m/s for germanium.

5.3.3 DTV of the Germanium given in Literature

The single impact resistance of the germanium is changing between 225 m/s and 250 m/s according to the Figure 2.14, Figure 2.15 and Figure 2.16. On the other hand, the ADTV values changing between 122 m/s and 155 m/s. Moreover, since these experiments are performed by MIJA, the intermediate values such as DTV (second impact) or DTV (fifth impact) can also be read in those figures. It is seen that the threshold velocity reduces progressively while the number of impact increases. Moreover the trends of the slopes largely change between 1 and 10 impacts and after that the curves start to smooth out.

CHAPTER 6

DISCUSSION, CONCLUSION and FUTURE WORK

6.1 Discussion

In SIJA and MIJA test techniques the target (such as germanium) is stationary and the water has a high impact velocity. Because of that the water resembles to a water jet due to the high pushing forces applied on it. On the other hand, in the whirling arm test technique, the water drop (released from rain emitters) makes only free fall motion and reaches up to only 1.75 m/s (Section 4.3) while the target hits water drops with high velocities. Since the water drop does not exposed to a large shape change (like it has been in the SIJA), it is assumed as spherical (water drop) in the whirling arm test technique. Therefore, it is more convenient to compare water jet simulations with respect to MIJA results and the water drop simulations with respect to whirling arm experiments.

6.1.1 Comparison of Numerical Results (Water Drop) with Whirling Arm Experiment

The numerical simulations for water drop show that the DTV (ten impacts) of germanium is 150 m/s. On the other hand, the ADTV of germanium is between 125 m/s and 150 m/s in the whirling arm experiments as explained in Section 5.2. So, it is clear that, numerical simulation overestimates the experimental study within the scope of the multiple impacts.

According to the definition mentioned in Section 5.1.1 regarding the failure criterion of the optical lens material, the damage obtained at 150 m/s is beyond the initiation of the failure. Therefore, the damage is said to be developed/enhanced at 150 m/s in the whirling arm experiment. On the other hand, there is not any cracking observed at 125 m/s. Therefore, in order to make a true comparison between the results, the exact velocity at which the damage is just initiated should be known for the whirling arm experiment. However, there is no such an intermediate data between 125 m/s and 150 m/s. Because of that, there is a need for an estimation between these values for the determination of the initiation of the failure in the whirling arm experiment. Since the ADTV is above from 125 m/s and below from 150 m/s, it is thought to be convenient to take the mean of these two values in order to assume the initiation of the failure very roughly in the whirling arm experiment. Therefore, if the ADTV is assumed as 138 m/s for the whirling arm experiment, the amount of error in the numerical simulation is approximately %9 for the numerical simulation within the scope of multiple impact threshold comparison. However, the single impact threshold comparison between the water drop simulations and the whirling arm experiment cannot be made due to the nature of the test technique.

6.1.2 Comparison of Numerical Results (Water Jet) with MIJA Experiments

Water jet simulations are performed for the comparison of the numerical results with the MIJA results found in the literature. This test technique allows investigation of both the single and multiple impact cases. Therefore both DTV (single impact) and ADTV values can be obtained together in this experiment. In order to see the effect of each impact to the DTV, generally “number of impact versus DTV” curves are used in the MIJA experiment (like in Figure 2.14, Figure 2.15 and Figure 2.16). To make a comparison, same kind of graph is drawn for the numerical simulations as shown in Figure 5.4 and Figure 5.6. Since 10 successive impacts are used in the numerical simulations, the comparison can be made up to ten impacts by using these graphs. In order to see all the results together, Table 6.1 is prepared for the first, third, fifth, tenth, one hundredth, two hundredth (and more) impacts by using the

numerical simulation results and the MIJA results.

Table 6.1 DTV comparison between the numerical simulation results for water jet and experimental results found in the literature.

	1st Impact	3rd Impact	5th Impact	10th Impact	100th Impact	200+ Impact
FEM (water jet)	225	160	142	112	-	-
Figure 2.14	225	190	175	160	155	155
Amount of error	0.0%	15.8%	18.9%	30%	-	-
Figure 2.15	250	192	170	162	136	122
Amount of error	10%	16.7%	16.5%	30.9%	-	-
Figure 2.16	250	200	170	155	135	130
Amount of error	10%	20%	16.5%	27.7%	-	-

It is seen that, the first impact results obtained in the numerical simulation underestimates the MIJA results with 10% in Figure 2.15 and Figure 2.16. There is no error with respect to the Figure 2.14 for the first impact. However, it is clear that the amount of error is growing up as the number of impact increases. The maximum error is 30.9% which occurs at the tenth impact with respect to Figure 2.15.

6.1.3 Shape of Damage in Rain Erosion

A special damage shape occurs in water drop impact problems generally. Damage patterns on the target material which is brittle generally take a circular like shape with an undamaged central zone after the impact(s). This form of the cracks in the rain erosion is also observed by other referenced studies such as [6], [18] and [19]. The reason of this type failure, according to the mentioned studies, is the Rayleigh surface waves that are emanating from the impact region. Since the brittle materials can withstand high compressive loadings which occur at the centre of the impact, material does not fail due to compressive loading at the initial stages of the impact. It fails due to the Rayleigh surface waves generated by the impact which causes tensile loading on the material surface. There are two partially circler regions can be seen in Figure 6.1 (a). One of them is in the upper left corner and the other is the lower right corner of the view. This type of damage can also be seen in the numerical simulation. It is seen in Figure 6.1 (b) that the shape of the damage in the numerical simulation is almost circler.

The time step is automatically calculated in order to investigate the shock waves throughout an explicit simulation. The size of the time step depends on the minimum edge length on the elements. At each time step, the minimum edge length is searched and if a change is detected (such as deformation of the element), the time step value is updated according to the new length.

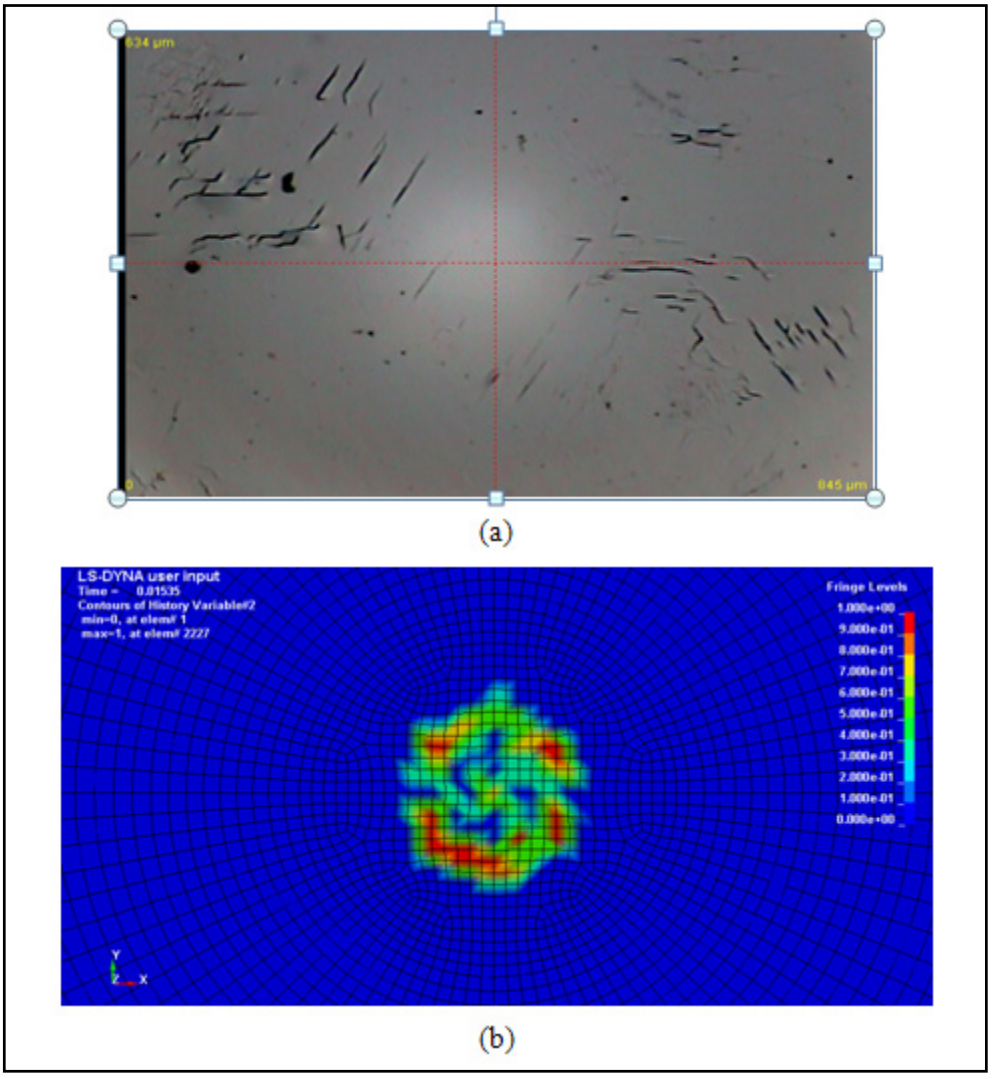

Figure 6.1 Damage observed in the (a) whirling arm experiment at 150 m/s (b) 3th impact at 200 m/s in numerical simulation.

6.2 Conclusion

In this study, the DTV of germanium, an optical window, is estimated by means of the finite element method. Both single and multiple impact conditions are considered within the scope of the current thesis. Additionally, two different water shapes (water drop and water jet) are used for the numerical simulations in order to make a comparison with different type of experimental studies. The DTV (ten impacts) is

estimated as 150 m/s by the numerical simulation for water drop and it is found as 138 m/s in the whirling arm experiment. It is seen that the numerical simulation results for the spherical water drop over estimates the whirling arm experiment by 9%. However, this comparison is not made at the same number of impacts condition. There are roughly 156 impacts calculated (see the Section 5.2.1) on the same place at 125 m/s in whirling arm experiment, whereas there are just 10 successive impacts considered in the numerical simulation. Although the DTV curve is almost smoothed out after ten impacts in Figure 5.4, the slope still shows a falling tendency in the DTV with the increase of the number of impacts. Therefore, if the comparison can be made over 100 impacts, it is thought that the amount of error in numerical simulation may be reduced some more.

Since a special test setup is required, the rain erosion experiment may not be found easily everywhere. However, if the material model constants are known, one can use FEM in order to estimate the rain erosion resistance for that interested optical material.

6.3 Future Work

The numerical simulations for the water jet are compared to MIJA experiment results which are found in the literature for germanium. Since the individual impact results can be captured in this test technique, the comparison can be made with respect to number of impacts. To make a comparison, the 1^{st}, 3^{rd}, 5^{th} and 10^{th} impacts conditions are considered for both numerical simulation and MIJA experiment results. It is seen that, the first impact results are close to each other. However, as the number of impact increases the amount of the error increases also and the maximum error is %30.9 in the numerical simulation after the 10^{th} impact. What causes this error at higher number of impacts is not known exactly, but it is clear that water jet diameter expands in MIJA as it can be seen in Figure 2.10. Moreover, the length of the water cannot be known exactly in the experiment. Since a logical explanation cannot be made with this information currently, the investigation of this error is left

as future work.

The rain erosion resistance of germanium is changing between 122 m/s and 155 m/s for multiple impact conditions as it can be seen in both experimental and numerical simulation studies. However, as mentioned before, the use of special protective coatings can enhance the DTV of germanium against the rain erosion. 1μm carbon coated germanium samples can withstand higher impact velocities, such as 220 m/s, as it is mentioned in Section 2.5.1. On the other hand, another important consideration about the coating is the optical performance as mentioned by Goldman and Tustison [46]. Protective coatings should be transparent through the spectral region of the optical material in order not to degrade the performance of the lens. The transparence of the coating depends on the compositon of the coating and the thickness.

The effect of a coating depends on thickness (in the order of microns), bonding (in the order of nanometers), internal stress and the mechanical properties of the coating and the substrate. Moreover, while the production of the coatings on the substrate material, some process parameters such as temperature and/or material composition can also change the effect of the coatings. However, modeling of the coating in explicit finite element software is complex. The numerical simulation of the coated optical windows is left as the future work for the current thesis.

Lastly, the shape of the water drop is assumed as spherical throughout the current study. However, although the water drop resembles to a spherical shape, the exact geometry is not a pure sphere. The actual shape of the water drop can be modelled as a future work and the differences between the spherical geometry can be investigated.

REFERENCES

[1] Osborne N., Graves G., Alexander K., Simerlink D. and Haren R., "LANTIRN Infrared Window Failure Analysis" Proc. SPIE Vol. 2286, pages; 444-455, 1994.

[2] Defence Standard, "Environmental Handbook for Defence Material", Ministry of Defence, 00-35 (PART 4) / Issue 3, Chapter 6-02, page; 203, May 1999.

[3] Coad E.J., Pickles C.S.J., Seward C.R., Jilbert G.H., and Field J.E., "The Erosion Resistance of Infrared Transparent Materials", Proc. R. Soc. London, pages; 213-238, 1998.

[4] Cook Stanley S., "Erosion by Water-Hammer", Proceedings of the Royal Society of London, Vol. 119, No. 783, pages; 481-488, July 1928.

[5] Huang Y. C., Hammitt F. G., and Mitchell T.M., "Note on Shock-Wave Velocity in High Speed Liquid-Solid Impact", Journal of Applied Physics, Vol. 44, No 4, April 1973.

[6] Kennedy C. F., Field J.E., "Damage Threshold Velocities for Liquid Impact", Journal of Material Science, Vol. 35, pages; 5331-5339, February 2000.

[7] Harris Danniel C., "Infrared Windows and Dome Materials", SPEI Publications, ISBN 0-8194-0998-7, 1992.

[8] Heymann F. J., "High Speed Impact Between a Liquid Drop and a Solid Surface", Journal of Applied Physics, 40, pages; 5113-5122, 1969.

[9] Field J. E., M. Lesser B., Dear J. P., "Studies of Two-Dimensional Liquid-Wedge Impact and Their Relevance to Liquid-Drop Impact Problems", Proceedings of the Royal Society of London, Series A, Mathematical and Physical Sciences, Vol. 401, No. 1821. , pages; 225-249, October 1985.

[10] Haller K.K., Ventikos Y., Poulikakos D., "Computational Study of High-

Speed Liquid Droplet Impact", Journal of Applied Physics, Volume 92, Number 5, September 2002.

[11] Li N., Zhou Q., Chen X., Xu T., Hui S., Zhang D., "Liquid drop impact on solid surface with application to water drop erosion on turbine blades, Part I: Nonlinear wave model and solution of one-dimensional impact", International Journal of Mechanical Sciences, Volume 50, pages; 1526–1542, August 2008.

[12] Zhou Q., Li N., Chen X., Xu T., Hui S., Zhang D., "Liquid drop impact on solid surface with application to water drop erosion on turbine blades, Part II: Axisymmetric solution and erosion analysis", International Journal of Mechanical Sciences, Volume 50, pages; 1543–58, August 2008.

[13] Adler W. F. and Mihora D. J., "Analysis of Waterdrop Impacts on Layered Window Constructions", SPIE Proceedings Vol. 2286, pages; 264-274, September 1994.

[14] Chang Y., "Hydrocode Analysis at APL", Johns Hopkins Apl Technical Digest, Volume 19, Number 1, 1998.

[15] Tutt B. A., Taylor A. P., "The Use of LS-DYNA to Simulate the Water Landing Characteristics of Space Vehicles", 8th International LS-DYNA Users Conference, May 2004.

[16] Kiocek P., Mckenna T., and Trombetta J., "Thermo-Optic, Thermo-Mechanical, and Electromagnetic Effects in IR Windows and Domes, and the Rationale for GaAs, GaP, and Diamond", SPIE Proceedings Vol. 2286, pages; 70-90, September 1994.

[17] Seward C.R., Pickles C.S.J., Coad E.J., Watt M. and Field J.E., "Studies of Rain Erosion Mechanisms in a Range of IR Transmitting Ceramics · Including Coated Samples", SPC-92-4032, January 1994.

[18] Bowden F. P., and J. H. Brunton, "The Deformation of Solids by Liquid Impact at Supersonic Speeds", Proceedings of the Royal Society of London, Series A, Mathematical and Physical Sciences, Vol. 263, No. 1315, pages; 433-450, October 1961.

[19] Zwaag S. V. D. and Field J.E., "Indentation and Liquid Impact Studies on Coated Germanium ", Philosophical Magazine A, Vol. 48, No. 5, pages; 767-777, April 1983.

[20] Seward C. R., Coad E. J., Pickles C. S. J. and Field J. E., "The Rain Erosion Resistance of Diamond and Other Window Materials", SPIE Proceedings Vol. 2286 / 285, September 1994.

[21] Hörmann M., "Introduction to LS-DYNA", Training Class, CADFEM, March 2008.

[22] Belytschko T., "Finite Elements for Nonlinear Continua and Structures", Northwestern University, December 1998.

[23] Vesenjak M., Müllerschön H., Hummel A., Ren Z., "Simulation of Fuel Sloshing – Comparative Study", 3rd local LS-DYNA Conference, Germany, October 2001.

[24] Day J., "Guidelines for ALE Modeling in LS-DYNA", Livermore Software Technology Corporation, 2009.

[25] Souli M., "Fluid-Solid Interaction in LS-DYNA", 4th European LS-DYNA Users Conference, May 2003.

[26] Souli M., Wang J., Do I., Hao C., "ALE and Fluid Structure Interaction in LS-DYNA", 8th International LS-DYNA Users Conference, May 2004.

[27] Olovsson L., Souli M., Do I., "LS-DYNA – ALE Capabilities (Arbitrary-Lagrangian-Eulerian) Fluid-Structure Interaction Modeling" Livermore Software Technology Corparation, January 2003.

[28] LS-DYNA Keyword User's Manual, Version 971, Rev 5, Livermore Software Technology Corporation, May 2010

[29] LS-DYNA Support, http://www.dynasupport.com/howtos/material/eulerian-method-basics, Last visited on August 2011.

[30] LS-DYNA Support, http://www.dynasupport.com/howtos/general/equation-of-state, Last visited on August 2011.

[31] Mahmadi K., Itoh S., Hamada T., Aquelet N., Souli M., "Numerical Studies of Wave Generation Using Spiral Detonating Cord", Material Science Forum, Vol. 465-466, pages;439-444, 2004.

[32] Aquelet N., Souli M., "2D to 3D ALE Mapping", 10th International LS-DYNA User's Conference, 2008.

[33] McCallum S. C. and Townsend D. D., "Simulation of Hydrodynamic Ram and Liquid Aeration", 5th European LS-DYNA Users Conference, 2005.

[34] Shah A. S., "Water Impact Investigations for Aircraft Ditching Analysis", Master of Science Thesis, School of Aerospace, RMIT University, January 2010.

[35] Johnson G. R., Holmquist T. J., "A Computational Constitutive Model for Brittle Materials Subjected to Large Strains, High Strain Rates, and High Pressures", Shock-wave and High-Strain-Rate Phenomena in Materials, New York, pages;1075-1081, 1992.

[36] Johnson G. R., Holmquist T. J., "An Improved Computational Constitutive Model for Brittle Materials", High-Pressure Science and Technology-American Institute of Physics, 1994.

[37] Krashanitsa R., "An Inverse Computational Approach for the Identification of the Parameters of the Constitutive Model for Damaged Ceramics Subjected to Impact Loading", Doctor of Philosophy Thesis, Department of Aerospace and Mechanical Engineering, University Of Arizona, 2005.

[38] Johnson G. R., Holmquist T. J., Beissel S. R., "Response of Aluminum Nitride (Including Phase Change) to Large Strains, High Strain Rates, and High Pressures", J. Appl. Physics 94, pages; 1639-1646, 2003.

[39] Gazonas G. A., "Implementation of the Johnson-Holmquist II (JH-2) Constitutive Model Into DYNA3D", Army Research Laboratory, ARL-TR-

2699, March 2002.

[40] Cronin D. S., Bui K., Kaufmann C., Mclntosh G., Berstad T., "Implementation and Validation of the Johnson-Holmquist Ceramic Material Model in LS-DYNA", 4th European LS-DYNA Users Conference, 2003.

[41] Holmquist T.J., Templeton D.W., Bishnoi K.D., "Constitutive Modeling of Aluminum Nitride for Large Strain, High-Strain Rate, and High-Pressure Applications", International Journal of Impact Engineering, 2001.

[42] Güden M., Taşdemir A. "Test Raporu – Germanyum Malzemesi JH-2 Modeli", Dinamik Test ve Modelleme Labaratuarı, İzmir Yüksek Teknoloji Enstitüsü, İzmir, October 2009.

[43] "Saab Rain Erosion Test Facility", Brochure, SAAB AEROSYTEMS, Box SE-581-88, Sweeden, Tel: +46(0)13 18 00 00, E-mail : flighttest@saab.se, www.saabgroup.com.

[44] Avşar A. L., Özhan A. E. S., "Yağmur Erezyonu Testi Sonuç Raporu", ASELSAN INC Internal Report, 2009.

[45] Boxel J. H. V., "Numerical Model for the Fall Speed of Raindrops in a Rainfall Simulator", Faculty of Environmental Sciences, University of Amsterdam, Netherlands, Workshop on Wind and Water Erosion, 1997.

[46] Goldman L. M, Tustison R. W., "High Durability Infrared Transparent Coatings", SPIE, Vol: 2286, pages; 316 - 324, 1994.

APPENDIX-A

EXAMPLE CALCULATION ON NUMBER OF WATER DROPLETS HITTING TO TARGET

Question:

How many impacts are expected for a 25.4 mm diameter window travelling 125 m/s through a 2.5 cm/h rain fall consisting of 2mm diameter raindrops released from 0.15m above the target in 5 minutes?

Solution:

The terminal velocity for 2 mm diameter raindrops released from 0.15m above the target is:

$v_t = 1.75\ \mathrm{m/s}$. (from Figure 4.11)

Equation 4.1 gives the number of impacts:

$$\text{impacts} = {10\ (2.5)(125)(\pi \times 1.25^2)(5 \times 60)} \Big/ {6\ \pi(2^3)(1.75)} = 17438$$